Design of a Radially Segmented Halbach Multipole Magnetic Bearing.

AE-5711: Thesis Aerospace Structures & Materials

Buta Vlad

Delft University of Technology

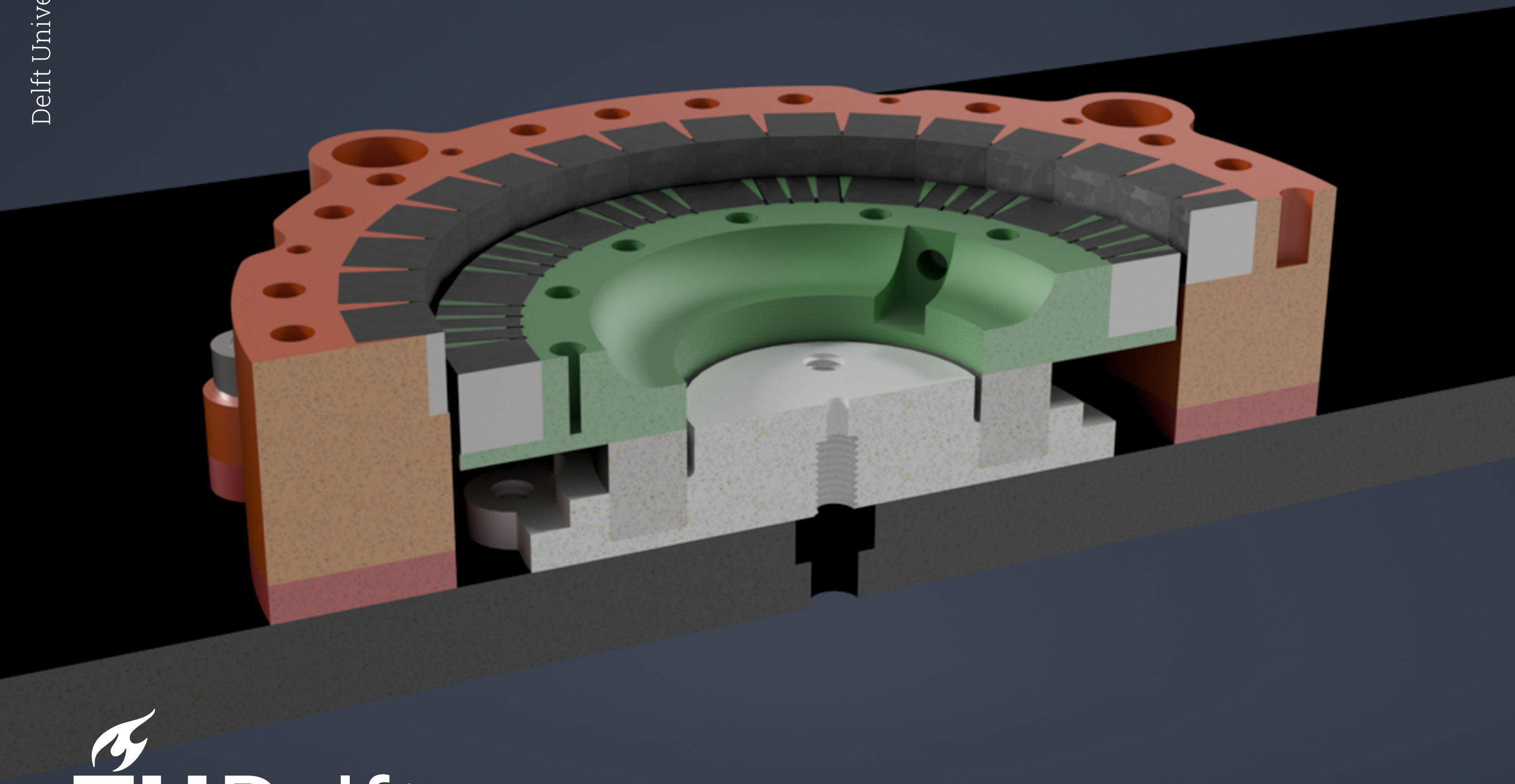

TU Delft

Design of a Radially Segmented Halbach Multipole Magnetic Bearing.

by

Buta Vlad

Student Name	Student Number
Buta Vlad	5627753

Primary Supervisor:	Ines Uriol Balbin
Project Duration:	March, 2023 - September, 2023
Faculty:	Faculty of Aerospace Engineering, TU Delft

Cover: Autodesk Inventor Pro - Bearing Prototype Render

TUDelft

Acknowledgements

The work conducted and resulting thesis marks the culmination of my academic journey at the TU Delft Faculty of Aerospace Engineering. This achievement would not have been possible without the invaluable aid and unwavering support of numerous people, for which I wish to take a moment and express my gratitude.

First and foremost, I wish to extend my deep appreciation to my thesis advisor, Ines Uriol Balbin, whose guidance, expertise and patience were instrumental in shaping the direction of my research. Your insightful feedback and constant encouragement are what motivated me throughout the entirety of the project's duration. I am truly grateful for the opportunity to work under your mentorship.

I am also indebted to all my colleagues and supervisors at ARCSEC, who offered me the chance of operating in an environment which fosters innovation, collaboration and curiosity. I wish to especially extend my appreciation to my external supervisor, Mante Bakeleand, who has provided me with a constant source of inspiration in the development of my thesis, as well as crucial guidance in the field of magnetic bearings. The insights gained and discussions I had with my colleagues significantly enriched my research and broadened my understanding of the engineering process in all its aspects. I also wish to extend my gratitude to Tjorven Delabie, Jelle Lanting and Alexander Vandenberghe, who have all aided me in the development of my work. Working alongside each of you has been a privilege for which I wish to thank you.

Last but not least, I am grateful for the never ending support of my parents and friends, without which I could simply not have made it this far. Your encouragements and unabated reassurance are what made my journey possible. Please know that your impact could not have gone unnoticed and is deeply appreciated.

This work stands as a testament to the collective efforts of all those involved in guiding my academic path. Although I unfortunately cannot name every single individual here, I wish to thank you for being an integral part of this transformative chapter in my life.

Thank you!

Buta Vlad
Delft, September 2023

Summary

In recent years, an increasing interest for high pointing accuracy systems can be observed within the space sector. As such, the micro-vibration environment and its reduction has become a more pressing matter for engineers. It is generally accepted that the reaction wheel system within a spacecraft's Attitude Control and Determination System (ADCS) has the greatest impact on on this environment, and as such has the opportunity of providing the most substantial gains in performance with the implementation of newer bearing technologies. Magnetic bearings generate a soft suspension mechanism which can greatly help with the mitigation of micro-vibrations, as well as offering a virtually infinite operational life. However, they can raise issues if magnetically sensitive equipment is in close proximity to the bearing, especially if the permanent magnets employed generate high stiffnesses, translating to strong magnetic fields. In order to better control the generated magnetic field, specific configurations and orientation patterns of magnets can be employed. In this manner, the exterior field of the bearing can be curated to a specific application.

This thesis explores the concept of Multipole Magnetic Bearings, focusing on Halbach pattern radially segmented configurations. In its most basic form, such a bearing is composed of two concentric circular magnets, both segmented into arc-shaped magnetic elements with alternating orientations. The bearing studied employs a Halbach pattern, with a 90 degree polarization axis shift between magnetic elements, forming a repeating unit of 4 elements. This radially segmented configuration, although complex in its design, has been chosen based on its reduced volume when compared to other multipole bearings architectures, thus allowing for more possibilities of integration. Within this configuration type, three main design parameters have been studied: the number of segments employed in a radially symmetric bearing, the ratio between the number of segments of each of the two arrays (radially asymmetric bearing), and the ratio between individual magnets within a magnetic array. Four different bearing magnetization directions have been considered (2 axial, 2 radial), as well as two additional concepts: the introduction of ferromagnetic elements within the arrays in an attempt to better control the generated magnetic field, and combining a multipole array with a monolithic magnet for the purpose of stabilizing bearing performance throughout its rotation.

The primary differentiating factor between these configurations was the generated bearing stiffness. Both the radial and axial stiffness are critical performance indicators, which have great impact on rotational stability and micro-vibration response. The ideal configuration should provide high radial stiffness, constant throughout rotation, and zero axial destabilizing force under a perfectly centered position. Such a configuration has been found through combining a conventional monolithic magnet and a multipole segmented magnet with a $1/3$ ratio between the "working" segments and the "pattern-completion" segments. A prototype of such a configuration has also been developed and built, in order to determine simulation results accuracy and attempt concept validation.

The experimental part of the thesis focuses on a simplified model of the optimal configuration, replacing the arc-shaped segments with cubic and rectangular magnets. This has been done in order to allow for readily available, off-the-shelf magnets to be employed. The supporting structure of test setup has been 3D printed in PLA, which allowed for the possibility of quick iterations within the testing process. However, the prototype did not achieve radial stability due to manufacturing tolerances, both in relation to the magnetic elements and the low stiffness of the 3D printed structure. The determination of the axial stiffness was possible, for which a scale was employed, while a gaussmeter was used to measure the strength of the generated magnetic field of individual magnets within the array.

Simulation results have been obtained through ANSYS Magnetostatic Workbench (student version), while the test setup has been developed and designed in Autodesk Inventor Pro.

Contents

List of Figures

List of Tables

Nomenclature

Abbreviations

Abbreviation	Definition
ADCS	Attitude Determination and Control System
RWA	Reaction Wheel Assembly
PMB	Passive Magnetic Bearing
AMB	Active Magnetic Bearing
EDB	Electrodynamic Bearing
RMD	Rotating Magnetization Direction
TMFD	Total Magnetic Flux Density
CAD	Computer Aided Design
FEM	Finite Element Method
PLA	Polylactic Acid
ACS	Axial Cross Section
RCS	Radial Cross Section
R	Radial Configuration
RF	Radial Focus Configuration
AH	Axial Halbach Configuration
AnH	Axial non-Halbach Configuration
ID	Inner Diameter
OD	Outer Diameter
RPM	Revolutions per minute

Symbols

Symbol	Definition	Unit
K_r	Radial Stiffness	[N/mm]
K_a	Axial Stiffness	[N/mm]
F_a	Axial Force	[N]
B	Magnetic Flux Density	[T]
B_r	Residual Magnetism	[T]
BH_{max}	Maximum Energy Product	[MGOe]

1

Introduction

This section of the thesis aims to explain the fundamental principles behind the concept of magnetic bearings and the literature surrounding them, as well as defining necessary terms used in their development and testing. The reasoning behind their usage in the modern aerospace industry is first addressed, followed by a brief classification of the various magnetic bearing types. The section closes with a description of key performance parameters and their relevance within the bearing system.

1.1. Magnetic Bearing Fundamental Concepts

One of the most crucial systems a spacecraft is the Attitude Determination and Control System (ADCS), which is in charge of maintaining pointing accuracy and stability. Over time, the technology powering this system has been improving, thus making very high pointing accuracies more reachable than before. However, with better technology also came more stringent requirements for missions with high stability sensitivity payloads, such as Earth observation or laser communication missions. For these types of spacecraft, one of the most common problems encountered are the disturbances caused by micro-vibrations, which can raise considerable issues for the operational success of the mission if not properly managed. Much effort has already been put into their mitigation and reduction through the use of various dampening systems and careful design of the structural components. However, as long as there is a solid transmission media between sensitive equipment and disturbance generating components, the micro-vibration environment will pose a risk to the mission. Within the systems of a spacecraft, the one that is generally considered to be the main source of this type of disturbance is the Reaction Wheel Assembly (RWA), a central component of the ADCS. The RWA typically consists of an electric motor driven flywheel-shaft component, which is conventionally supported by ball bearings. The most common reasons for the generation of disturbances within the RWA are rotor imbalance, motor eccentricity, material degradation and bearing irregularities [1].

The operating principle of the assembly being the conservation of angular momentum. Through spinning the flywheel in a certain direction, the generated momentum will be transferred to the spacecraft body, leading to a counter rotation motion. Multiple such flywheel assemblies are present on a spacecraft in order to allow for controlled orientation in all axes. Given their role, and with breakdowns possibly leading to mission failure, they are a critical component of the ADCS. The RWA supporting bearings are subjected to a harsh operational environment, comprised of very high RPM values sustained for long periods of time [2]. This can lead to heavy wear of the working surfaces in the case of conventional bearings, limiting the operational life of the RWA, and thus the entire spacecraft. Ball bearings can also suffer from more complex issues, such as bearing race degradation caused by electrical discharge [3] [4], which introduces new disturbance sources to the system. These issues have been documented as the root cause of mission failures in the past, such as on NASA's Far Ultraviolet Spectroscopic Explorer (FUSE) [5] and on the Kepler space telescope [6]. One last disadvantage of ball bearings is their inherent high radial stiffness, which forms an ideal media for micro-vibration transmission between the RWA and the spacecraft body.

Magnetic bearings offer solutions to these problems through the creation of a soft suspension media between the RWA and the spacecraft structure. In this manner, no bearing surfaces are in mechanical contact, eliminating wear and allowing for a virtually infinite operational life [7]. The soft suspension mechanism also dampens vibrations being generated by the RWA, the main variable responsible for this mitigation being the generated radial stiffness [7]. However, these advantages also come with an increase in development cost and manufacturing complexity, which can be a deterrence to their implementation when compared to the tried-and-true ball bearings. Furthermore, through their operating principle of opposing magnetic fields, magnetic bearing can raise issues if magnetically sensitive components are in close proximity to the bearing. With space coming at a premium on most modern satellite platforms, limiting the usable space around the bearing can be a considerable issue. As such, if the external magnetic field of the bearing could be adapted to each application, they would be a more attractive bearing solution to satellite developers. This is where multipole magnetic bearings have the advantage over their monolithic counterparts - their external magnetic field can be controlled through varying the the orientation of individual magnets within the array.

1.2. Magnetic Bearing Types

Passive Magnetic Bearings

Passive magnetic bearings (PMBs) are bearings in which the bearing function carried through the attractive and repulsive forces generated between magnet pairs. The most common type of magnet employed for the development of bearings are sintered rare-earth Neodymium magnets, which offer the most performance out of all permanent magnetic materials. Their magnetization most commonly falls within either axial, radial or diametrical orientation. Arrangements of these magnetizations into set patterns are the basis for multipole bearings, which will be presented with more detail in the next chapter. The primary performance metrics used to assess these bearings are the bearing load, the radial and axial stiffness generated, the destabilizing force and the damping properties of the bearing. These variables can be adapted to a particular application through magnet volume, magnet grade, layering of magnets and magnetization patterns.

The primary advantage of PMBs is their passive nature, requiring no external resources for the stabilization of the bearing load in its primary direction (radial direction for radial bearings, axial direction for axial bearings). Other advantages are long operational life, as a result of not requiring mechanical contact (and thus no friction), low vibration transmission in low stiffness configurations, very high reliability and high load bearing capacity to weight ratio. By comparison to traditional ball bearings, magnetic assemblies typically have a lower stiffness and load bearing capacity for the same bearing volume. The primary disadvantage of PMBs is their inability to achieve stable levitation of the rotor assembly in all degrees of freedom through their own passive means. As stated in Earnshaw's theorem [8], if a passive magnetic system is stable in the radial direction (a positive radial stiffness is generated between the stator and the rotor), then the axial direction will be unstable (a negative axial stiffness is generated, leading to a destabilizing axial force between the stator and the rotor). Similarly, axial stability will lead to radial instability. As such, in order for a PMB to be operational, stability of the weak direction will need to be provided by an annex mechanism through counteracting the destabilizing stiffness. This can be achieved in a variety of ways, either through using another type of magnetic bearing (active magnetic bearing, electrodynamic bearing), conventional ball bearings or other mechanical elements. Each solution brings its own advantages and disadvantages by means of cost, complexity, reliability and operational limitations.

Active Magnetic Bearings

Active magnetic bearing (AMBs), by comparison to their passive counterparts, offer the advantages of higher achievable stiffness and a higher load bearing capacity. Additionally, their damping behavior can improved through active vibration isolation. However, the reliability and resource independence of the PMBs is no longer present. In order to operate, AMBs require a finely tuned control loop, which increases the cost and complexity of their development. Based on rotor displacement readings, a current is fed to coils within the bearing, generating a working magnetic field. This field then interacts with a ferromagnetic material element on the rotor to stabilize it. This type of bearing is not the main focus of this work, and as such will not be treated in great detail.

However, it is worth mentioning that active magnetic bearings can be part of hybrid magnetic assemblies which have an increased efficiency over mono-architecture bearings. Such a system is presented in the works of Lijesh and Hirani [9], where a multipole PMB is paired with an AMB to reduce its running cost by 31%. Another example of a similar hybrid bearing is presented in the works of Choi et al. [10] [11], where Halbach multipole arrays are used to increase the static force of a bearing system by a factor of four, while also introducing a gravity load compensation system to the assembly.

Electrodynamic Bearings

Electrodynamic bearings are mechanisms which employ Lorentz forces in their operation. The working principle behind this type of bearing are the eddy currents formed as a result of relative motion between a ferromagnetic element and a magnetic field. In most cases, EDBs are based on a rotating object in a stationary magnetic field. However, this imposes operational limitations on the bearing, as without relative motion there is no levitating or stabilizing force being generated [12]. Therefore, employing this type of bearing in a RWA would be detrimental to mission success, due to zero crossings of the flywheel resulting in a total loss of bearing support.

1.3. Magnetic Bearing Performance Definition

When talking about the performance of a magnetic bearing, regardless of the operational type or monolithic/multipole configuration, a set of relevant variables must be identified and defined. This section of the thesis addresses parameters which are of interest to the research being conducted and discusses their importance in the development process.

1. **Magnet Grade ($N - X - Y$):** The grade of a magnet provides valuable information about the permanent magnetic material used. In the case of Neodymium magnets, N represents material type (Neodymium - NdFeB), X represents the maximum energy product BH_{max}, or the ”strength” of the magnet, and Y represents the temperature resistance, or the safe temperature range in which the magnet does not lose its magnetism.

2. **Residual Magnetism (B_r) :** Residual magnetism, or Remanence, is the strength of the magnetization of a material after the forming magnetizing field is removed. This parameter shows the practical strength of the magnetic material and is used in simulations as a material definition variable.

3. **Magnetic Flux Density (B) :** Magnetic flux density is a measure of the magnetic flux through a given area, and is a parameter which indicates ”where the magnetic field is the strongest”. This variable is crucial in the assessment of both internal and external magnetic fields generated by the bearing. Measurements can be conducted through a Gaussmeter.

4. **Radial Stiffness (K_r) :** In the case of radial bearings, the generated radial stiffness is the driving parameter in bearing performance when it comes to radial stability and micro-vibration dampening behavior. This value can be measured through imposing a radial displacement to the bearing’s rotor and measuring the centering force generated.

5. **Axial Stiffness (K_a) :** In the case of radial bearings, the axial stiffness is negative and thus destabilizing within the bearing system, which introduces the requirement for a compensation mechanism in order for the bearing to function. The axial stiffness is related to its radial counterpart through the following approximation: $K_a = -2 \cdot K_r$. [13]

6. **Axial Force (F_a) :** In the case of radial bearings, the axial force being generated is a byproduct of the negative axial stiffness, and is a destabilizing force. It can be measured through imposing an axial displacement to the bearing’s rotor and measuring the destabilizing force generated.

7. **Cartesian Forces in the radial plane (F_x, F_y) :** In the case of radial bearings, the forces are stabilizing and, in an ideal system, should be null and constant throughout the bearing’s rotation.

2

Research Framework

This chapter of the thesis starts with a brief overview of the state of the art in the field of multipole magnetic bearings, classifying the different designs based on bearing architecture and selecting one of them as the main focus of this work, followed by a section on theoretical approximations and mathematical models. The second part of this chapter focuses on the Research Questions formulated based on the Literature Study, together with the definition of the Requirements, Objectives and Methodology that the study will adhere to.

2.1. Literature Study

This initial section of the literature study review will briefly go over the main configurations found in literature, and discuss the trade-off process which lead to the choice of the radially segmented Halbach configuration. Following this, each configuration will be discussed individually, with examples of their implementations in literature. The four main bearing architectures are presented in the figure below.

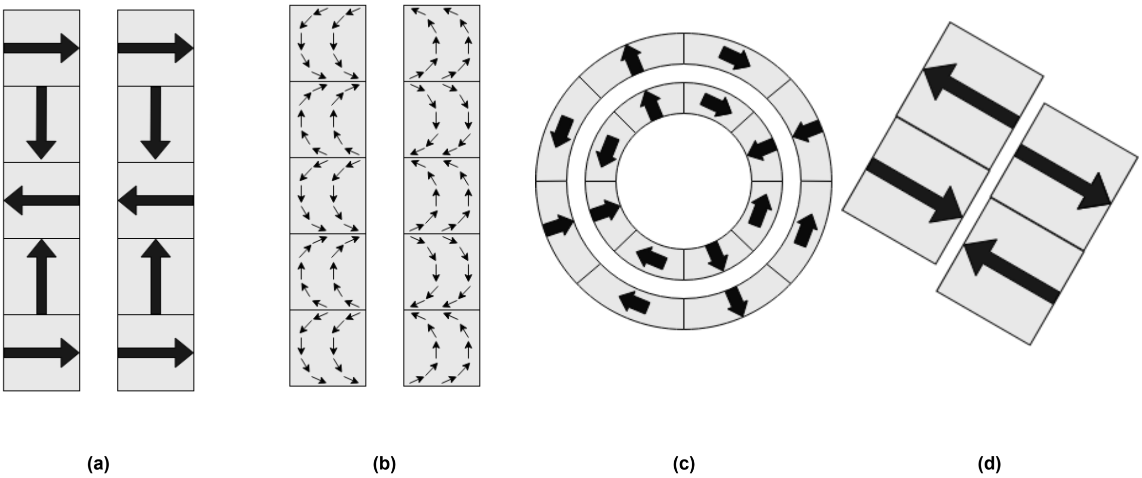

(a) (b) (c) (d)

Figure 2.1: Multipole Magnetic Bearing Configurations Overview. (a) Stacked ring magnet arrays with varying degrees of magnetization rotation angle. (b) Stacked ring magnets with continuously rotating magnetization. (c) Segmented ring magnets with Halbach configurations. (d) Stacked ring conical magnets with 180 degree magnetization rotation angle.

Design geometry and complexity considerations

The configurations vary in complexity from the stacked ring magnets configurations (2.1a), which employ simple axially or radially magnetized ring-magnets to operate, to the continuously rotating magnetization configuration (2.1b) that requires highly specialized equipment in order to be manufactured. Both the segmented (2.1c) and conical (2.1d) architectures fall between the first two in design complexity. However, this is not the only factor in choosing a configuration architecture. The dimensions of the bearing are an important consideration. Within the RWA, a driving design concept is the reduction in axial length (direction of the axis of rotation) of the system with the scope of improving rotational stability. As a result, a bearing with a reduced emphasis on axial length would be favorable. The stacked and continuously rotating magnetization architectures have as primary dimension the axial length, and as such have a disadvantage based on this criterion. Conical bearings have a relatively low axial length, but their manufacturing and assembly processes can raise issues during development, which will be discussed further in the next paragraph. Segmented bearing designs have the smallest axial length, being on par with conventional monolithic bearings, and as such are the best fit from a geometry standpoint. Both segmented and conical architectures also allow for simplifications of their respective designs, which greatly help with their translation into a prototype.

Commercial availability considerations

When considering the commercial availability of the magnetic elements, stacked ring magnets with 180 degree magnetization angle (top-to-bottom and alternating magnetization) are the simplest way of implementing a multipole magnetic bearing, as axially magnetized ring magnets are readily available. The same can be said for stacked ring magnets with 90 degree magnetization angle (Halbach configurations), which combine axial and radial magnetizations. The manufacturing process is starting to become considerably more complex with the introduction of expanded Halbach configurations, where the magnetization angle between adjacent magnetic elements falls below 90 degrees (such as magnet stacks with 45 degree magnetization angles). The stack segments which require a diagonal magnetization pattern are exponentially more difficult to find as off-the-shelf components, and would most likely require a custom order.

Arc shaped magnets are available commercially, although to a smaller degree than cubic ones. However, their magnetization can raise issues for segments that require a tangential orientation, thus implying a custom order. Conical ring magnets are virtually non-existent as off-the-shelf components, and would require a highly specialized production facility in order to account for the conical aspect of the elements, thus reducing the feasibly of the concept. Continuously rotating magnetization patterns would require in-house development of a magnetization coil in order to be manufactured, which falls outside the scope of the project as it greatly increases its complexity. As a result of these considerations, the most feasible concepts are the stacked and segmented ring magnets.

Trade-off Conclusion

When taking into account both geometrical and commercial availability trade-off processes presented above, the two architectures which would best fit the profile for a RWA bearing are the segmented ring and the conical configurations. Both of them have a small axial profile and allow for magnetic design simplification, which compensates for the relatively limited commercial availability. However, the segmented architecture presents a lower estimated complexity of assembly, which ism beneficial when an experimental phase to the project is to be carried out with relatively limited equipment. As such, the final bearing architecture will follow a segmented ring magnet with Halbach patterns configuration (Fig. 2.1c).

2.1.1. Stacked Magnetic Configurations

The concept of multipole magnetic bearings was initially explored by Yonnet et al. [13], where both the stacking of circular magnets with top-to-bottom and rotating magnetizations were considered. A similar setup had also previously been developed by Klaus Halbach in the 1980s [14], with the scope of focusing particle accelerator beams. The paper by Yonnet et al. is aimed at enhancing the centering stiffness of multipole bearings, while minimizing relative bearing volume. The starting point for the investigation was a conventional passive magnetic radial bearing, which composed of two concentric ring magnets generating repulsive forces. Through the top-to-bottom stacking configuration, depicted in Figure 2.2a (four stacked magnets with 180 degree magnetization direction between adjacent magnets), the authors improved the radial stiffness performance by a factor of seven, while magnet volume increased by a factor of four. While this result showed considerable improvements to bearing stiffness performance, it could further be enhanced by decreasing the magnetization rotation angle to 90 degrees. This configuration, referred to in the paper as magnet stack with rotating magnetization direction (RMD), can be observed in Figure 2.2b. The RMD setup resulted in a radial stiffness twelve times greater than that of the baseline configuration, while only increasing the volume by a factor of four.

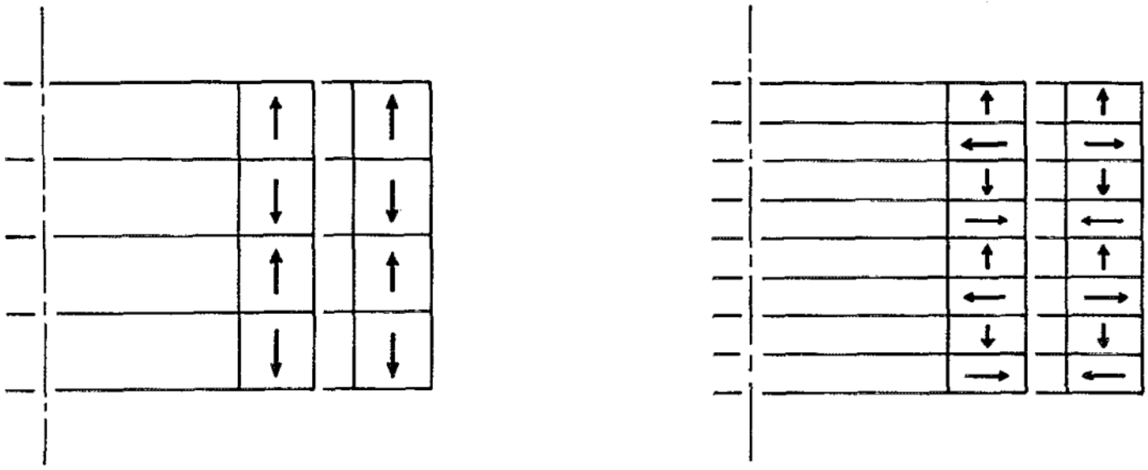

(a) Top-to-Bottom Magnetic Stacking.

(b) Rotating Magnetization Direction Stacking.

Figure 2.2: Top-to-Bottom and Rotating Magnetization Direction Stacking, Yonnet et al. [13]

Using a similar concept, Robertson et al. [15] employed a neodymium Halbach array as a load bearing spring for a vibration isolation table. The system can be observed in Figure 2.3. Each array was composed of four alternating polarization magnets, with a magnetization wavelength of 30mm. In their study, the authors investigated the forces between opposing arrays while varying the ratio of magnetization wavelength to array thickness. The configuration which led to the greatest generated force is characterized by a ratio of 2 (wavelength of magnetization is twice the thickness of the multipole array). This ratio equates to a square cross section of the individual elements, which is also confirmed to be an optimal solution in [16]. The authors also noted that reducing the magnetization rotation angle to 90 or even 45 degrees would result in stronger generated forces. Consequently, this adjustment would enable greater achievable stiffness for the same bearing volume.

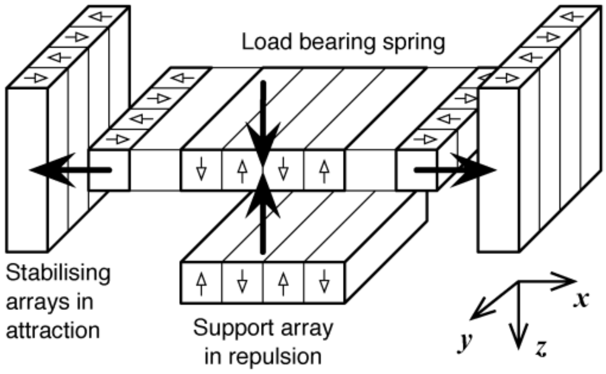

Figure 2.3: Multipole array magnetic spring designed by Robertson et al. [15]

Planar Halbach arrays find another application in the study conducted by Lijesh and Hirani [9], in which the primary objective is the reduction of the operational costs in the case of an active magnetic bearing. The paper explores two configurations: a ”full” Halbach array, containing five magnets with a 90-degree magnetization rotation angle, and a simplified ”half” Halbach array with only three such magnets. The maximum flux density obtained through simulation of the full arrangement was 1.8 times higher than a conventional active magnetic bearing, and only 1.14 times higher than the half arrangement results. Therefore, the authors determined that the complexity involved in developing the full Halbach array was unwarranted for the relatively small flux density improvement.

The concept of stacked ring magnets is also presented by Feipeng et al. [17], where a parametrization and optimization process is developed. The paper first describes an ideal three-pair-pole Halbach radially magnetized ring, characterized by a unidirectional magnetic flux, commonly known as ”self-shielding”, which has the property of a completely single sided magnetic flux, and can be observed in Figure 2.6b. This ideal sinusoidal magnetization pattern however, is very difficult to manufacture. In order to simplify the design, the sinusoidal pattern is segmented, with better approximations achieved through higher segment counts per pole. The authors opt for two segments per pole, resulting in a 90-degree rotation angle, which brings the advantage of requiring the stacking of either axially or radially magnetized rings. The approximation can be observed in figure 2.4b. Configurations with three to six stacks have been simulated in FEM software, resulting in a linear increase of the generated force, while the stability range remains constant.

A more in depth analysis of the optimization process for the ring magnet stacking method is presented by Moser et al. [18]. This optimization centers around maximizing the radial stiffness generated by the bearing, and is derived from testing a broad range of magnet layups, from monolithic to sixteen-layer configurations. The authors concluded that the optimal configuration is independent of the bearing’s aspect ratio, but highly dependent on the air gap employed.

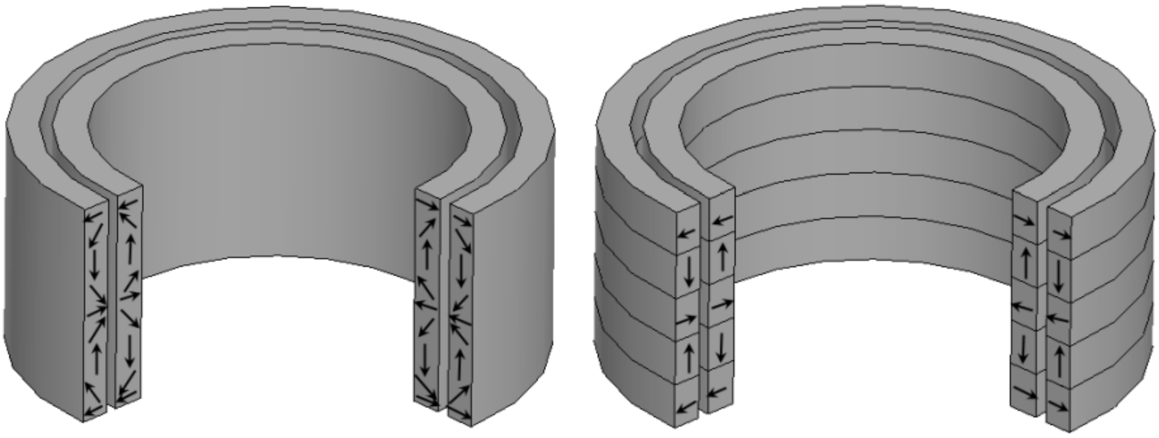

(a) Sinusoidal Magnetization **(b)** Segmented Magnetization Approximation

Figure 2.4: Ideal Halbach magnetization and its segmented approximation. [17]

A similar magnetic configuration is employed by Jinji et al. [19], where four stacked magnets with 90-degree magnetization rotation are employed to control the axial orientation of a magnetically suspended control moment gyro, with focus on the determination of the axial bearing angular stiffness. 2D FEM static magnetic analysis results lead to a difference between theoretical and experimental values of the angular stiffness of 11%, and 5% for the generated axial force.

Mystkowski et al. [20] explored the concept of stacked circular Halbach arrays is also explored, employing FEM analysis and experimental tests on a radial bearing constructed from a 180-degree magnetization rotation array. Its configuration is similar to the Top-to-Bottom stacking method presented in Figure 2.2a. The experimental setup showed very close results of the axial force, thus validating the simulation model.

In the work of Nielsen et al. [21], four different multipole magnetic bearing configurations are studied, employing radially and axially magnetized rings. The central focus of the paper is the quantification of forces generated by the bearings across various configurations. One particularity of the paper is the usage of a circular array of many cubic magnets as a simplification of the design in order to ease the manufacturing process.

In the paper by Wu et al. [22], a series of Halbach magnet arrays were integrated as the upper bush of the water-lubricated bearing aiming to mitigate friction-induced vibrations. Simulation is employed to gauge the stiffness and damping coefficients of the bearing, which are then compared to those of a conventional rubber bearing. The Halbach system proved to have a lower stiffness but a superior dynamic stability.

2.1.2. Segmented Magnetic Configurations

Liu et al. [23] discusses a distinct approach to the multipole concept. Instead of stacking magnets to construct planar or circular arrays, a circular array is developed through arranging alternating polarization segments. The focus of the paper is on increasing magnetic torque coupling through circular Halbach arrays, as opposed to the linear ones employed in previously presented papers. The paper discussed multiple co-axial and face-to-face configurations of alternating magnetic poles. In the case of co-axial configurations, the coupling torque was found to increase as the number of poles increases, peaking at twelve poles. For the face-to-face configurations, two options were discussed: a conventional eight pole circular array with a 180 degree alternating magnetization, and an eight pole, 16 segment Halbach array (with 90 degree alternating magnetization). The magnetic flux density of the Halbach array design increased by 48.7% when compared to its eight poles, eight segments counterpart. The optimum number of poles, however, is specified to be heavily dependent on system geometry and considered air-gap.

In the study by Eichenberg et al. [24], the circular Halbach array concept is further explored and tested upon, through two multipole magnet designs. The first one was composed of 16 magnet segments, while the second of 32 magnet segments. Both systems were tested in relatively large air-gap configurations (above 1mm). The design can be observed in Figure 2.5. The magnetic arrays were employed in both tests on the rotor of the testing rigs, while the stators featured a coiled system which was the main focus of the study. As such, no mentions were made on bearing stiffness or Halbach Array design characteristics.

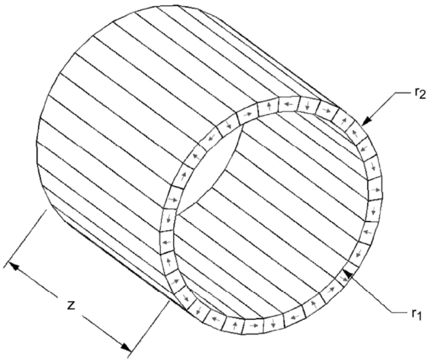

Figure 2.5: 32 Segment Circular Halbach Array. [24]

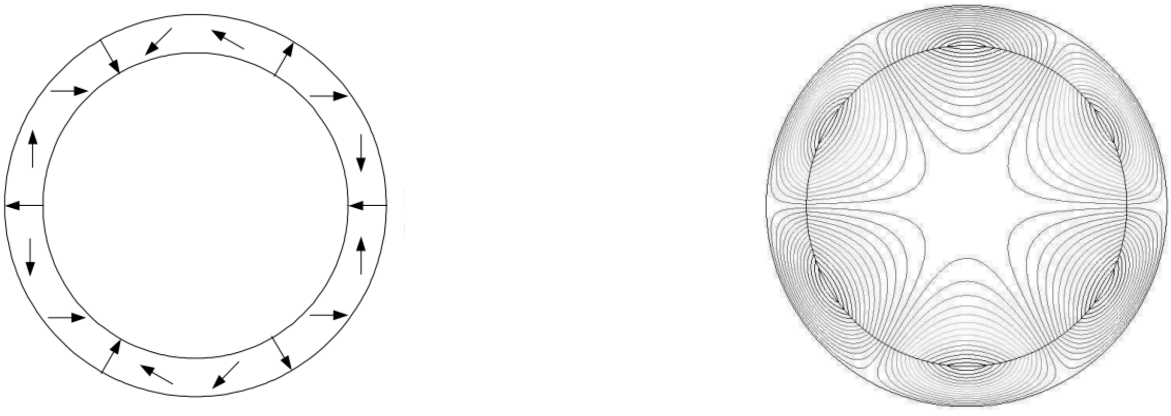

(a) Magnetization Direction

(b) Generated Magnetic Flux

Figure 2.6: Ideal Halbach Magnetization (3poles), displaying of its the self-shielding property [17]

2.1.3. Special Magnetic Configurations

Marth et al. [25] introduces the concept of continuous rotating magnetization as a method of increasing bearing stiffness. The paper outlines two methods of achieving rotating magnetizations: through stacking of uniformly magnetized permanent magnets with different magnetization directions (similar to prior sections of the paper) or through the magnetization of a single magnetic element for continuous rotation. This latter magnetization pattern was also mentioned in Feipeng et al. [17] and can be seen in Figure 2.7. Employing a two pole rotating magnetization instead of uniform magnetization, an increase in stiffness by a factor of 3.7 was achieved, however this value was limited by pre-imposed geometrical constraints.

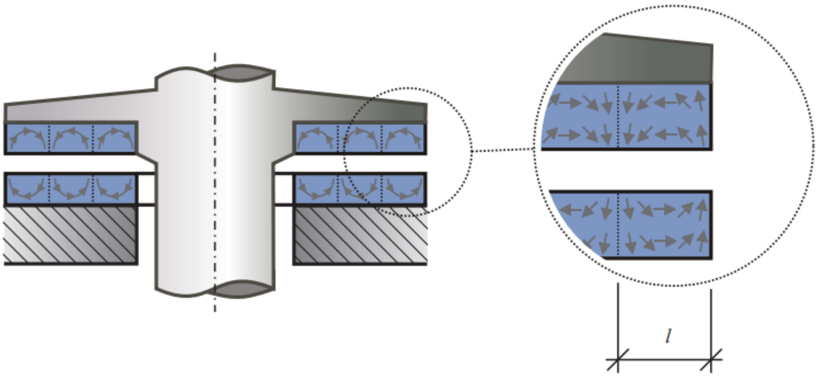

Figure 2.7: Continuously Rotating Magnetization Pattern with three magnetic poles and pole length l. [25]

This pattern is however very difficult to manufacture, closely resembling the ideal Halbach magnetization featured in Figure 2.6a. In order to obtain such a magnetization, a set of magnetization coils has been employed, which can be observed in Figure 2.8. The paper states that ensuring complete theoretical magnetization requires the coil-generated field to be three times the polarization's coercivity. However, this can lead to exceptionally high currents, resulting in elevated coil temperatures. As such, the thermal environment of magnetization coils can be a limiting factor in the manufacturing of bearings with continuous rotating magnetization. Another aspect discussed is that it may not be feasible to magnetize the entire cross-section of the magnetic element with the rotating magnetization pattern, thus leaving the outer regions of the cross-section with a pattern similar to the initial magnetization.

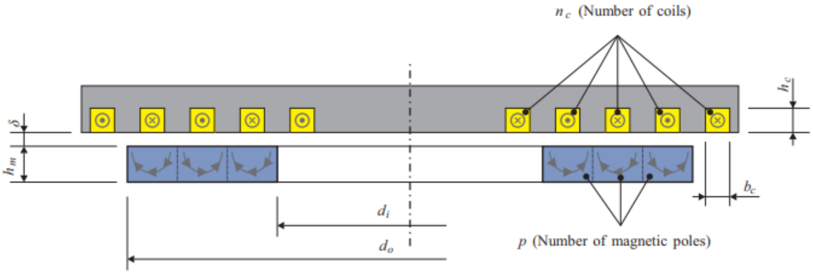

Figure 2.8: Parametric model of the Continuously Rotating Magnetization Coil. [25]

In all passive bearings, radial stiffness determines the required compensation active force to reach axial stability. However, the ideal balance between the negative and positive stiffness values is hard to reach, and even harder to maintain, as the radial stiffness itself varies with axial displacement. By angling the interfacing plane between the magnet rings into a conical shape, the bearing can exert forces along both the axial and radial directions, while also allowing for the adaptation of stiffness based on inclination angle. In the research conducted by Bjork et al. [26], such a bearing is developed and optimized. The bearing assembly is comprised of two concentric conical magnets. A range of configurations and inclination angles (from 0 to 90 degrees) are explored, all with a constant 0.2mm air-gap. These configurations can be observed in Figure 2.9. From the simulations conducted in the paper, the following relations have been found: increasing tilt angle results in reduced optimal bearing radius, volume-normalized force, and absolute stiffness. It has also been found that alternating the magnetization of the rings and the stacking of conical rings produce an increase in volume normalized force, regardless of inclination angle. It was also found that scaling the bearing improves generated force but leaves stiffness unaffected. Considering these findings, the optimal bearing characteristics are achieved at a 60-degree tilt angle, as it has a constant stiffness over a small axial displacement domain and a linearly varying force, properties which are desirable for an easily controllable bearing.

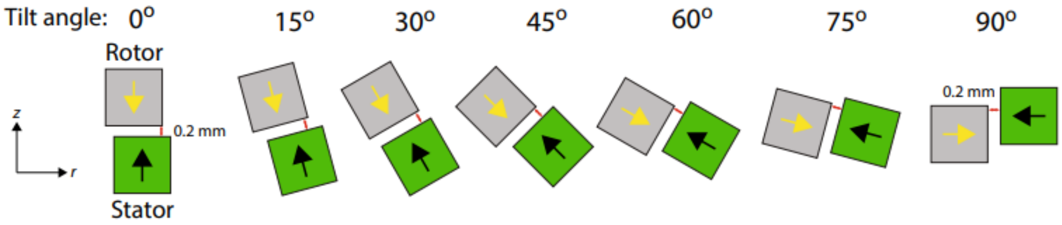

Figure 2.9: Conical Bearing Tilt Angle Configurations [26]

2.1.4. Approximations, Analytical and Semi-Analytical Mathematical Models

Yonnet et al. [13] offers a basic approximation of the radial stiffness of multipole stacked ring magnets as a function of individual layer radial stiffness was found and is presented in Equation 2.1. Stiffness values presented errors of less than 5%. However, for the improved rotating magnetization direction configuration (90 degree magnetization direction angle), an analytical solution is not discussed.

$$K_{rn} = (2 \cdot n - 1) \cdot K_r \tag{2.1}$$

In the paper by Robertson et al. [15] Bancel's "magnetic nodes" technique [27] was employed in order to solve the force-displacement relationship for a linear Halbach array. This analytical approach uses "nodes" located at the corners of cubical magnets to extract the field generated by linear magnet arrays. While the modeling of circular magnets is mentioned, it remains unelaborated. The analytical model is validated using finite element analysis software, resulting in a very small error (maximum error of 1%).

The determination of bearing stiffness, regardless of magnet type or magnetization direction, is dictated by the generated magnetic field. As such, the determination of the generated field is an integral part of the approximation process. The two most used models in determining this field in the case of permanent magnets are the equivalent charge model and the equivalent current model [28].

Ravaud et al. [29] develops a three-dimensional analytical approach, based on the Coulombian model, for studying cylindrical Halbach structures. The paper mainly focuses on structures composed of ring segment permanent magnets with radial or tangential magnetization. However, in a subsequent paper [30], the topic of varying magnetization direction of ring segment permanent magnets was discussed and an analytical model was developed. As such, the magnetic field generated by segmented ring magnets can be determined through analytical expressions, regardless of the magnetization orientation. In order to illustrate the model, 16 segments magnetic arrays with rotating polarization are studied, and the generated magnetic field is determined. In [29], two kinds of permanent magnet Halbach assemblies are developed: The first one resulting in a radial field whose shape is perfectly sinusoidal (Figures 2.10a and 2.11a), whereas the second type generates a radial field whose shape is trapezoidal (Figures 2.10b and 2.11b).

In the work of Selvaggi et al. [31] [32] equations for designing and optimizing cylindrical multipole magnets via toroidal harmonic expansion are developed. The initial paper focuses on axially magnetized cylindrical multipole magnets, specifically on four-pole cylinder magnets, while the second paper explores radially magnetized multipole rings.

In the study conducted by Hu et al. [33] an enhanced equivalent magnetic charge method for computing the magnetic field and forces generated by magnetic bearings with irregular magnetization or geometry is developed. This method is applied to determine magnetic properties of arc-shaped permanent magnets with irregular magnetizations, as well as on an annular Halbach array. The values obtained were then validated by both experimental testing and FEM simulations. It was concluded that the semi-analytical model overestimates force values, leading to a 5-10% error.

Marth et al [25] develops a method based on magnetic line dipole interaction energy [34] to compute analytical stiffness for systems with consciously rotating magnetization. The method's discussed downside is its reliance on a planar model, which does not account for ring magnet curvature. However, the model employed in the paper resulted in errors below 0.5%.

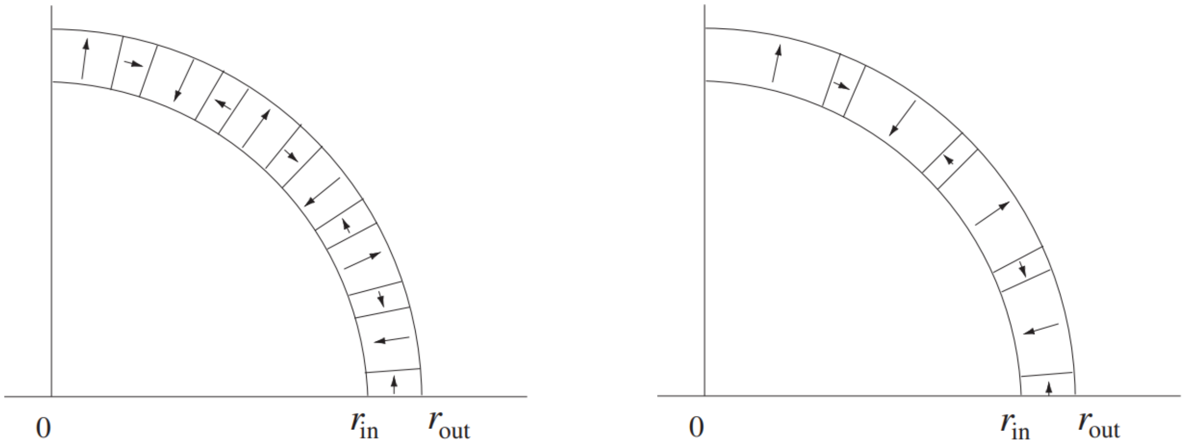

(a) Optimized Halbach Segmented Configuration with trapezoidal field and $\frac{1}{3}$ segment ratio.

(b) Optimized Halbach Segmented Configuration with trapezoidal field and $\frac{1}{5}$ segment ratio.

Figure 2.10: Analytically Optimized Halbach Segmented Configurations with varying segment ratios [29].

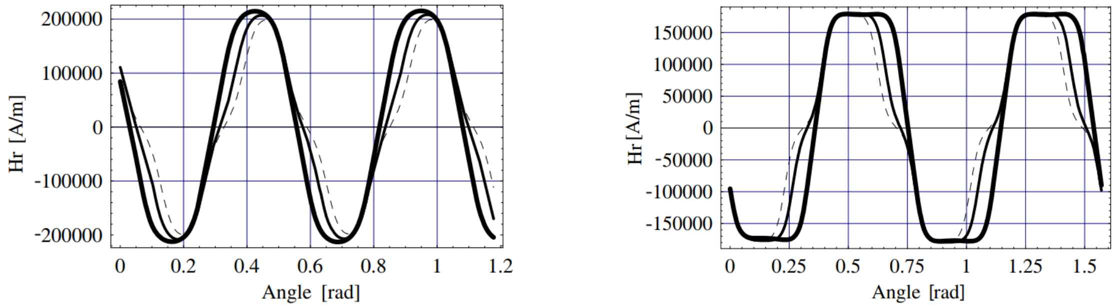

(a) Sinusoidal radial magnetic field. The thick line represents the angular width ratio between the tile permanent magnets radially and tangentially magnetized is $\frac{1}{3}$. The thin line represents a ratio of $\frac{3}{2}$, while the dotted line represents a ratio of 1.

(b) Trapezoidal radial magnetic field. The thick line represents the angular width ratio between the tile permanent magnets radially and tangentially magnetized is $\frac{1}{5}$. The thin line represents a ratio of $\frac{1}{2}$, while the dotted line represents a ratio of $\frac{5}{6}$.

Figure 2.11: Sinusoidal and Trapezoidal radial magnetic field shapes [29].

2.2. Research Questions

The following Research Questions have been formulated based on the radially segmented Halbach multipole magnet configuration which was chosen

1. **RQ-1:** How does the number of segments in a Halbach multipole magnet affect bearing performance in terms of generated magnetic field and bearing stiffness?
2. **RQ-2:** How does the ratio between the number of segments within a multipole magnet affect bearing performance in terms of generated magnetic field and bearing stiffness?
3. **RQ-3:** In comparison to a conventional monolithic magnetic bearing, how does a Halbach multipole magnet affect performance in terms of bearing stiffness?
4. **RQ-4:** To what extent do manufacturing and assembly tolerances affect the operation and radial stability of a multipole magnetic bearing?

The above presented Research Questions address the main aspects of multipole magnetic bearings which have either not received conclusive academic research or have not been investigated, to the best of my knowledge, in literature. As such, they tackle topics of interest for the field of magnetic bearings and their development.

2.3. Requirements, Research Objectives and Methodology

Requirements

This section of the thesis addresses the required parameters and expected achievable results for a radially segmented multipole Halbach magnetic bearing. The satisfaction of all requirements listed below is crucial to the development of a functional radial bearing, and as such must be respected in each step of the research process.

1. **REQ-1:** The designed bearing configuration must be radially stable.
2. **REQ-2:** The designed bearing configuration must maintain its radial stability throughout its rotation, with as little variance in stiffness as possible.
3. **REQ-3:** The designed bearing configuration must not generate any axial force in a perfectly centered position.
4. **REQ-4:** The designed bearing must either be feasible from a manufacturing standpoint in order to be translated into a prototype, or allow for a simplification of the design in such manner that a prototype of the configuration can be built.

The rationale behind the requirements listed will now be discussed. In order for a radial bearing to fulfill its core purpose, REQ-1 must be satisfied, translating to a positive generated radial stiffness without which no loads can be supported in the radial plane. Likewise, if the radial stiffness is not positive in all positions throughout the rotation of the bearing, stability will be lost and REQ-2 will not be satisfied. Variations in stability can lead to an unreliable bearing whose performance is dependent on the rotation angle, which is not desired in the case of RWA bearings. REQ-3 relates to the destabilizing axial force generated by radial bearings. Depending on the configuration, this destabilizing force can either be present or not in a perfect axially centered position. The generation of this force in this position is not desirable as it increases the load which must be compensated by an auxiliary stabilizing mechanism. For example, if using an active magnetic bearing for axial stabilization, in the case of a ”zero axial force” configuration, the small axial displacements based on which its control loop operates will only allow for the generation of relatively small destabilizing forces (ranging from a couple Newtons to tens of Newtons, depending on bearing strength), as these forces increase with displacement (in the near field). However, in the case of a ”non-zero axial force” configuration, the destabilizing force can be orders of magnitude higher than their counterpart configuration, requiring a more robust compensation mechanism, which in turn increases resource consumption and total bearing volume, both of which are undesirable effects. The last two requirements address the experimental part of the thesis. The satisfaction of REQ-4 assures that the chosen design will allow for the creation of a prototype. The requirement is met if most components can be procured off-the-shelf or do not require highly specialized equipment (e.g. manufacturing and magnetizing magnetic material is considered an unfeasible process).

Research objectives

1. **RO-1:** Identify a magnetic configuration which satisfies all imposed requirements for a radial magnetic bearing.
2. **RO-2:** Assess the performance of the designed configuration and compare it to a conventional monolithic magnetic bearing.
3. **RO-3:** Translate the identified bearing configuration into a prototype.
4. **RO-4:** Verify simulation results and assess prototype performance based on magnetic field and stiffness measurements.

The above listed research objectives outline the main milestones that need to be reached in order for the Research Objectives to be answered to a satisfactory degree. As such, RO-1 and RO-2 are prerequisite conditions for RQ-1, RQ-2 and RQ-3. RO-3 and RO-4 address the experimental component of the thesis, and are prequisites for RQ-4. Thus, if all research objectives are completed, all research questions will also be addressed.

Methodology

The work that has been conducted in this thesis can be separated into a numerical phase and an experimental phase.

Numerical Phase

The theoretical phase covers Research Questions RQ-1, RQ-2 and RQ-3, and is subjected to Requirements REQ-1, REQ-2 and REQ-3. This phase and will be mainly carried out through FEM analyses within ANSYS Magnetostatic Workbench. Throughout the literature study, most papers relied on FEM simulations for the approximation of bearing performance. This is is due to the fact that analytical solutions can be limited or non-existent, depending on the topic being studied. An overview of the software being used in the papers presented within the literature study can be found in Table 2.1.

Table 2.1: Simulation Methods Overview.

Paper	Simulation Scope	Software Used
Yonnet et al. [13]	Magnetic Field	FLUXLAB
Mystkowski et al. [20]	Magnetic Field	Comsol Multiphysics
Lijesh et al. [9]	Magnetic Field	ANSYS 2D
Hu e al. [33]	Magnetic Field	Comsol Multiphysics
Choi et al. [10]	Magnetic Field, Torques,	-not specified-
Liu et al. [23]	Torque characteristics	ANSYS Maxwell 3D
Bancel et al. [27]	Force Map	FLUX 3D
Jinji et al. [19]	Force and stiffness	-not specified-
Nielsen et al. [21]	Force and Stiffness	MagTense
Bjork et al. [26]	Force and Stiffness	Comsol Multiphysics
Feipeng et al. [17]	Force and Stiffness	-not specified-
Marth et al. [25]	Force and Stiffness,	FEMM, MagOpt
Moser et al. [18]	Radial Stiffness, Optimization	FEMM
Wu et al. [22]	Stiffness, Damping Coefficient	-not specified-

Another aspect that was considered during the planning phase of the theoretical phase was whether 2D or 3D simulations would be more beneficial for the purpose of assessing the performance of multipole bearings. In the work of Fitouri et al.[35] and Naik et al.[36] a comparative study is conducted between 2D and 3D ANSYS Maxwell simulation results, resulting in deviations as low as 2% and as high as 15%, depending on analysis parameters. Both papers conclude that 2D simulations would be more beneficial for preliminary designs, as the 3D simulations do not increase result accuracy to the same extent to which they increase computational time. A similar, although smaller in scale, study has been conducted in ANSYS Maxwell using a simple linear Halbach pattern. The case study resulted in a 8.77% difference in the magnetic flux density between 2D and 3D simulations, which falls within the values obtained by the previously mentioned papers.

However, in the case of the radially segmented multipole magnetic bearing simulations, 3D simulations will be used in order to obtain magnetic flux density results along the Z axis. Using 3D simulations will also help with the total number of simulations that need to be modelled, as studies of both radial and axial stiffnesses can be carried out using the same model project file.

Experimental Phase

The experimental phase of the thesis is the subject to Research Question RQ-4, and must satisfy Requirement REQ-4. Its focus is on bringing a variation of the final bearing design to reality through a prototype, with the goal of verifying results obtained in the first phase of the thesis. For this to happen, two main elements are needed: the magnetic elements forming the bearing array and a supporting structure which would allow for both axial and radial displacement, as well as accounting for the inevitable generation of an axial destabilizing force, while also allowing for the measurement of the various performance variables.

The magnetic elements would, ideally, be replicas of the ones presented in the theoretical design, however this would not be feasible from a manufacturing standpoint. As the magnetic elements that compose the multipole bearing arrays have unconventional magnetizations, they could not be procured via off-the-shelf component distributors. A brief study into the manufacturing processes of magnets was conducted, to assess whether or not it would be feasible to produce custom shaped magnets in-house.

Permanent magnets are manufactured through one of three different methods: sintered, bonded and additive manufacturing. The first method produces the most qualitative magnets in terms of performance, as it uses 100% magnetic powder as its base material. However, the heat treatments that are part of the manufacturing process would have required equipment which was not available. The other two methods employ a mix of magnetic powder (up to 80% [37]) and a polymer matrix as base materials. However, similar to the case of sintered magnets, steps within the manufacturing process would require inaccessible equipment. An in-depth description of the manufacturing processes of magnets can be found in the works of Cui et al. [38] [39], Li et al. [40], and Jafarzadeh et al. [41].

As a result of the manufacturing study, it was concluded that in-house manufactured magnets could not be a feasible solution, and thus off-the-shelf components would be the only solution. Companies which produce custom design magnets were also considered, but the cost of such a magnet would greatly surpass the budget for the prototype (quotes varied from 800€ to 10.000€) while also requiring a considerable lead time (>10 weeks could be expected). Thus, the search for magnetic elements was limited to off-the-shelf elements with conventional shapes. This in turn meant that the experimental setup would not be representative of the ”ideal” bearing design, but a simplified one which would be modelled based on the components found. More in-depth look on the simplified magnetic elements design can be found in Chapter 4.

The supporting structure of the bearing could be manufactured in one of two considered ways: additive manufacturing (3D printing) or CNC Machining. As the prototyping process usually implies multiple iterations and greatly benefits from rapid adaptations of designs, 3D printing was chosen as the manufacturing process. PLA was readily available, and as such was the chosen material for the structure, with component stiffness driven by the infill parameter. The structure was designed in such a way that the stator component of the bearing could be displaced axially, while the rotor could be radially displaced. An in-depth description of the supporting structure can be found in Chapter 4.

Measurements and Equipment

The test is planned to allow for the measurement of three different variables: generated radial stiffness, generated axial force, and generated magnetic flux density. For the measurement of the radial stiffness, a force gauge was intended to be employed, which would attach to the rotor of the bearing and thus produce a reading of the force necessary for a resulting, measurable, displacement. The axial force was measured through the use of a scale, on which the rotor of the bearing would be seated. The stator would then be lowered onto the rotor, decreasing the axial displacement between the two magnetic arrays in steps. Readings from the scale at those steps would then be converted into a force result and stored for comparisons with simulation data. The magnetic flux density was measured using a Gaussmeter. Measurements were taken of all magnetic elements within the array at the center point of the face perpendicular to the magnetization axis (where possible) with the help of a transversal probe. Readings were stored and compared to simulation data. Results and comparisons between measured and simulation data are presented in-depth in Chapter 4.

3

Configuration Designs and Simulations

This section of the thesis focuses on the numerical phase of the project. It starts with a general introduction to the simulation process conducted, where simulation parameters are presented and discussed. Following this, the four main categories of configuration simulations are presented: Monolithic Bearing Configurations, Segmented Bearing Configurations, Non-Symmetrical Bearing Configurations and finally Monolithic-Multipole Bearing Configurations. The last two categories build on the shortcomings of the segmented configuration and focus on the introduction of new design concepts in an attempt to better their performance. All chapters are further divided into a description of the configuration, where Total Magnetic Flux representations are used to help with the visualisation of the magnetic orientations and interactions, and a section on simulation data where results are analyzed.

3.1. Simulation Parameters

3.1.1. Material Definition

All simulations up to the experimental phase design simplifications have been utilizing Neodymium N45 as magnetic material. Within ANSYS Workbench, this material has been defined through a Linear "Hard" Magnetic Material template, which requires the Coercive Force and Residual Induction of the material as inputs. The coercive force considered is $9.24 \cdot 10^5$ [A/m], while the Residual Induction is 1.38 [T]. These two values have been sourced from a material data sheet of one of the magnetic providers employed in a previous work [42]. The second material needing to be defined within ANSYS Workbench is air, which was introduced through its Isotopic Relative Permeability of 1. For the analysis and implementation of steel elements within the magnetic arrays (Monolithic-Multipole Configurations), M3 Steel has been chosen from the Engineering Data Source available through ANSYS Workbench. This particular material has been selected based on the shape of its defined B-H curve (Figure 3.1) which, compared to other available materials, had a flatter evolution of the magnetic flux density with increasing magnetic field intensity. This translates to better simulation results, as the saturation behavior of this curve emulates the real material

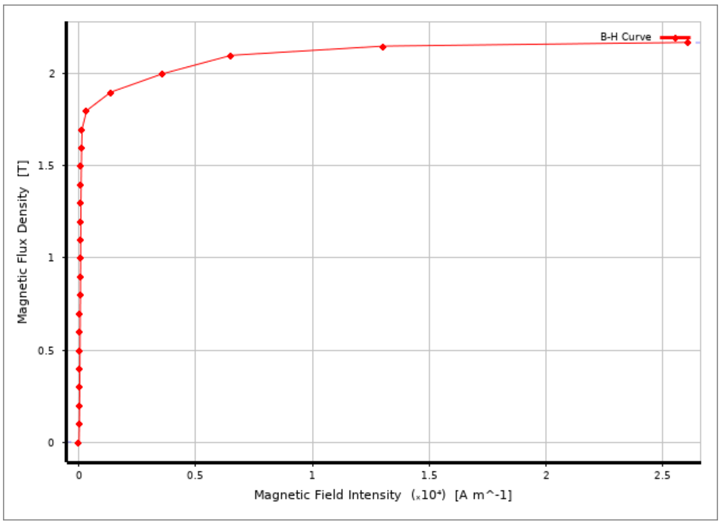

Figure 3.1: M3 Steel B-H Curve.

more closely. The magnetic properties of the magnets in the experimental phase [43] will be discussed more in-depth in the design simplification chapter.

3.1.2. Geometry Definition

The general dimensions of the bearing are presented in Tables 3.1 and 3.2. The other ever present component is the Enclosure, which varied throughout simulations in order to bring the total number of nodes below the student version limit (thus maximizing the number of elements employed in the meshing of the magnetic array and air-gap). Generally the enclosure outer diameter was 6 mm larger than the outer diameter of the largest magnetic array, and 6mm larger in the axial direction. The enclosure also features a 20 mm hole at its center, which also aids in lowering the total number of nodes without disconsidering performance-defining areas.

Table 3.1: Approximate Bearing Dimensions.

Array	**ID [mm]**	**OD [mm]**	**Height [mm]**	**Width [mm]**
Rotor Array	78	92	7	7
Stator Array	94	108	7	7

Table 3.2: ANSYS Workbench Geometry Definition.

Inner Median Radius [mm]	**Outer Median Radius [mm]**	**Cross-section Side [mm]**	**Air-Gap Median Radius [mm]**
42.5	50.5	7	46.5

3.1.3. Simulation Commands and Meshing.

As mentioned previously, ANSYS Workbench student features a 128k node limit. This did not prove to be an impediment in the simulation of most configurations, exceptions being large axial displacement simulations, where a maximum of 22 mm was achieve (with increasing axial displacement, the total simulation volume also increases, leading to more nodes being required to maintain the same mesh density). All simulations ran approached this limit, averaging around 126k nodes. The magnetic arrays were seeded radially in such a way that each element would cover a 2 degree arc, with the width and height of the array spanning 4/5 elements. The air gap interfaced the two magnetic arrays, and as such inherited their radial and height seeding. The width of the air-gap was only 1 element (2 elements were also tested, but results only differed by 2%). The mesh used in all simulations features Quadratic elements, primarily Tet10 (enclosure) and Hex20 (magnetic arrays and air-gap). The validation of the mesh has been carried out through the orthogonal mesh quality metric, with scores between 0.74 and 0.85, falling under the ”very good” element quality classification within ANSYS recommendations. The mesh quality distribution typically encountered can be observed in Figure 3.2.

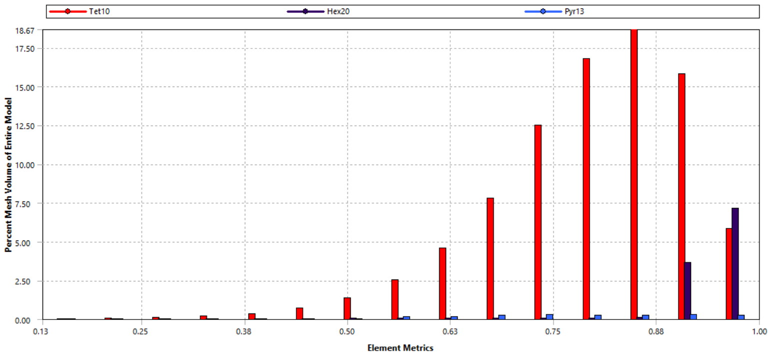

Figure 3.2: Ansys Mesh Element Quality Metric Graph for the Monolithic-Multipole Radial Focus Configuration.

The following command was employed in the simulation of the tangential magnetic elements, whose orientations can not be defined without APDL commands.

```
mpdele,mgxx,matid  ! DELETE X (OR RADIAL) COMPONENT MAGNETIZATION
Hc = -9.24e5 !
mp,mgyy,matid,Hc ! DEFINE Y (OR CIRCUMFERENTIAL) COMPONENT OF MAGNETIZATION
```

3.2. Monolithic Bearing Configurations

This section of the thesis project focuses on defining a baseline performance through simulations of conventional monolithic bearings. This design has long been utilized in the construction of magnetic bearings and are the basis of stacked multipole magnetic bearing configurations, as was discussed in Chapter 2.

Monolithic magnetic bearings which produce zero axial force are composed of two concentric magnetic elements with either radial or axial magnetizations. Radial monolithic bearings have the inner magnetic element oriented along the +R direction, while the outer magnetic element has the opposite -R magnetization. In this manner, the field lines are concentrated in the air-gap between magnetic elements, leading to slightly better radial stiffness performance when compared to their axial counterpart. Axial monolithic bearings are composed of two same orientation concentric magnetic elements, with orientations following either +Z or -Z directions. This configurations uses the magnetic field lines on the lateral sides of the magnet to provide the bearing's stiffness, and as a result the performance is slightly lowered by comparison. Performance metrics of both bearings are presented in Table 3.3.

Configuration	Air Gap AVG [mT]	Absolute Radial Force [N]	Axial Force [N]	Radial Stiffness [N/mm]
Monolithic Axial	695.21	-222.39	0.0097284	77.0
Monolithic Radial	776.91	-496.45	0.0097284	70.1

Table 3.3: Monolithic Magnetic Bearing Performance.

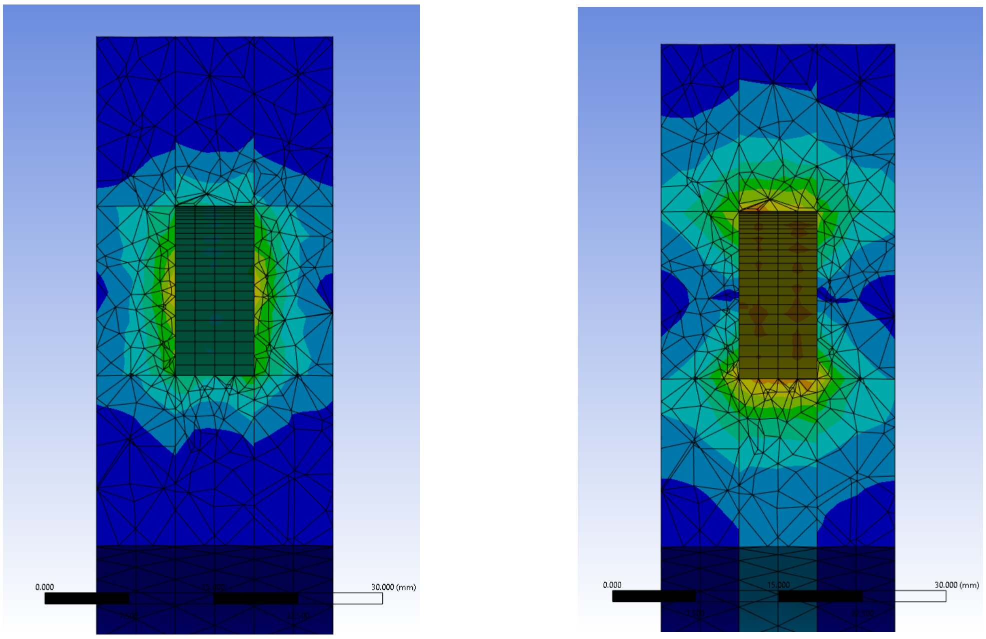

(a) Radial Monolithic Bearing.

(b) Axial Monolithic Bearing.

Figure 3.3: Radial Cross Section Comparison between Monolithic Bearing Enclosures of the Total Magnetic Flux Density.

Figures 3.23d and 3.24d offer a visualisation of the magnetic field through the total magnetic flux density parameter. The enclosure accounts for 10 mm on either side of the magnetic arrays along the Z axis, and 15 mm along the radial plane. The radial monolithic bearing offers a much smaller external magnetic field, and as a result it is characterized by less generated magnetic pollution. The axial bearing, unlike its radial counterpart, has both its main magnetic faces (North and South) open to the exterior of the bearing, translating a larger external magnetic field, unhindered by bearing interactions.

These total magnetic flux density simulations have also had paths traced along the main axes of the model (+Z, -Z, +R, -R) such that the external magnetic field can be qualitatively characterized. These are presented and discussed in-depth in section 3.5 of this chapter. The axial cross sections have been considered in Figures 3.4a and 3.4b. Through this visualisation it can be seen how the radial monolithic bearing has a considerably smaller external magnetic field, which is a desirable bearing behavior.

Monolithic magnetic bearings generate strong and constant throughout rotation magnetic fields, while keeping system complexity low. While their external magnetic field differ greatly, their performance is comparable, with the radial monolithic bearing prevailing with a slightly larger radial stiffness (+9.38%). Both monolithic configurations set good baselines for multipole magnetic bearing development, both in generated stiffness performance and through their considerable external magnetic fields.

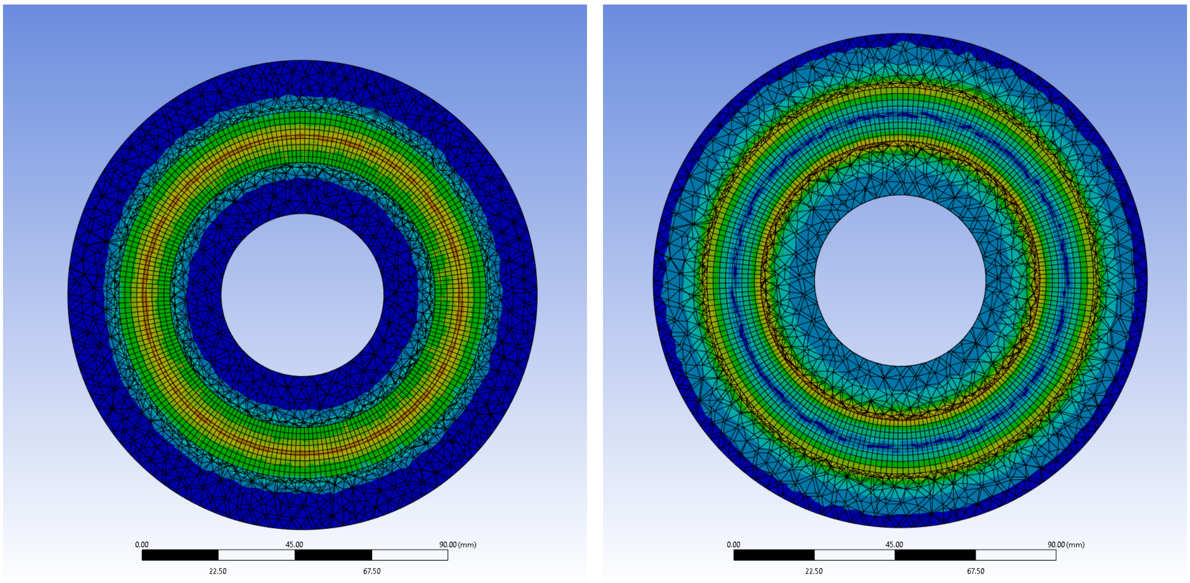

(a) Radial Monolithic Bearing.

(b) Axial Monolithic Bearing.

Figure 3.4: Axial Cross Section Comparison between Monolithic Bearing Enclosures of the Total Magnetic Flux Density.

3.3. Segmented Bearing Configurations

This section of the thesis addresses the first configuration architecture of multipole bearings tested and is split in two subsections. The first presents total magnetic flux visualisations of the generated magnetic field and defines configuration parameters, while the second discusses simulation results.

3.3.1. Configuration Description

The segmented configuration testing covered symmetrical magnetic arrays with 12, 16, 20, 24, 32, 36 and 40 segments. Three such configurations are pictured in Figures 3.5a, 3.5b and 3.5c.

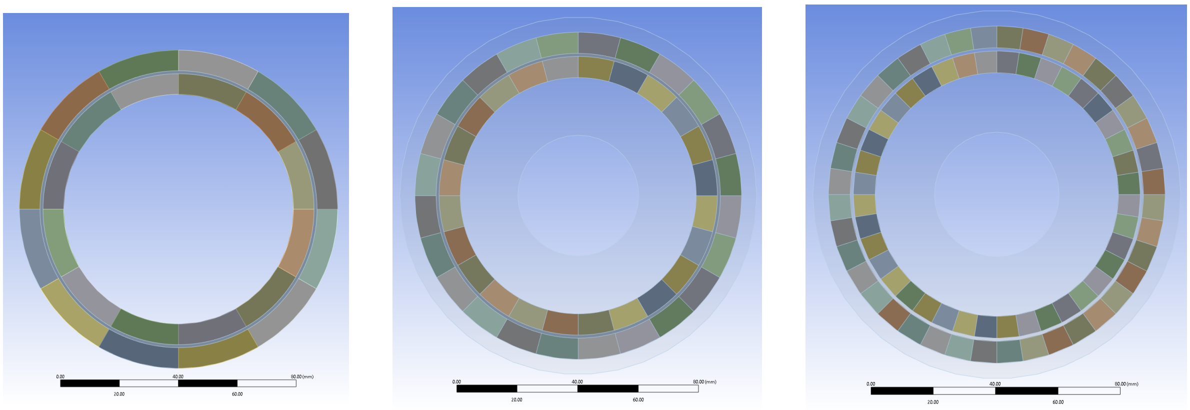

(a) Bearing with 12 segments per magnetic array.

(b) Bearing with 24 segments per magnetic array. Visible enclosure.

(c) Bearing with 40 segments per magnetic array. Visible enclosure.

Figure 3.5: Comparison between different segment number configurations.

Based on these bearing geometries, four different magnetization configurations have been studied. These are: Axial Halbach, Axial non-Halbach, Radial and Radial Focus. These configurations all differ based on the focus direction of the generated magnetic field. The focus direction is dictated by the orientation of the tangential magnetic elements with respect to their axial or radial counterparts. Magnetic orientation definitions are based on a cylindrical coordinate system, with the X axis representing the radial direction, the Y axis the circumferential direction (positive direction following an anti-clockwise motion) and the Z axis the axial direction.

The Radial Focus configuration is presented in Figures 3.6b and 3.7b, where different segment numbers are featured (12 and 40). This magnetic configuration features two different magnetization patterns, one for the outer magnetic array which focuses the magnetic field in the -R direction, and another for the inner magnetic array which strengthens the +R direction. These patterns are Tangential [+Y], Radial [+R], Tangential [-Y], Radial [-R] for the inner array, and Tangential [+Y], Radial [-R], Tangential [-Y], Radial [+R]. Through focusing the +R radial element with the tangential magnets on the inner array, the resulting magnetic field will be stronger on in the +R face of the array. Similarly, through focusing the -R radial element on the outer array, the resulting field is stronger on the -R face. This pairing of array magnetizations leads to increased magnetic field strength in the most crucial operational volume of the bearing - the air-gap. This can best be observed in Figure 3.7a, where a clear outline of the air-gap is visible.

Another observable difference between the 40 segment and the 12 segment configurations is the external magnetic field being generated, which is presented in Figures 3.6a and 3.7a. In the case of the 12 segment array, the magnetic field in both the +R and -R directions has a considerable reach, touching both outer surfaces of the enclosure, which is due to the fact that the individual magnetic elements have a longer arc-length. As a result of this, the magnetic field being generated by the magnet does not fully interact with adjacent elements on the basis of being too far apart. In the case of the 40 segment array this is no longer the case. With individual magnetic element arc-length being considerably shorter by comparison, they fully interact with adjacent segments, resulting in a much tighter spread of the external magnetic field. The internal (air-gap) magnetic field is also more defined in the 40 segment configuration, for the same reasons. As such, just from a total magnetic flux density visualisation, it

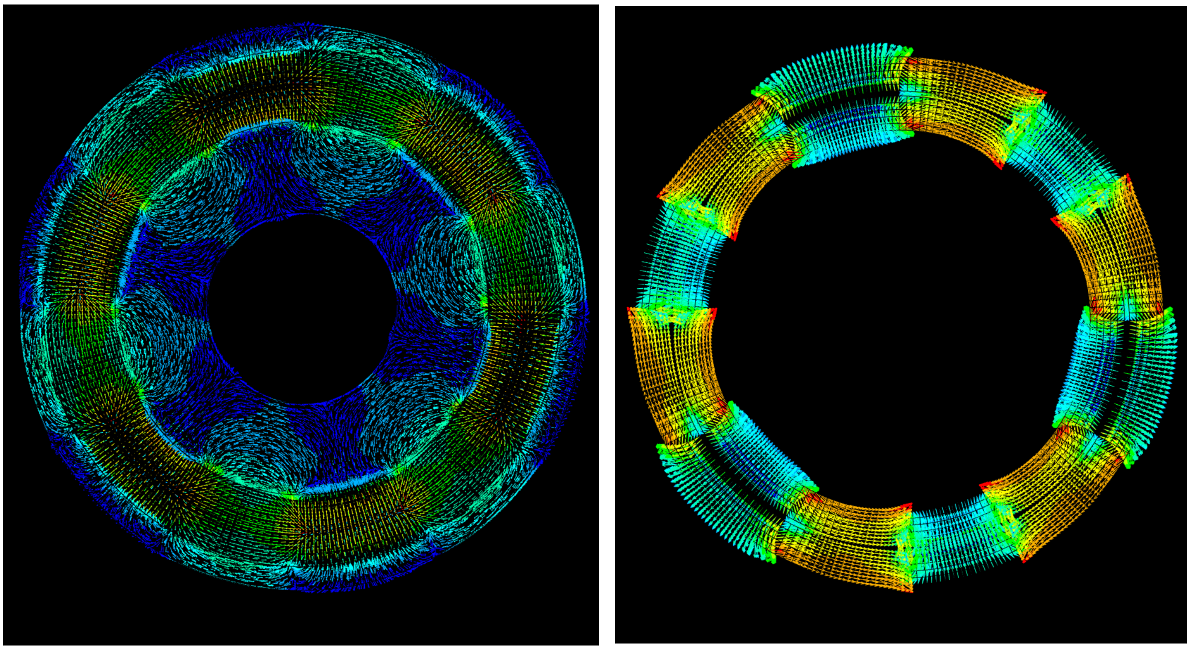

(a) Enclosure Total Magnetic Flux Density **(b)** Magnet Total Magnetic Flux Density - Vector Representation

Figure 3.6: 12-Segment Radial Focus Configuration - Total Magnetic Flux Density

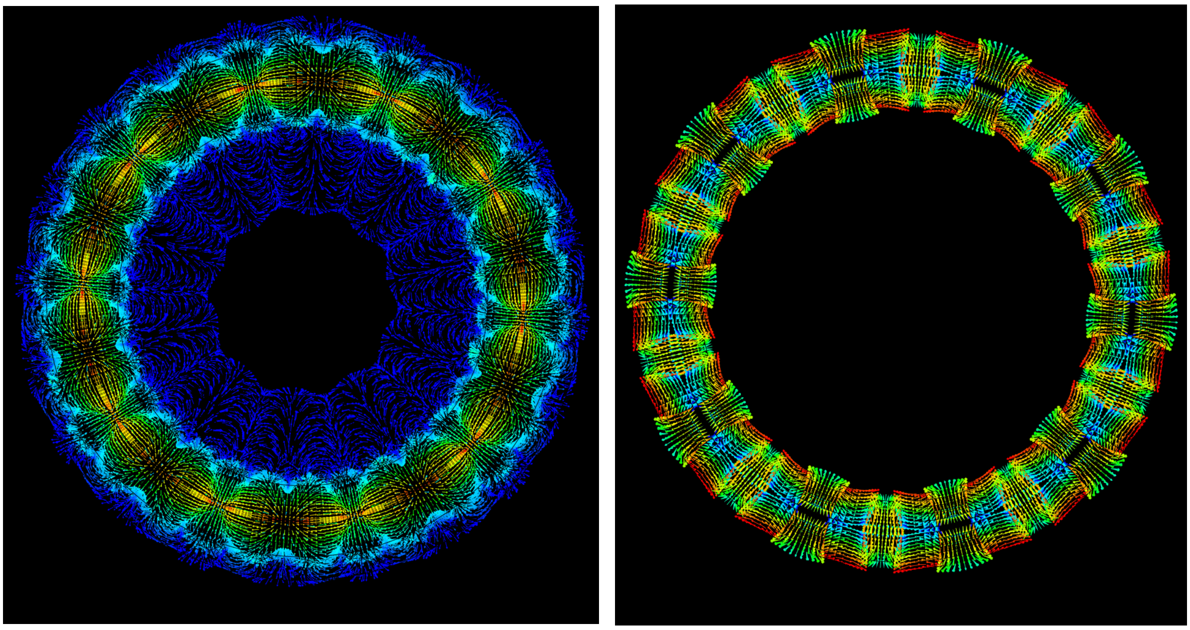

(a) Enclosure Total Magnetic Flux Density **(b)** Magnet Total Magnetic Flux Density, Vector Representation

Figure 3.7: 40-Segment Radial Focus Configuration - Total Magnetic Flux Density

can be concluded that increasing the number of segments per magnetic array will lead to an increase in magnetic field strength in the regions of interest. This will be qualitatively confirmed in the following section of the chapter, where analysis results are discussed.

The radial configuration is featured in Figures 3.8a and 3.8b, where similarly to previous configurations, the enclosure total magnetic flux density and the magnetic array vector representations are shown. The repeating pattern of the radial configuration features the same sequence on both magnetic arrays: Tangential [+Y], Radial [-R], Tangential [-Y], Radial [+R]. This leads to an unsymmetrical external mag-

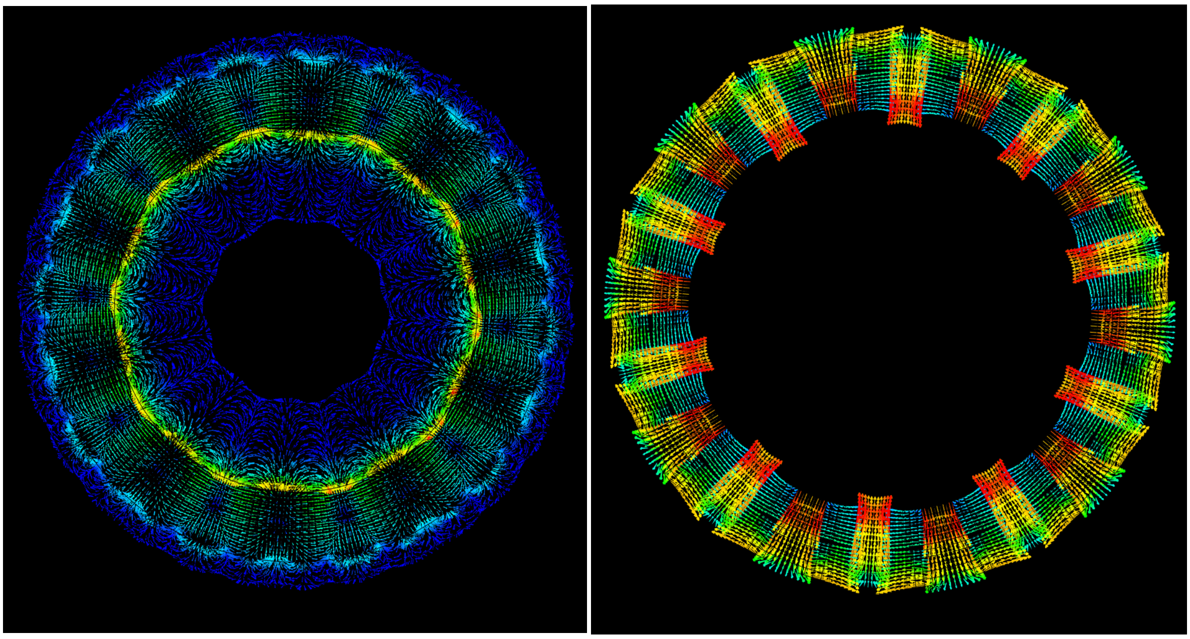

(a) Enclosure Total Magnetic Flux Density

(b) Magnet Total Magnetic Flux Density, Vector Representation

Figure 3.8: 40-Segment Radial Configuration - Total Magnetic Flux Density

netic field between in the radial direction. The focused -R magnetic elements lead to a much more concentrated flux line distribution on the inner face of the bearing compared to the outer one. This could be beneficial if the scope of the bearing would be the reduction in +R external magnetic pollution. However, in Figure 3.8b we can observe how this pattern leads to large sections with identical magnetic orientation. This in turn leads to radial instability and poor stiffness performance, as attraction forces dictate bearing behavior. This aspect of the radial configuration will be further discussed in the simulation results section of this chapter.

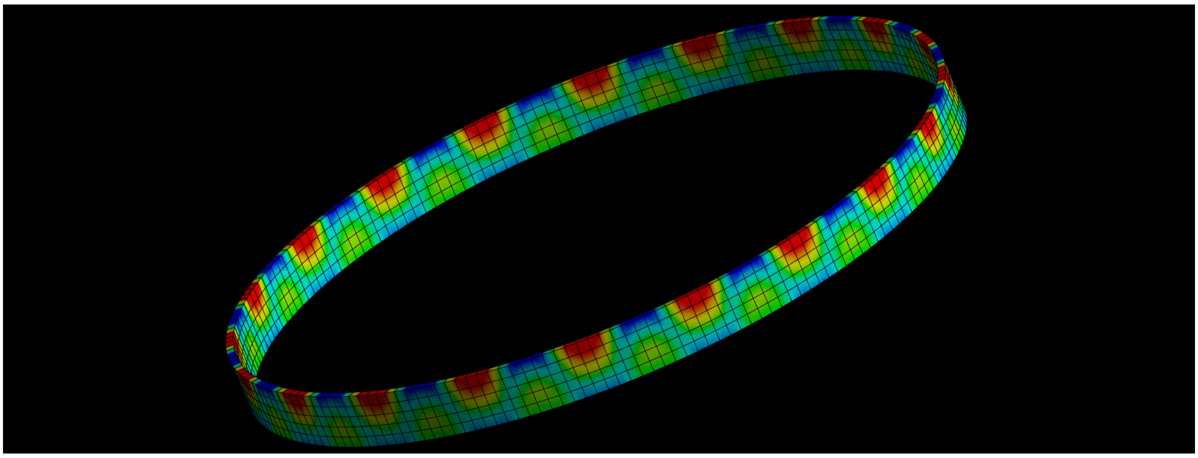

Figure 3.9: 40-Segment Axial Configuration Air Gap - Total Magnetic Flux Density

The axial Halbach configuration featured the following repeating pattern of magnetization: Tangential [+Y], Axial [+Z], Tangential [-Y], Axial [-Z]. In this pattern, the two tangential elements focus the magnetic field away from the -Z axial element, and strengthen the one generated by the +Z axial element. The resulting bearing generated magnetic field will be stronger on the +Z face of the assembly. Such a configuration can be observed in Figure 3.10. The difference between the axial vectors on the Z faces are the result of focusing the magnetic field. However, this gives the design an asymmetric axial

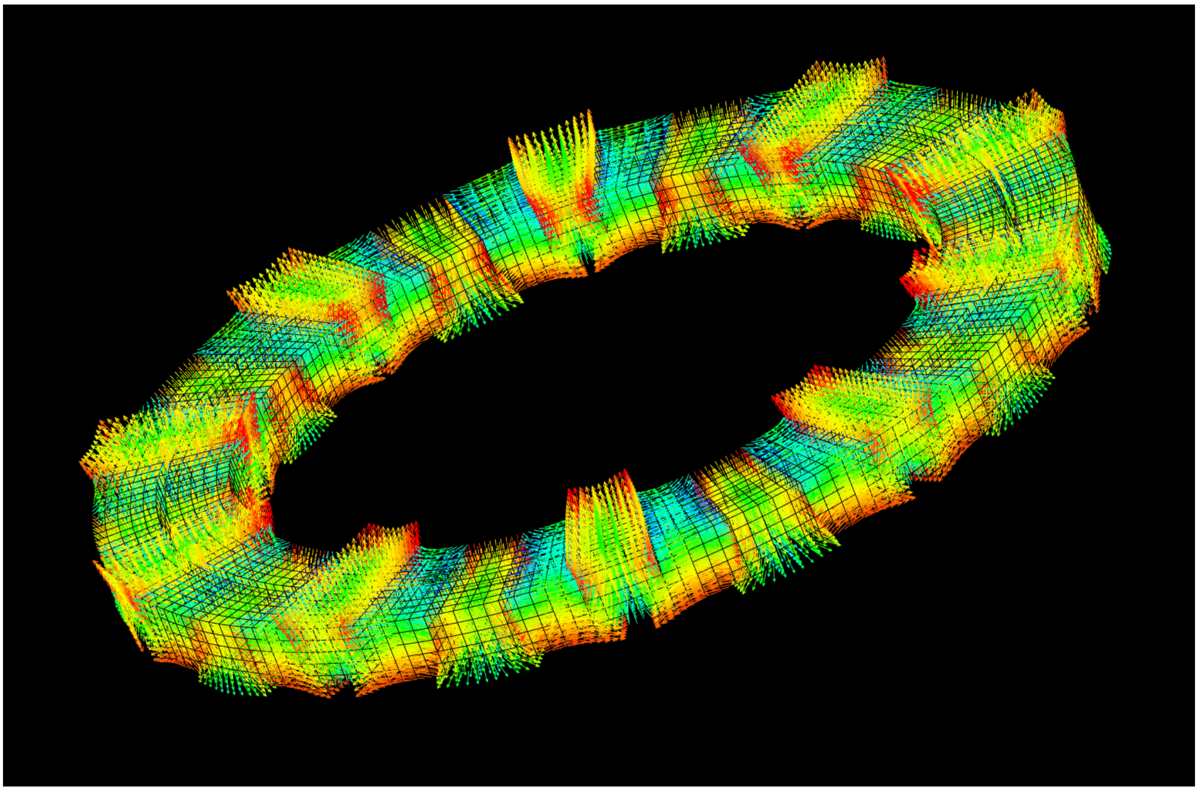

Figure 3.10: 40-Segment Axial Configuration - Total Magnetic Flux Density, Vector Representation.

magnetic flux distribution, leads to the exertion of axial forces even in a perfectly centered position. This is best observed in Figure 3.9, where high magnetic intensity areas are distributed along the +Z face of the air-gap, with the -Z face being considerably less magnetically dense. This behavior of the axial configuration was counteracted by altering the pattern of magnetization to only allow for either +Z or -Z orientations, which is known in this study as a Axial non-Halbach configuration. The performance of the bearing was typically unchanged, with the exception of the generated axial force under zero displacement, which is now zero. Further analysis of the configurations and their performance will be presented in the following section.

3.3.2. Simulation Outputs

This section of the chapter will focus on the analysis and interpretation of simulation results of the various segmented configurations defined in the previous section. Both the generated magnetic field and radial stiffnesses are considered in this section. All values are compared to their monolithic counterparts through percentage difference metrics. The general guidelines for good bearing performance are high magnetic flux density average in the air-gap, high (negative) radial force and zero axial force.

Tables 3.4 and 3.5 address simulation results of the Axial Halbach and Axial non-Halbach configurations. The first table focuses on magnetic field data and resulting forces as a function of the total number of segments used. The average magnetic flux density within the air-gap of the bearing has a downwards evolution with increasing number of segments. This is due to the fact that the elements are not focused towards the interior volume of the bearing, and as a result their interactions affect the exterior magnetic field more. However, the increased activity within the external field does cause an increase in the radial and axial forces being exerted on the bearing's rotor with increasing number of segments. The increase in absolute radial force can be a good indicator for the radial stiffness generated by the bearing, however it is not always representative and dedicated stiffness analyses need to be conducted. However, the increase in axial force is a downside of the axial configuration, which under an ideal bearing would be zero. This issue lead to the introduction of the non-Halbach axial configuration, whose performance is identical to its Halbach counterpart presented in the first table.

Table 3.5 showcases the difference in performance when it comes to axial force generation. By removing the axial magnetic flux gradient in the air-gap through only employing one axial magnetic orientation, it can be observed how the axial force drops from the 200N+ values generated by the Halbach configuration to the zero hovering values of the non-Halbach one. This concludes that the non-Halbach configuration would be the better configuration for a multipole axial bearing. By comparison to a monolithic bearing, the axial configuration underperforms in both average total magnetic flux density within the air gap (-31% to -37%) and the radial force generated (-50% to -55%). This decrease in performance is due to the reduction in volume of the axially magnetized elements. While in the monolithic configuration its entire magnetic volume is axially orientated and actively contributes to bearing performance, in the case of the axial configuration only 25% of the magnetic material is axially magnetized, the rest only contributing to closing the Halbach pattern and thus focusing the magnetic field to one side of the bearing.

Table 3.4: Axial Segmented Configurations Total Magnetic Flux Density Comparison to Monolithic Configuration.

Configuration	Air Gap AVG [mT]	% Difference	Radial Force [N]	% Difference	Axial Force [N]
AH 32	536.55	-31%	-221.91	-55%	122.27
AH 36	542.31	-30%	-235.51	-53%	159.59
AH 40	535.62	-31%	-242.12	-51%	189.62
AH 24	530.43	-32%	-246.57	-50%	208.95
AH 32	509.41	-34%	-244.38	-51%	224.83
AH 36	494.96	-36%	-239.31	-52%	223.53
AH 40	487.98	-37%	-236.31	-52%	216.9

Table 3.5: Generated Axial force by Halbach and non-Halbach Axial Segmented Configurations with different radial displacements (A=0.25mm, B=0.5mm, C=0.75mm).

Configuration	A AH [N]	A AnH [N]	B AH [N]	B AnH [N]	C AH [N]	C AnH [N]
32 Seg.	-225.300	0.026	-224.740	0.544	-224.960	0.665
36 Seg.	-222.970	0.135	-224.230	0.139	-222.900	0.248
40 Seg.	-217.650	-0.057	-216.360	0.992	-218.130	-0.504

The radial configuration is addressed in Table 3.6, where the same parameters are being studied. It can be observed how with an increasing number of segments both the total average magnetic flux in the air gap and the radial force increase. However, the radial force generated by this configuration is positive, which indicates attraction between the rotor and stator of the bearing. This leads to radial instability, as even small radial displacements will cause the attractive force to increase in the direction of the displacement, thus bringing the rotor and stator together instead of centering them. As such, the radial segmented configuration is not fit for multipole radial bearings, failing to fulfill requirements REQ-1 and REQ-2. In terms of generated magnetic field, the difference between the radial configuration and the monolithic bearing is smaller than the one observed in the case of the axial bearing, however it is still underperforming by a considerable amount in smaller segment number configurations.

Table 3.6: Radial Segmented Configurations Total Magnetic Flux Density Comparison to Monolithic Configuration.

Configuration	Air Gap AVG [mT]	% Difference	Radial Force [N]	% Difference	Axial Force [N]
R 12	520.38	-33%	305.43	+162%	0.14
R 16	569.84	-27%	305.39	+162%	-0.05
R 20	603.01	-22%	309.25	+162%	0.038
R 24	635.75	-18%	311.43	+163%	0.21
R 32	682.25	-12%	317.46	+164%	0.20
R 36	695.92	-10%	320.59	+165%	-0.11
R 40	715.44	-8%	321.27	+165%	-0.15

The radial focus configuration is featured in Table 3.7. Similarly to the radial configuration previously studied, both the average magnetic flux density in the air gap and the generated radial force increase with the number of magnetic segments employed. While the internal generated magnetic field is still smaller than the one produced by its monolithic counterpart, the radial force developed by the radial focus configuration overpasses monolithic performance starting 32 segments per magnetic array. In this case absolute radial force also translates to stiffness, which will be further explored in Table 3.8. The radial focus configuration is the first one to surpass the performance of the monolithic design, leading to the conclusion that it would be the best choice in terms of segmented designs for a monolithic multipole bearing.

Table 3.7: Radial Focus Segmented Configurations Total Magnetic Flux Density Comparison to Monolithic Configuration.

Configuration	Air Gap AVG [mT]	% Difference	Radial Force [N]	% Difference	Axial Force [N]
RF 12	472.75	-39%	-269.19	-46%	0.32
RF 16	526.88	-32%	-348.72	-30%	0.67
RF 20	572.73	-26%	-421.24	-15%	1.07
RF 24	615.74	-21%	-489.04	-1%	-0.29
RF 32	686.41	-12%	-604.42	22%	-0.70
RF 36	713.82	-8%	-649.89	31%	-0.17
RF 40	741.99	-4%	-693.16	40%	0.19

Table 3.8 presents stiffness data of all configuration types discussed thus far. For stiffness simulations the bearing rotor has been displaced along the Y axis by three different radial displacement values: A = 0.25mm, B = 0.5mm and C = 0.75mm. In each of these positions, the resulting centering force (or destabilizing in the case of the radial configurations) have been selected and translated to radial stiffness values. This process has been repeated for three segment number samples: 32, 36 and 40. From the table data it can be observed that the only configuration which provides a positive radial stiffness larger than the one generated by the monolithic bearing is the Radial Focus configuration. This is due to the fact that the magnetic field is concentrated in the "working" volume of the bearing, the air-gap. The radial focus configuration surpasses the monolithic bearing in stiffness by 41% to 65%. Both axial configurations offer a positive axial stiffness, which however underperforms by the same amounts as in the case of the air gap average total magnetic flux density. The radial configuration is the only one generating negative radial stiffness due to its attraction centric magnetic orientations.

As a result of instantaneous zero rotation performance analysis, the radial focus configuration offers the most performance out of multipole designs, followed by the axial non-Halbach configuration. The axial Halbach and radial configurations both cause bearing instability through either a non-zero axial force or a negative generated radial stiffness.

Table 3.8: Fadial Focus Segmented Configurations Stiffness Data Comparison with different radial displacements (A=0.25mm, B=0.5mm, C=0.75mm).

Configuration	A [N/mm]	B [N/mm]	C [N/mm]	Average	% Difference
Monolithic	80.88	76.66	78.97	79.50	0%
RF 32	112.7	110.35	112.23	111.76	**41**%
RF 36	119.47	114.26	121.96	118.56	**49**%
RF 40	130.60	130.32	133.47	131.46	**65**%
AH 32	55.14	51.56	53.59	53.43	-33%
AH 36	51.43	53.64	53.57	52.94	-33%
AH 40	53.54	56.28	55.50	55.11	-31%
AnH 32	53.96	51.56	53.61	53.05	-33%
AnH 36	49.11	53.64	53.90	52.22	-34%
AnH 40	51.33	56.28	57.47	55.03	-31%
R 32	-48.05	-49.84	-50.50	-49.46	-162%
R 36	-52.03	-51.67	-53.08	-52.26	-166%
R 40	-50.60	-51.99	-54.36	-52.32	-166%

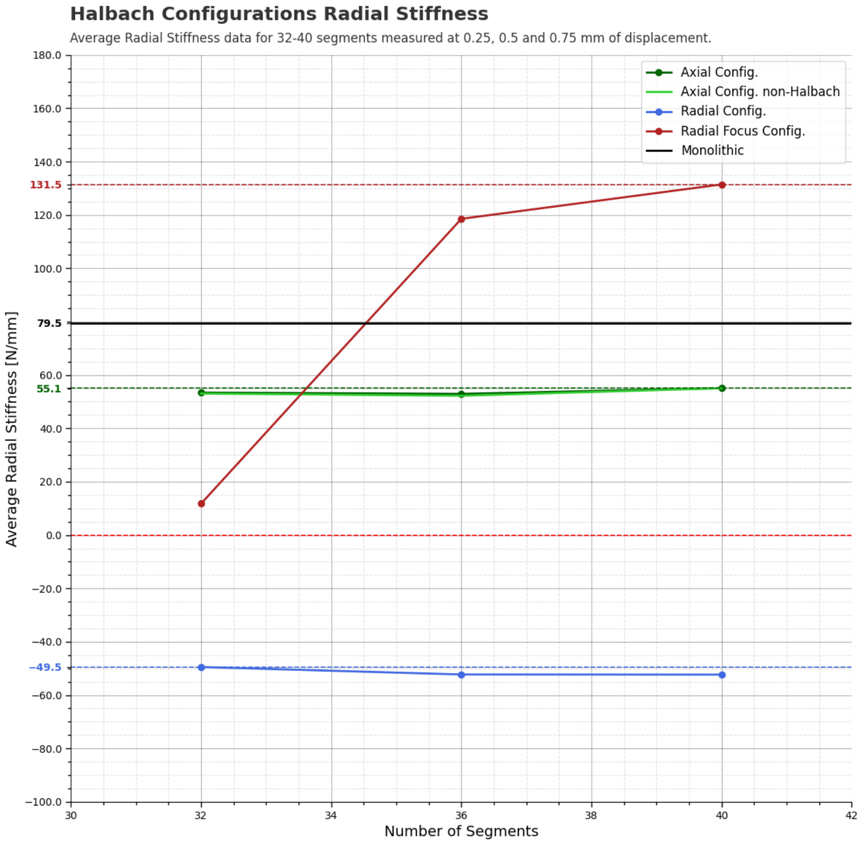

Figure 3.11: Generated radial stiffness as a function of total number of segments per magnetic array.

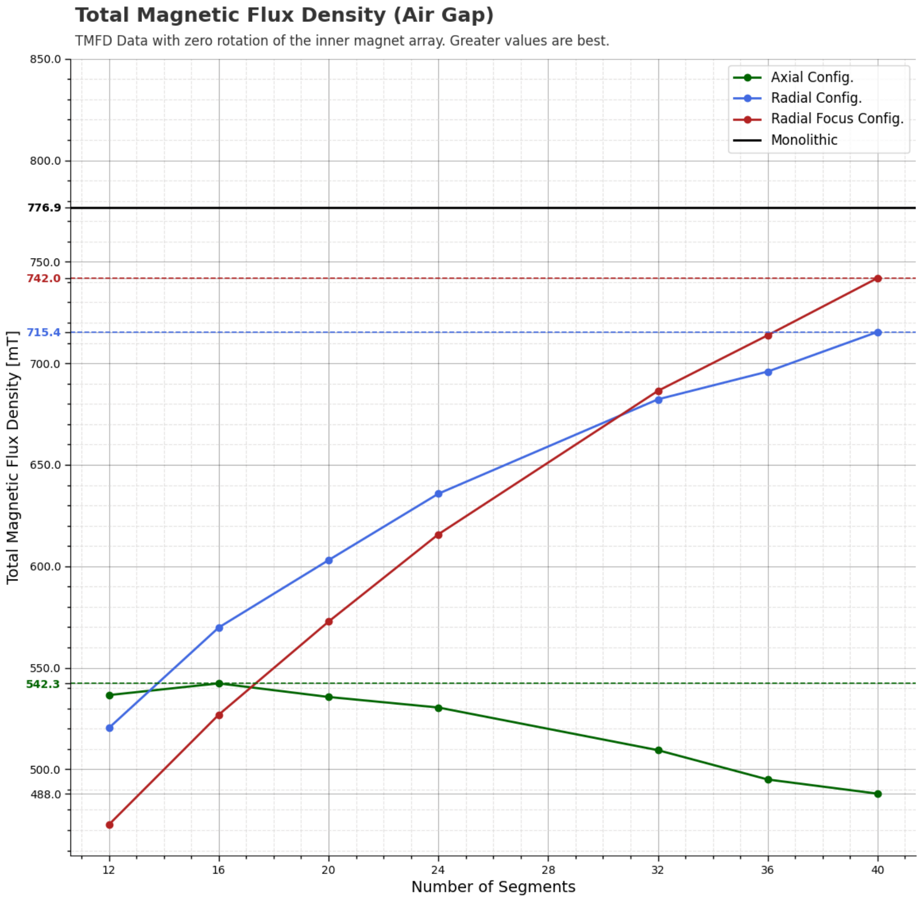

Figure 3.12: Generated average TMFD in the air-gap as a function of total number of segments per magnetic array.

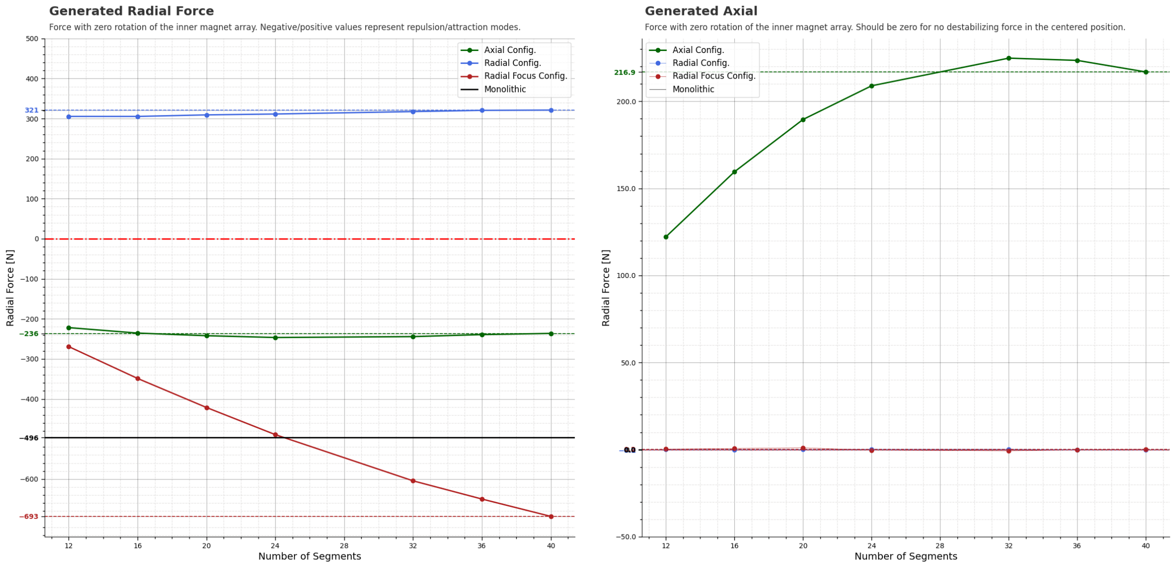

(a) Generated Radial Force.

(b) Generated Axial Force.

Figure 3.13: Generated forces as a function of total number of segments per magnetic array.

However, a bearing's successful operation implies relative motion between the stator and the rotor, which can have considerable effects on the performance of segmented magnetic designs. The effect of rotation on bearing performance will be now discussed, in the case of the configurations which achieve radial stability, through Figure 3.14. The figure shows the data discussed thus far as starting points for the rotational study. Both radial focus and axial configurations feature an increase in absolute generated radial force until 18 degrees in rotation, after which it drops back to starting values, completing the loop. As the 40 segment configurations are chosen, the entire Halbach pattern repeats every 36 degrees (9 degree arc per magnetic element). The peak generated radial force is encountered at the halfway point, or at a 2 segment arc distance. This translates to a 2 segment relative offset between the Halbach patterns encountered on the rotor and the stator. As a result, rotor magnetic elements which started as having reversed magnetizations to that of the opposing magnets on the stator, now face same orientation magnets. This leads to attraction forces being generated instead of repulsion ones. Figure 3.14 marks this switch between repulsion and attraction mode through the points where the radial force crosses the zero mark, going from negative to positive. This behavior of the two configurations means that the bearing is radially stable for only half its complete rotation, with intermittent sections in which the acting forces do not center the rotor, thus failing requirement REQ-2.

In conclusion, none of the segmented bearing designs fulfill all requirements, and as such none are fit for implementation on a RWA multipole magnetic bearing.

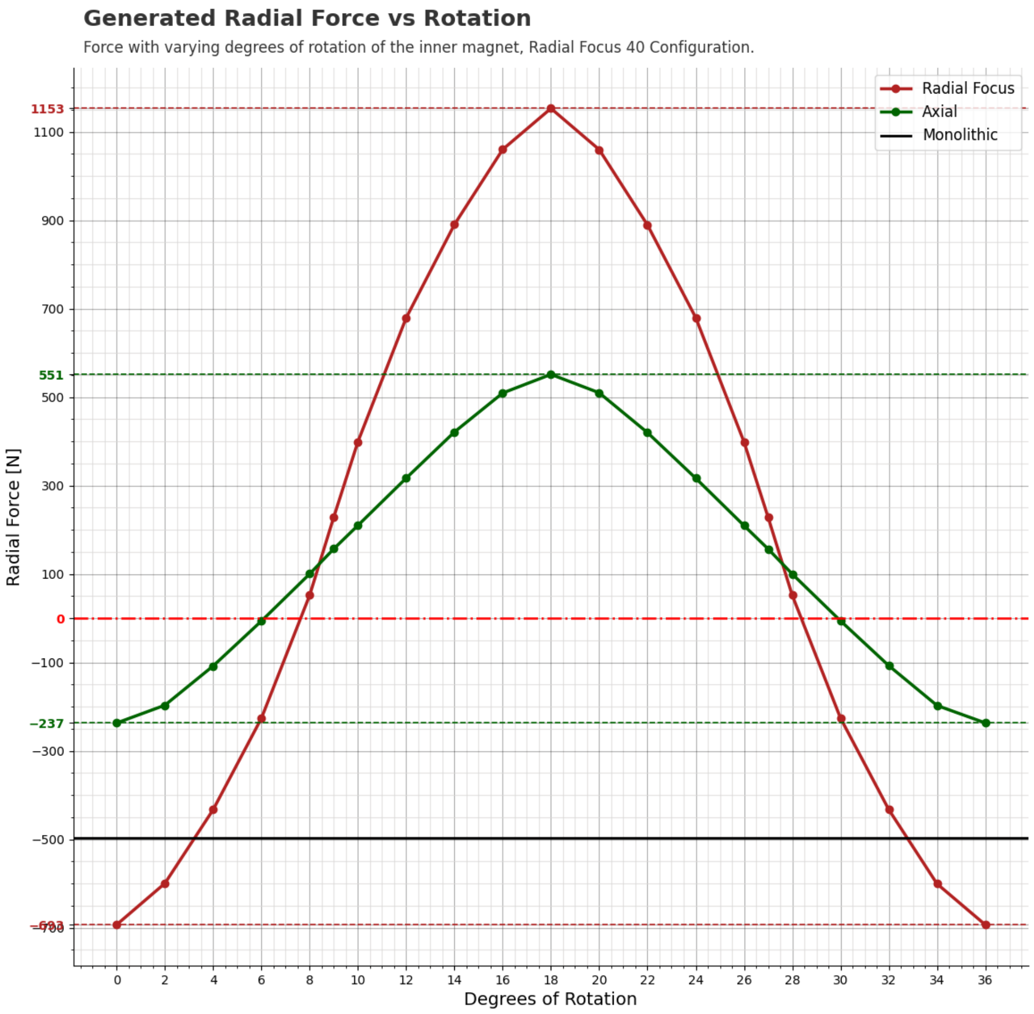

Figure 3.14: 40-Segment Axial Configuration - Total Magnetic Flux Density, Vector Representation.

3.4. Non-symmetrical Bearing Configurations

3.4.1. Configuration Description

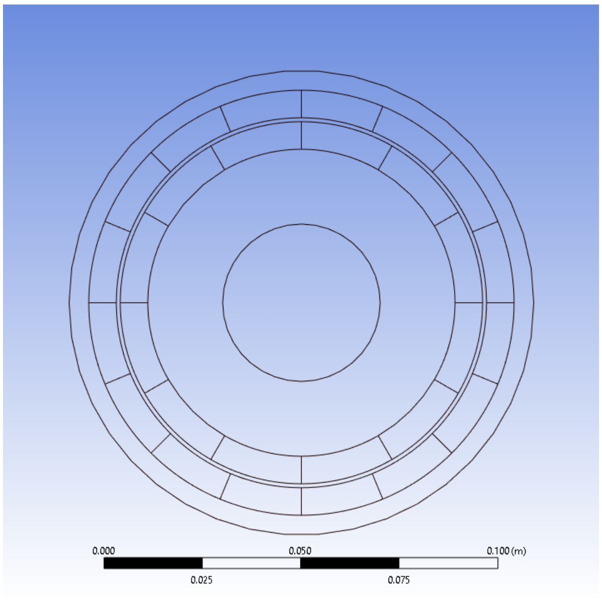

Figure 3.15: Non-symmetrical Configuration Geometry, 0.75 Ratio.

Non-symmetrical bearing configurations attempt to build on the shortcoming of the previous configurations studied, the simple segmented magnetic designs. The core issue with the performance of these segmented configurations was the intermittent switching between attraction and repulsion mode within the bearing's rotation, which would lead to loss of bearing stability. The main cause for this behavior was the overlapping of attraction mode magnets at intervals equal to half the arc-length of the Halbach pattern (18 degrees in the case of a 40 segment array). In an attempt to counteract the overlapping of these magnets, a ratio between the number of magnetic segments on the rotor and the stator was introduced. The thought behind the implementation of this ratio was that through the use of non-symmetrical layouts, no magnetic pairs with attraction generating magnetizations could be independently overlapped. Although overlaps would still be possible, the adjacent magnets would also be part of the overlapping sectors. Depending on the ratio used, the effect of the adjacent magnets would increase or decrease. To this effect three different ratios were considered: 0.3, 0.5, 0.75, 1.33, 2, and 3, which were achieved through the following pairings of magnetic segments for the rotor/stator : 12/36, 12/24, 12/16, 16/12, 24/12, 36/12. Upon simulating the first few configurations, it was observed that reversed configurations such as 12/36 and 36/12 would produce the same results, regardless of magnetization pattern. As such, in the results presented here only the following ratios will be discussed: 0.3 (12/36), 0.5 (12/24) and 0.75 (12/16).

Figure 3.16 shows the air-gap total magnetic flux density of a 0.75 ratio configuration, with radial magnetization. It can be seen from the distribution of the magnetic field that asymmetric magnetic arrays lead to asymmetric regions within the air-gap volume, which translate to higher radial forces being exerted in those particular regions. However, through the non-symmetrical nature of the design, the summation of all these regions will no longer give a null result, as was the case with the segmented configurations. As a result, the total sum of forces acting in the radial plane along the Cartesian X and Y axis will no longer cancel out, leading to radial destabilization, behavior which will be exemplified in the following section.

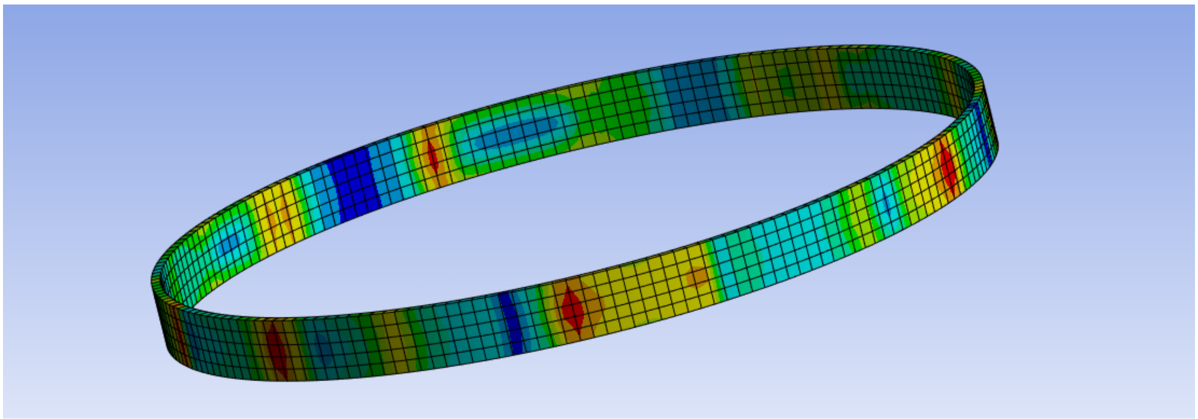

Figure 3.16: Non-symmetrical Radial Configuration, 0.75 Ratio, Air Gap TMFD.

3.4.2. Simulation Data

As discussed in the previous section, the main scope of the non-symmetrical configurations was the avoidance of attraction and repulsion regions in the rotation of a segmented bearing design. This aspect is featured in Figures 3.18a, 3.18b, and 3.18c, where the absolute radial force is plotted as a function of rotation angle. In the case of ratios 0.5 and 0.75, the switch between magnetic interaction modes stopped, however it was now positive across the entire bearing rotation. This would translate to constant attraction between the rotor and stator of the bearing, leading to radial instability. In the case of the 0.3 ratio, the generated absolute radial force only stopped mode switching for the radial focus configuration, but not its variation across bearing rotation. For the radial and axial configuration, mode switching still occured. As a result of these radial force behaviors, none of the ratios achieved radial stability, and as such could not be integrated into a RWA bearing.

The main cause for this result is the manner in which non-symmetric bearings handle the ”transition” between magnets. With magnetic elements now overlapping more than just one other magnet, the steep increase in radial force encountered with segmented designs is no longer present, as the larger overlaps ”average” the magnetic interactions in the air-gap volume. As the maximum attraction between two identical magnetic elements is stronger than their maximum repulsion, the average between the two will result in a positive (attraction) absolute radial force. Figures 3.18d, 3.18e, and 3.18f address the total magnetic flux density within the air gap. In this case, with increasing ratio between magnetic arrays, both the average value and the oscillatory behavior is reduced. The least affected by ratio configuration is the axial one, which does not focus the magnetic field in the air-gap, and as such the number of magnetic orientations interacting has less of an impact (as was the case with the number of segments).

An additional property of non-symmetric bearing is the generation of destabilizing Cartesian forces when the ratio does not allow for an exact number of magnets to overlap. Ratios 0.5 and 0.3 are safe as the number of segments employed results in 2 (12/24) and 3 (12/36) magnetic elements being overlapped at once. For ratio 0.75, this is no longer the case. This causes the summation of X and Y forces in the radial plane to no longer equate to zero, as exemplified in Figure 3.17.

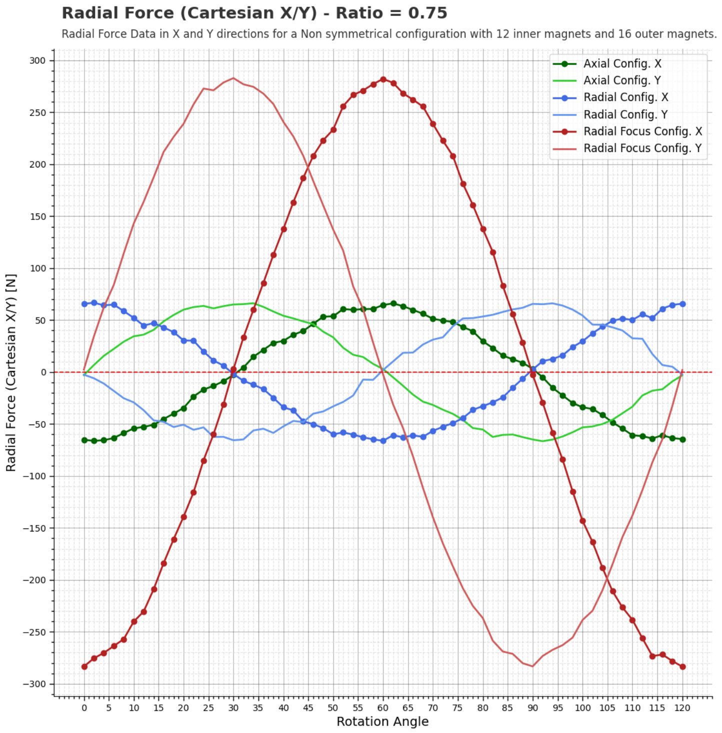

Figure 3.17: X and Y Forces for Non-symmetrical bearing configurations.

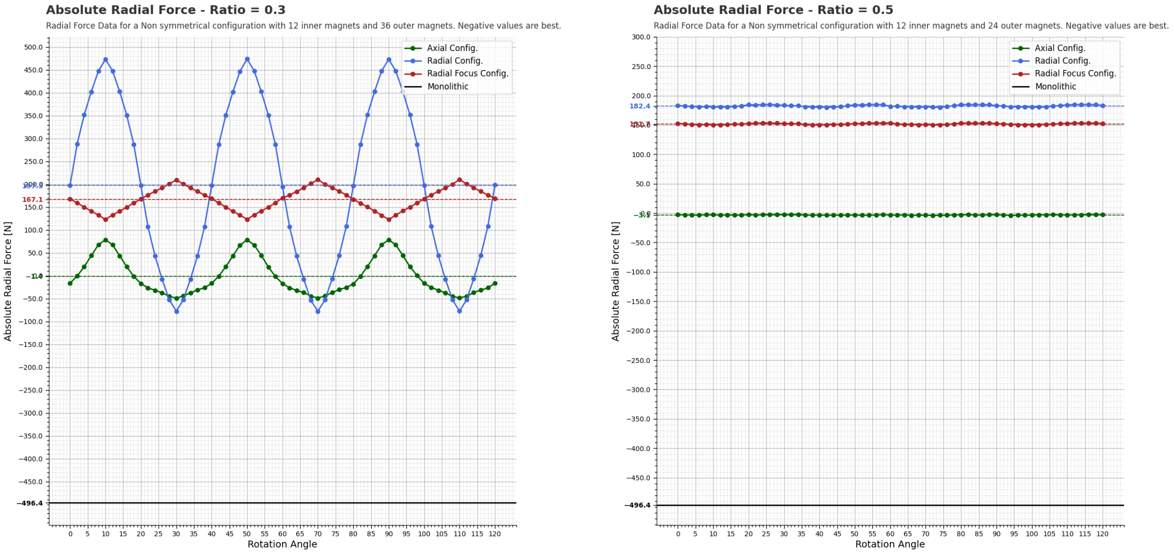

(a) Absolute Radial Force, Ratio 0.3 (12/36)

(b) Absolute Radial Force, Ratio 0.5 (12/24)

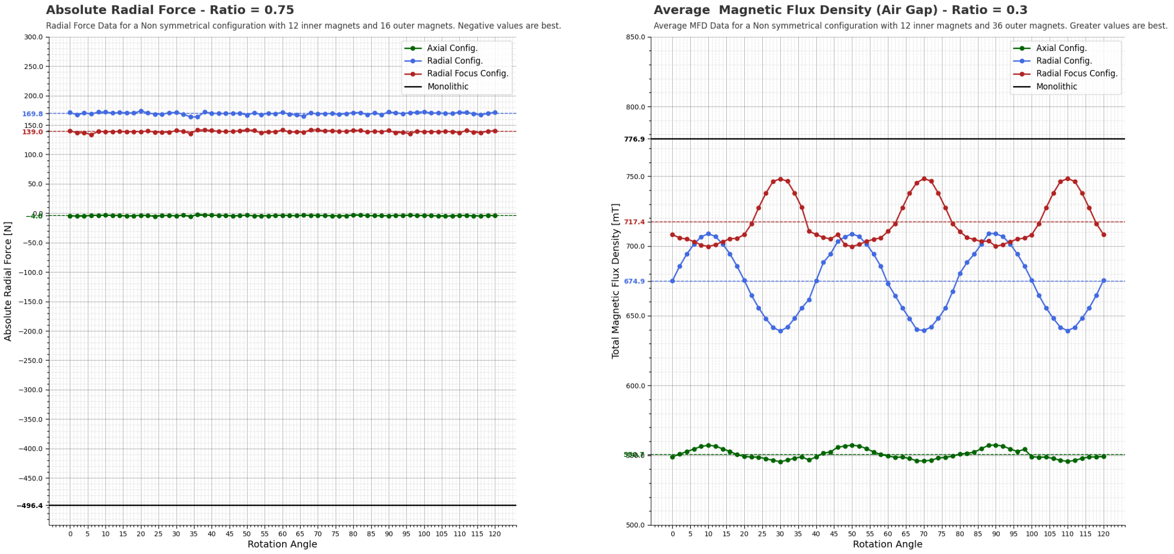

(c) Absolute Radial Force, Ratio 0.75 (12/16)

(d) Average Magnetic Flux Density (Air Gap), Ratio 0.3 (12/36)

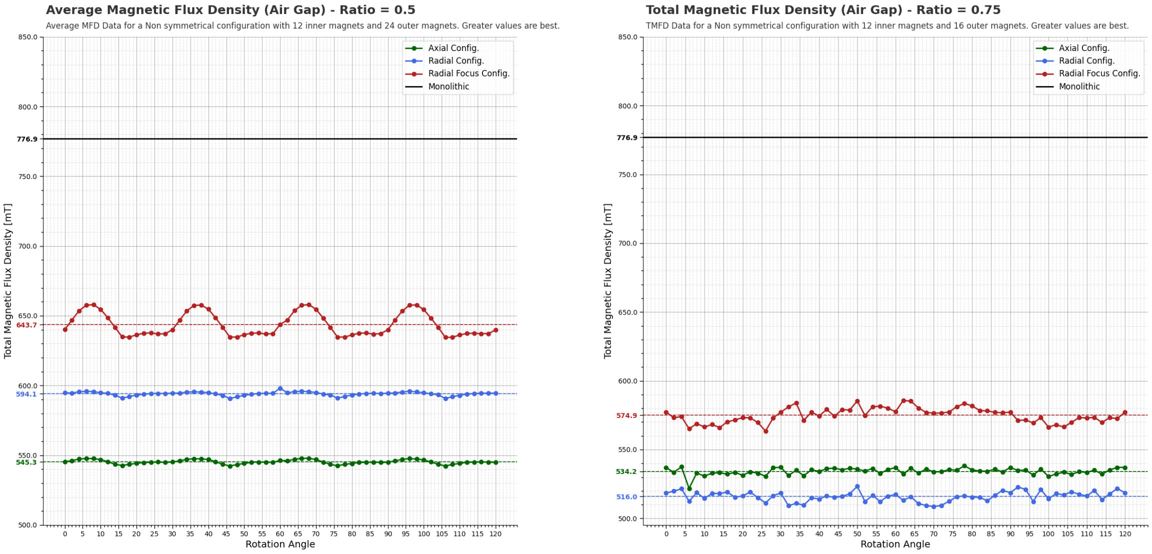

(e) Average Magnetic Flux Density (Air Gap), Ratio 0.5 (12/24)

(f) Average Magnetic Flux Density (Air Gap), Ratio 0.75 (12/16)

Figure 3.18: Non-symmetrical Bearing Configurations Simulation Data.

3.5. Monolithic-Multipole Bearing Configurations

The development of the Monolithic Multipole bearing configurations started from the continuous problem of the oscillatory behavior of the bearing's performance with respect to its rotation. A first attempt at mitigating this issue has been the introduction of non-symmetric bearing configurations, but they too suffered from the same problem (depending on the ratio used), while also introducing X and Y unbalance forces. The core issue in both configuration types tested so far has been the interaction between the rotor and stator magnetic elements, which would overlap and introduce attraction forces into the system. In order to avoid this issue altogether, the idea of replacing one of the multipole magnetic arrays with a monolithic one will be tested in this chapter of the thesis. In this manner, the overlapping problem will no longer exist, as all multipole elements will face a constant magnetic field regardless of rotation angle.

3.5.1. Configuration Description

The concept of the monolithic-multipole configurations started with the replacement of the outer magnetic array with either an axial monolithic bearing for the axial configurations, or a radial monolithic bearing for the radial focus configuration. Initial simulations of these configurations resulted in constant, positive radial stiffness performance across the entire rotation range of the bearing. The radial focus monolithic configuration generated a radial stiffness of 7.1 N/mm, while the axial Halbach configuration produced 42.1 N/mm. These values, although still considerably underperforming by comparison to a conventional monolithic bearing, were the first configurations which produced constant performance across a full bearing rotation, while satisfying all requirements set.

Simultaneously with the development of monolithic-multipole configurations, the concept of "working" and "pattern completion" magnets was defined. "Working" magnets were the ones actively contributing to the stiffness generation. Such magnets were the ones being focused by the tangential magnetic elements, and the ones which were always in repulsion with the monolithic magnet. "Pattern completion" magnets were represented by both tangential and defocused magnets, which would always be in attraction to the monolithic one. The next step in the search for a configuration which would generate a constant radial stiffness was the reintroduction of the ratio concept. However, in this second iteration, the ratio would refer to individual magnetic elements within the magnetic arrays, putting more emphasis on the "working" magnets. Two ratios were considered and tested: 1:2, 1:3. The 1:2 ratio tested a configuration in which the magnets that had either radial or axial magnetizations would have their arc-length twice that of the tangential elements. The concept behind this configuration was the fact that tangential elements would also enter attraction mode throughout rotation (when they overlapped an opposing orientation element), and reducing their area of magnetic interaction could better bearing performance. The 1:3 configurations followed the same concept, but with axial or radial magnets having three times the arc-length of their tangential counterparts. However, the simple reintroduction of the ratio concept did not improve the performance enough, as oscillations in radial stiffness were still appearing.

At this point, the previous two concepts described, monolithic-multipole configurations and the magnetic array internal ratios were combined. While the implementation of the monolithic bearing would provide a constant magnetic field on which the multipole array could rest, the ratio would strengthen the contribution of the "working" magnetic elements and thus increase bearing performance. As such, the 5-5-5-15 Monolithic-Multipole configuration was defined. The ratio in this configuration would result in the "working" axial or radial magnet having three times the arc-length of all other magnets within the Halbach pattern. The numbers in the configuration name refer to the arc of the individual segments, in degrees. (15 degree working magnets - 5 degree pattern completion magnets). In this manner, the magnet which would have the largest contribution to the radial stiffness would also have the most air-gap volume at its disposal.

The axial cross sections of the non-monolithic radial and axial, yet ratio integrated configurations can be observed in Figures 3.19a and 3.19b. The first observation that can be made is the enclosure pattern caused by the ratio. In figure 3.19a, the high magnetic flux areas imprinted onto the enclosure follow the 15 degree elements, with the smaller patches representing the 5 degree elements with axial magnetizations. In figure 3.19b the high magnetic flux areas within the air gap are also caused by the 15 degree and 5 degree radial elements, with lower magnetic flux areas in the spots where tangential magnets would be. The exterior magnetic field is also noteworthy for the radial 5-5-5-15 configuration, as pockets of high magnetic flux density would form in both +R and -R directions at the faces of the 15 degree elements.

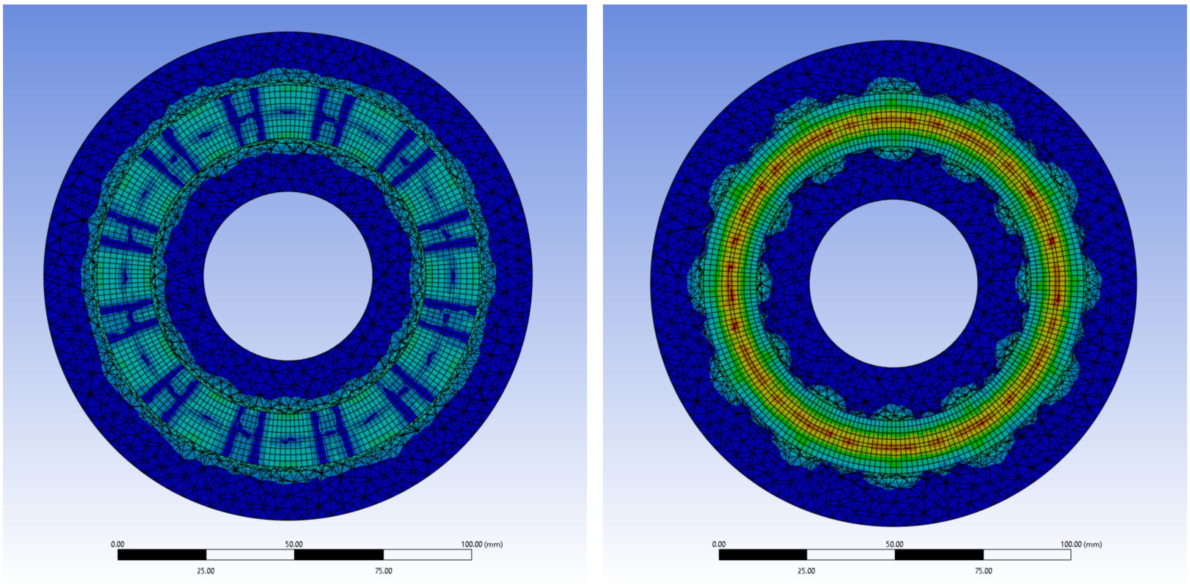

(a) Axial Halbach Configuration. **(b)** Radial Focus Configuration.

Figure 3.19: 5-5-5-15 Configurations Axial Cross Section Magnetic Flux.

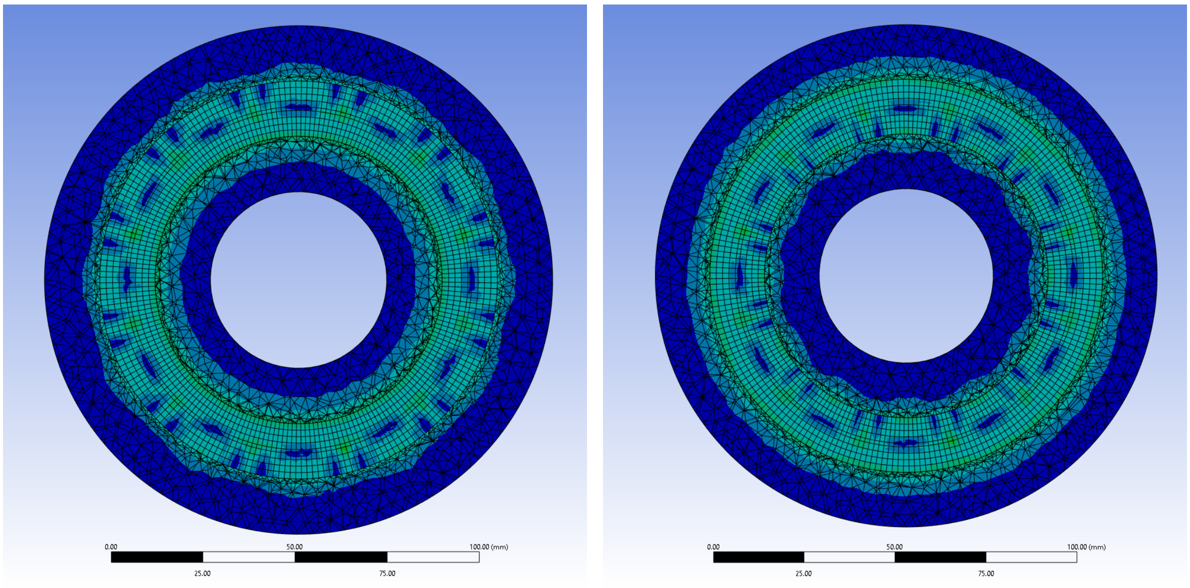

(a) Monolithic Axial Halbach Configuration. **(b)** Monolithic Axial Halbach Reversed Configuration.

Figure 3.20: Monolithic Axial Halbach 5-5-5-15 Configurations, Axial Cross Section Magnetic Flux.

Figure 3.20a and 3.20b feature the fully implemented monolithic-multipole 5-5-5-15 axial configuration, together with its reversed version (the monolithic magnet would now be on the outer portion of the bearing). An interesting feature of this configuration is that both the external and internal magnetic fields are different on the +R and -R sides of the bearing, based on magnetic array placement. If the multipole array is on the outside, as is the case with 3.20a, the +R external field will be inherited from the non-monolithic configuration. Therefore, each magnetic array imposes its own field ”print” on the closest volume. Similarly, figure 3.20b has had its +R external field defined by the constant monolithic magnetic field. This behavior of the external volumes of the bearing also apply to all other 5-5-5-15 monolithic configurations. In figures 3.21a and 3.21b the axial non-Halbach configuration is featured. As the name implies, the configuration does not follow a typical Halbach pattern, and as such the generated magnetic field is more similar that of a monolithic bearing than that of its axial Halbach counterpart. This will further be exemplified in the interpretation of the radial cross sections of the various configurations later in this chapter.

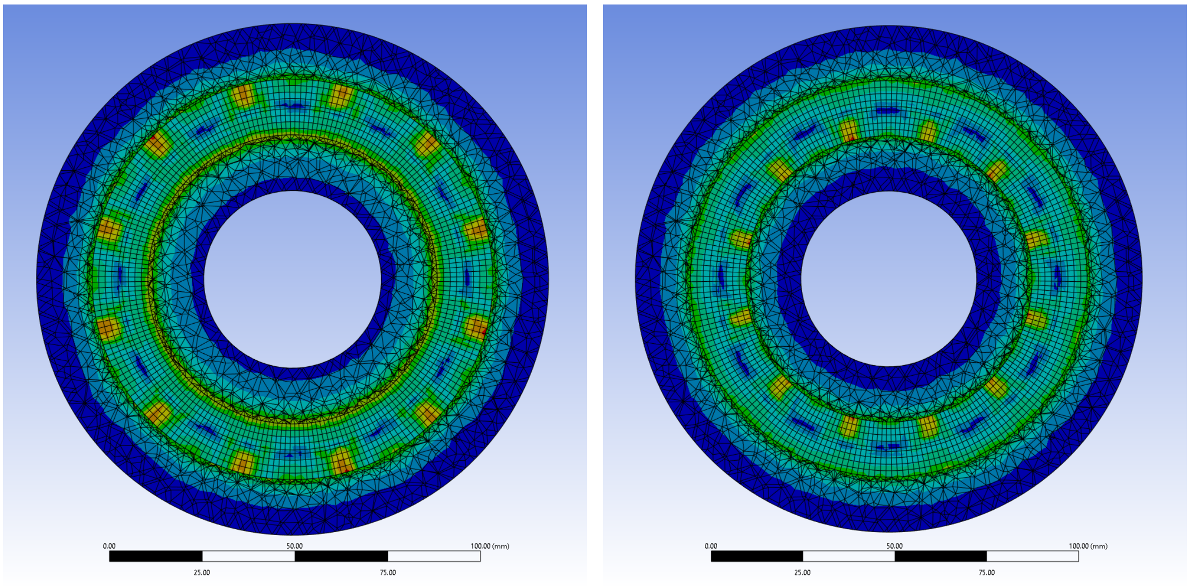

(a) Monolithic Axial non-Halbach Configuration

(b) Monolithic Axial non-Halbach Reversed Configuration

Figure 3.21: Monolithic Axial non-Halbach 5-5-5-15 Configurations, Axial Cross Section Magnetic Flux.

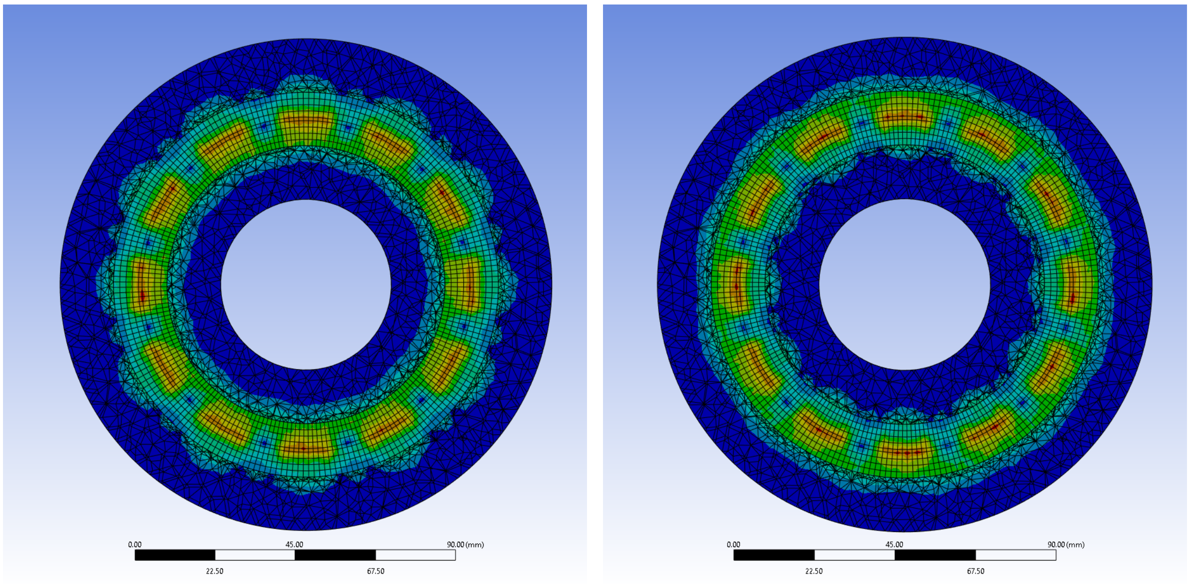

(a) Monolithic Radial Focus Configuration

(b) Monolithic Radial Focus Reversed Configuration

Figure 3.22: Monolithic Radial Focus 5-5-5-15 Configurations, Axial Cross Section Magnetic Flux.

Figures 3.22a and 3.22b present the radial focus 5-5-5-15 monolithic-multipole configuration. Similarly as before, the 5-5-5-15 radial focus non-monolithic external magnetic field can be seen in both images, on the side of the multipole array. It is also worth mentioning that this configuration produces the least amount of magnetic pollution in its external volume, which will be one of the defining factors in the choice for the best configuration at the end of this chapter.

The following three sets of figures feature the radial cross sections of the different 5-5-5-15 monolithic-multipole configurations. The main takeaways from these figures are the amount of magnetic pollution generated in the Z and R directions. For each of the cross sections, the +Z direction is to the left of the figure, with the +R direction being towards the top of the figure.

The axial Halbach configuration, seen in Figure 3.23a keeps its external magnetic field primarily focused on the +Z face, as would be expected of the configuration. The introduction of the monolithic bearing into this configuration slightly lowered its focus effectiveness, however it can still be observed in Figures 3.24a and 3.25a. By comparison, the axial non-Halbach configuration loses most of its focus with the implementation of the monolithic bearing, and as such is considered the worst performing monolithic-multipole configuration.

On the other hand, the radial focus configurations features a reduction in external generated magnetic field with the introduction of the multipole magnet. This can be observed in Figures 3.24c and 3.25c, where the external magnetic field is considerably reduced on the side of the multipole array by comparison to its non-Halbach counterpart, making it the main benefit of this configuration.

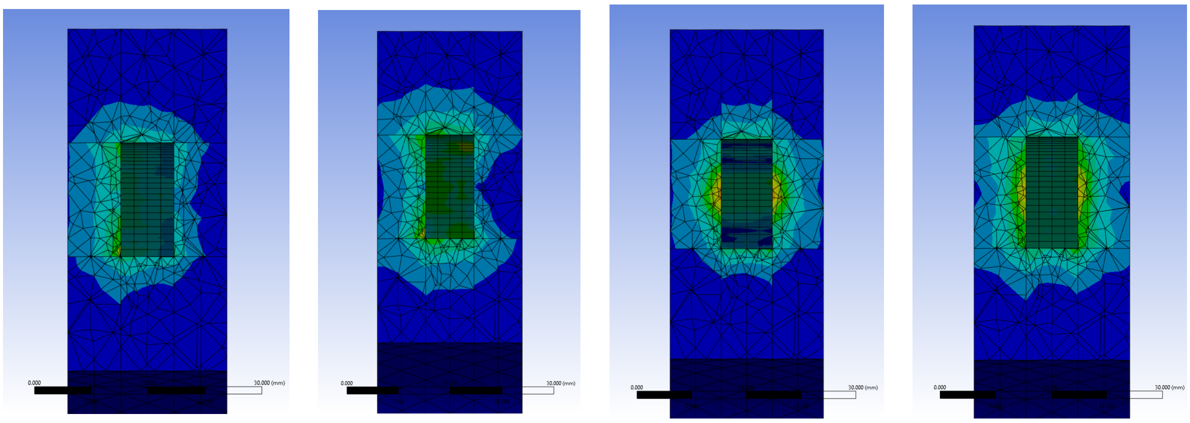

(a) Axial Halbach **(b)** Axial non-Halbach **(c)** Radial Focus **(d)** Monolithic Radial

Figure 3.23: Comparison between radial cross section total magnetic flux density of the 5-5-5-15 configurations.

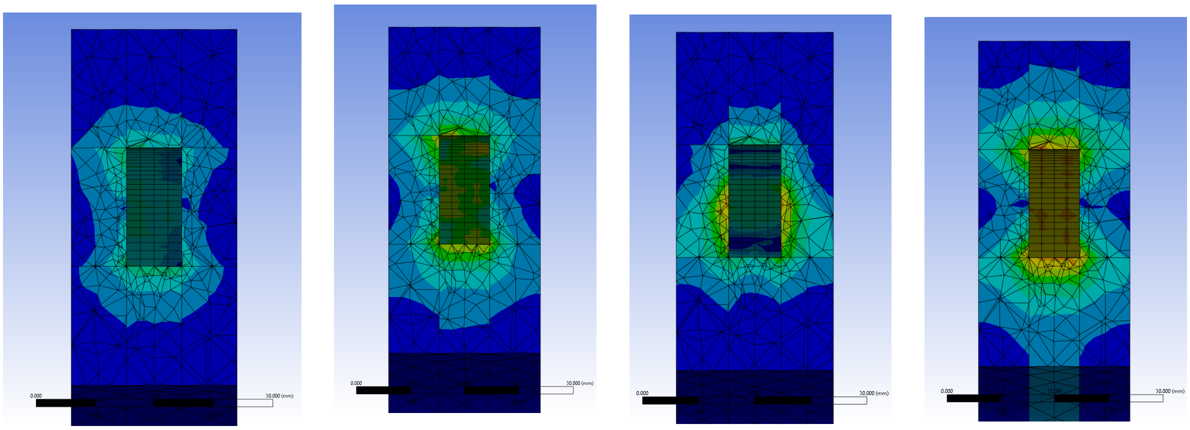

(a) Monolithic Axial Halbach **(b)** Monolithic Axial non-Halbach **(c)** Monolithic Radial Focus **(d)** Monolithic Axial

Figure 3.24: Comparison between radial cross section total magnetic flux density of the monolithic 5-5-5-15 configurations.

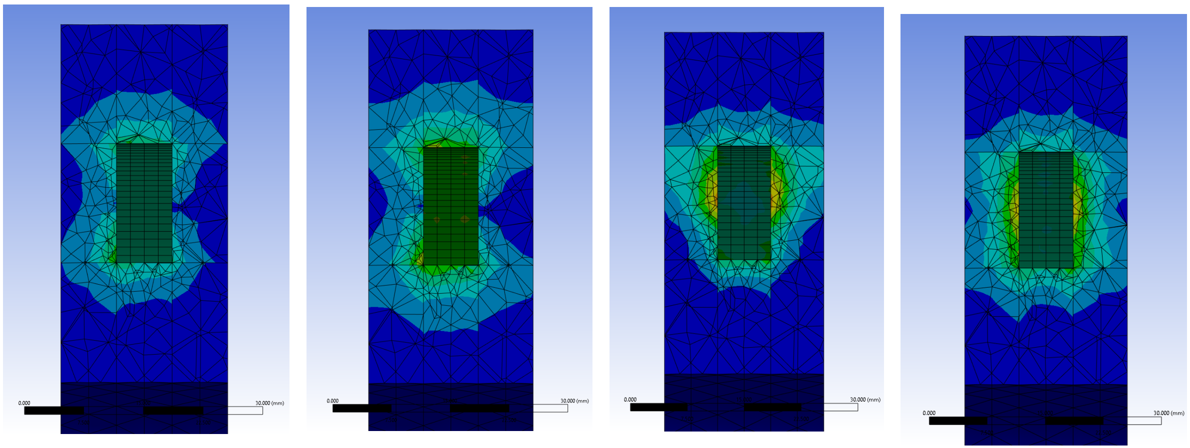

(a) Monolithic Axial Halbach Reversed

(b) Monolithic Axial non-Halbach Reversed

(c) Monolithic Radial Focus Reversed

(d) Monolithic Radial

Figure 3.25: Comparison between radial cross section total magnetic flux density of the monolithic reversed 5-5-5-15 configurations.

In conclusion to the configuration definition section of the chapter, the configuration which raises the most interest is the 5-5-5-15 Monolithic-Multipole Radial Focus design, as it provides the largest reduction in generated external magnetic fields. The axial Halbach configuration is next, followed by the axial non-Halbach and monolithic designs.

3.5.2. Simulation Data

This section of the chapter will focus on bringing a qualitative analysis to the observations made in the previous section. The first step towards this has been the partitioning of the enclosure into nine smaller volumes, which have been classified based on their placement within the initial enclosure, and can bee seen in Figures 3.26a, 3.26b and 3.26c. These partitions will be the basis of most graphs regarding the magnetic flux density simulation data found in this section.

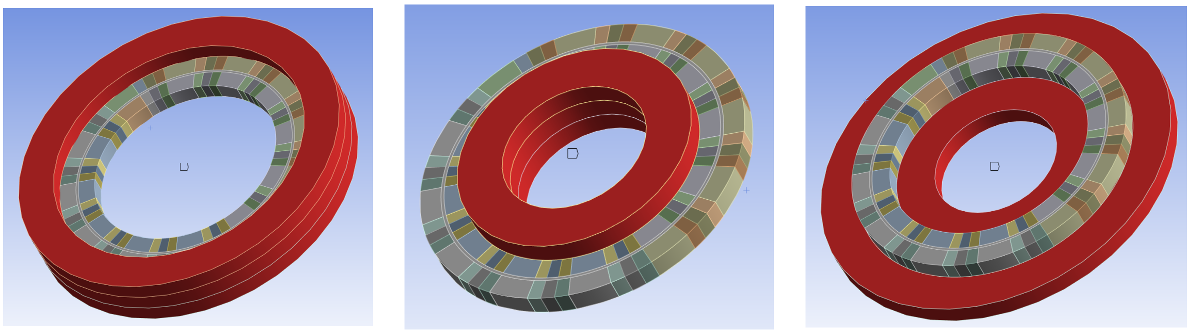

(a) R+ Enclosure Partition

(b) R- Enclosure Partition.

(c) Z- Enclosure Partition.

Figure 3.26: Enclosure Partitions

The first two Figures, 3.27 and 3.28, feature the stiffness measurements of the 5-5-5-15 multipole configurations, and 5-5-5-15 monolithic-multipole configurations respectively. In Figure 3.28 it can be seen how using only the ratio concept was not enough to stabilize the bearing in all its configurations. The axial Halbach and Radial focus configurations still display mode switching, although at a much smaller scale than previously encountered. The only configuration for which the ratio was enough to bring stiffness to a relatively constant and positive value was the axial non-Halbach configuration. Figure 3.27 also implements the monolithic-multipole concept, resulting in all configurations displaying constant positive stiffnesses across the rotation of the bearing. The highest stiffness was achieved by the Axial non-Halbach bearing, at 50 N/mm, followed by the Radial Focus configuration at 34.4 N/mm, and ending with the Axial Halbach configuration, at 25.6 N/mm. This order is due to the fact that the axial non-Halbach configuration is the least restricted one, with no elements in attraction to the monolithic bearing. All configurations still underperform in peak stiffness when compared to both monolithic bearings. This will always be the case, regardless of configuration type, as monolithic magnets employ their entire magnetic volume in the generation of stiffness performance, while monolithic-multipole architectures with the 5-5-5-15 ratio only employ half of the magnetic volume. However, the loss in stiffness performance is compensated through reductions in the external magnetic field and thus in magnetic pollution.

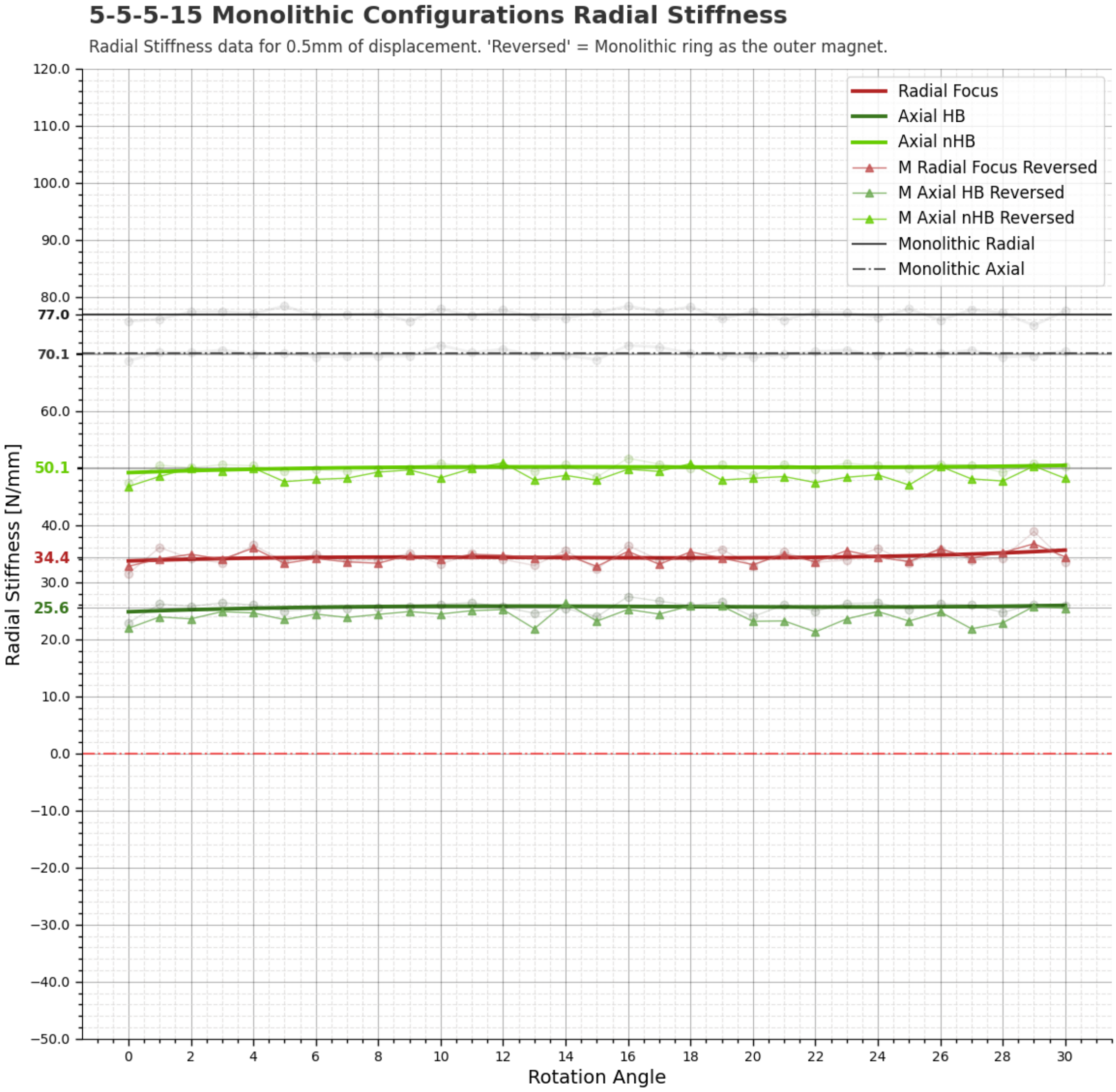

Figure 3.27: Stiffness data of 5-5-5-15 Monolithic Configurations.

The following set of figures focuses on the qualitative study of the enclosure partitions with respect to the external magnetic field generated, Figures 3.29a and 3.29b feature TMFD data along a path in the +R and -R enclosure partitions, where all magnetic configurations fall between the monolithic axial bearing (maximum) and monolithic radial bearing (minimum). Both axial configurations generate a stronger magnetic field in the radial direction than the radial focus configuration. Non-monolithic configurations are also featured in the first two sets of figures, which all fall below their monolithic counterparts in external field strength. This is expected as the monolithic integration reduces the effectiveness of the multipole configurations in terms of field print.

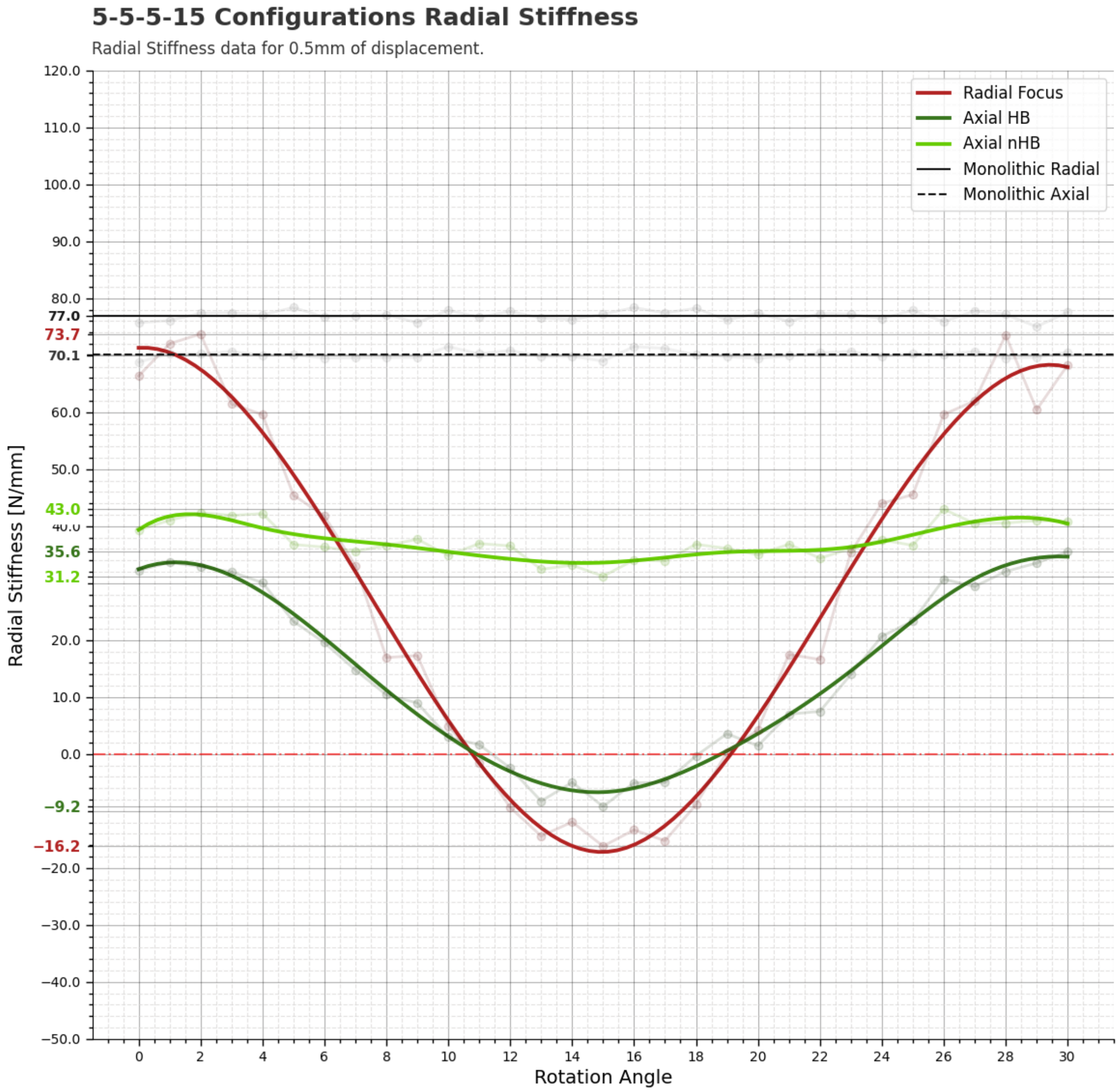

Figure 3.28: Stiffness data of 5-5-5-15 Configurations.

A similar phenomenon is seen in Figures 3.30a and 3.30b, where the axial enclosure partition paths are featured. However, a different order can be observed based on the distance from the bearing face. In the near field, the Radial configurations (both multipole and monolithic) generate the strongest fields, however when nearing the 3mm mark, the order reverses and is quite similar to the one present in the radial partitions. The radial configurations see a sharper drop in external magnetic field strength, which is a desirable behavior when considering magnetic pollution.

Figures 3.31a, 3.31b, 3.32a and 3.32b all feature average total magnetic flux density data averaged over the entire volume of the partitions considered, as opposed to just a centrally located path as was the case with the previous two sets of figures. In the radial partitions, the order encountered so far is maintained, with the axial configurations generating stronger fields than the radial one. An observable difference between the two radial partitions is that all monolithic configuration feature a considerable increase in generated field strength on the -R partition volume. This is due to the fact that the monolithic bearing is the one defining that volume of the enclosure, resulting in it imposing its field print. In the axial partitions, the order varies a bit, with the axial Halbach monolithic configuration featuring the highest average total magnetic flux density, followed by the radial focus monolithic and axial non-Halbach configurations for the Z+ enclosure partition. The Z- enclosure partition features the radial monolithic configuration as generating the strongest magnetic field, followed closely by the two axial configurations. Throughout all enclosure average data, the non-monolithic configurations, although generating weaker magnetic fields, display variations in the resulting values, which would have caused unreliable bearing performance.

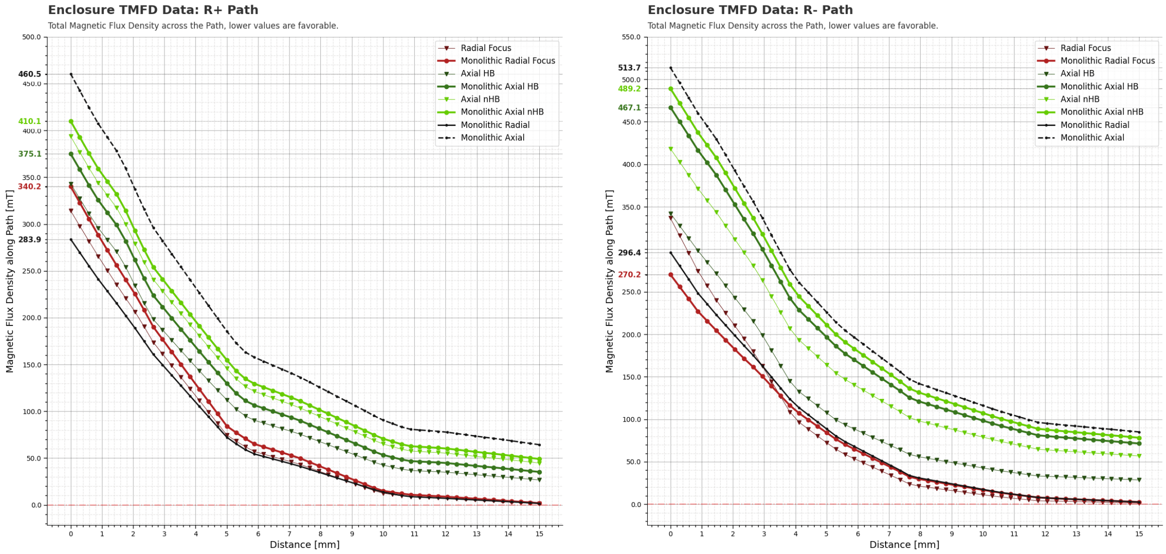

(a) Path along R+ enclosure.

(b) Path along R- enclosure.

Figure 3.29: TMDF data on a path along the width of the two radial enclosure partitions.

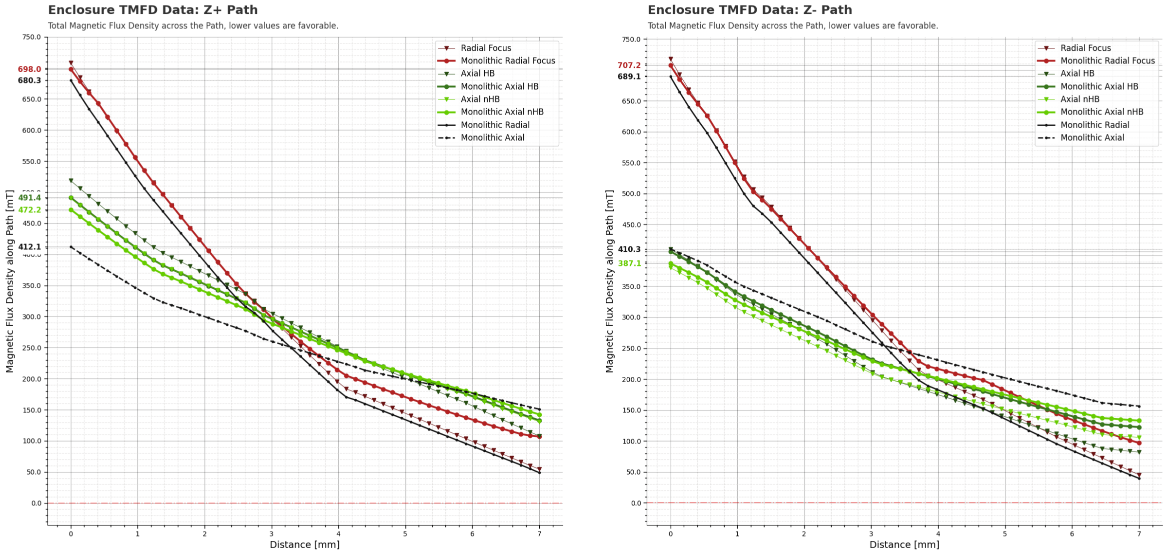

(a) Path along Z+ enclosure.

(b) Path along Z- enclosure.

Figure 3.30: TMDF data on a path along the width of the two axial enclosure partitions.

Figure 3.33 features an overview of the axial enclosure partitions in the case of the Radial Focus 5-5-5-15 Monolithic Configuration. This figure adds two more measurements to each face, namely two additional paths on the top and bottom side of the +/- Z face, in order to more accurately measure the influence of the monolithic component of the bearing. It can be observed how the bottom ("BOT")

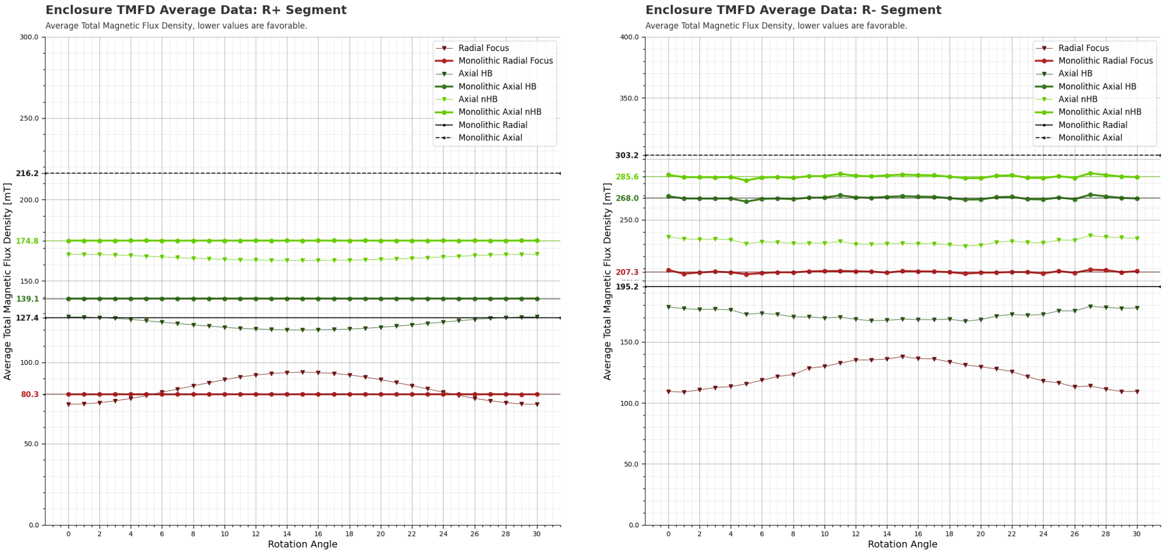

(a) R+ enclosure.

(b) R- enclosure.

Figure 3.31: TMDF data on the two radial enclosure partitions.

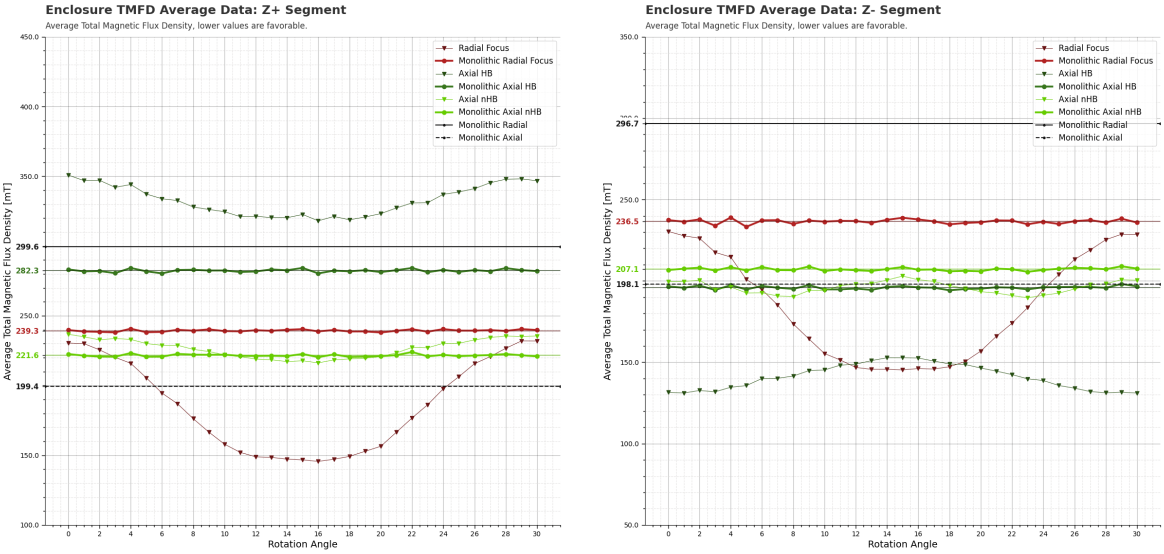

(a) Z+ enclosure.

(b) Z- enclosure.

Figure 3.32: TMDF data on the two axial enclosure partitions.

path falls below all other paths in the simulated magnetic field strength, which is in accordance with the observations on its axial cross section. Following this, the top ("TOP") path starts below the air-gap centric path that has been considered thus far. However, as we move away from the bearing face, and thus from the focused magnetic field around the air-gap, the "TOP" path takes the lead in magnetic field strength. Another aspect that is highlighted in this figure is the symmetry of the +Z and -Z generated fields, as the lines representing the +/- Z paths are very close in field strength regardless of distance from the bearing face.

As a conclusion to the Simulation Data section, the Radial Focus 5-5-5-15 Multipole Configuration has proved to be the one raising the most interest, by offering both a good stiffness performance (besting the axial-Halbach configuration), while also featuring a considerably smaller magnetic pollution volume.

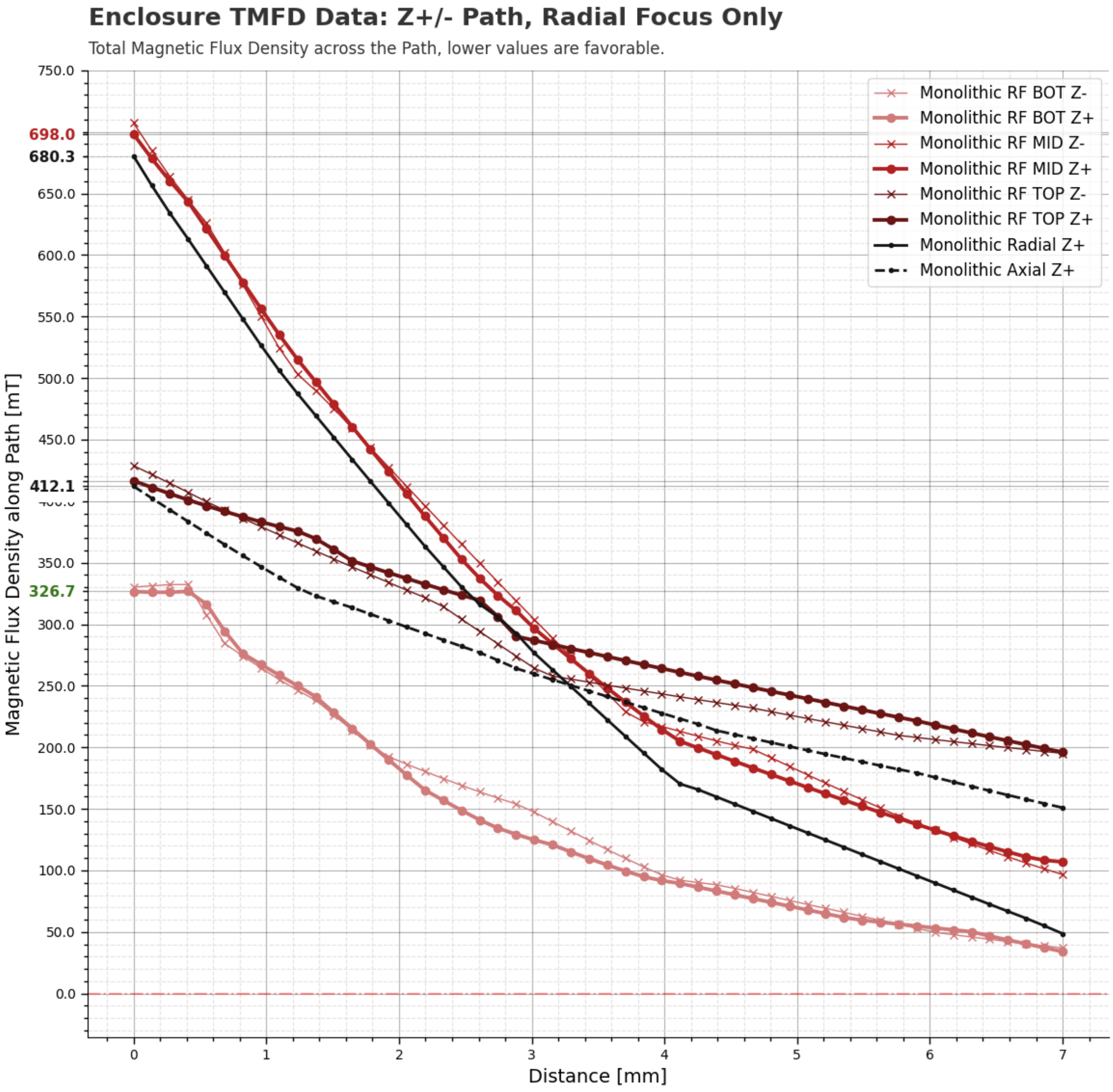

Figure 3.33: Radial Focus 5-5-5-15 Monolithic External Field Path Data.

The combination of both these properties makes this configuration the best out of the ones considered, and the final iteration of the segmented multipole bearing. This configuration will be the one adapted and simplified for the experimental phase of the thesis, which will be presented in more detail in Chapter 4.

3.5.3. Steel Implementation

This section of the thesis focuses on the concept of implementing steel elements into the structure of the 5-5-5-15 Monolithic bearing. The magnetic segments which were replaced by steel elements in the simulations were the tangential ones, as their magnetic configuration (tangential magnetization) is the hardest one to manufacture and would post the most problems in the experimental phase of the project. However, as Figure 3.34 shows, the steel elements allow for the formation of magnetic shorts within the multipole array, in both configurations tested. This in turn leads to complete loss of radial stiffness, making the steel inserts detrimental to bearing performance. In an attempt to counteract this behavior, both laminated steel elements and shortened steel elements (only the outer portion of the magnetic array featured steel elements, thus cutting their radial length in half) were considered. These adaptations prevented the formation of magnetic shorts, however the resulting radial stiffness was considerably lower than the no steel inserts configuration (around 5 N/mm).

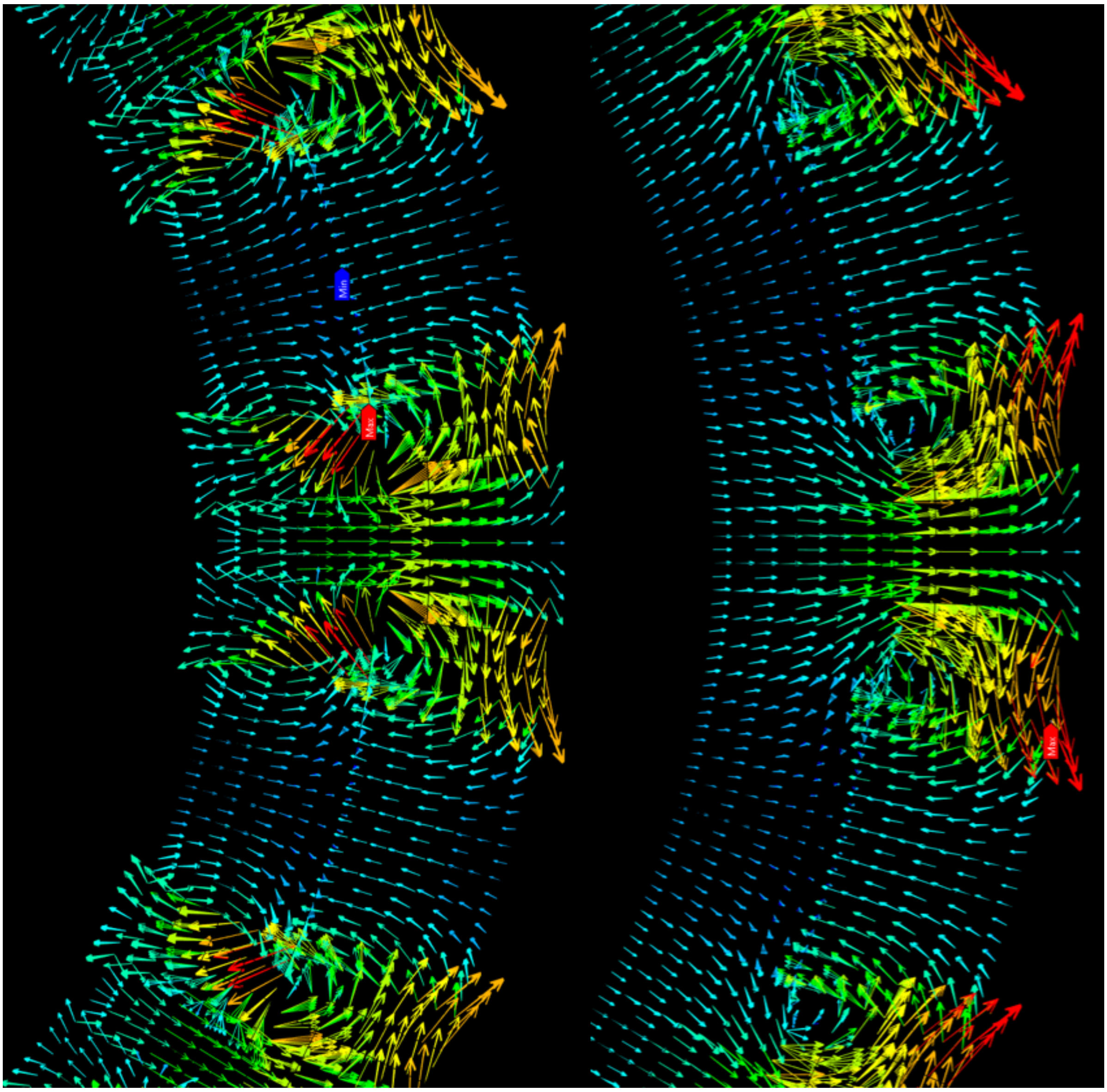

Figure 3.34: Total Magnetic Flux Density, Vector Representation, of the configuration resulted from replacing the tangential magnetic elements with steel. Right - steel elements on both arrays, Left - steel elements only on the multipole array.

Another integration of steel within the 5-5-5-15 Monolithic configuration was through the implementation of a steel plate on the +Z face of the bearing, which can be seen in Figure 3.35. The result of this integration is featured in Figures 3.36a and 3.36b. The steel plate is proved to lower the generated external magnetic fields in the axial direction for the axial bearing, while increasing its radially generated field. In the case of the radial bearing however, the plate increased both radial and axial total magnetic flux density in the far field, which leads to increased magnetic pollution.

As a result of these simulations, the steel integrations do not provide enough incentives to be integrated into the experimental design of the bearing, and as such will not be considered viable solutions for design simplification or performance enhancement.

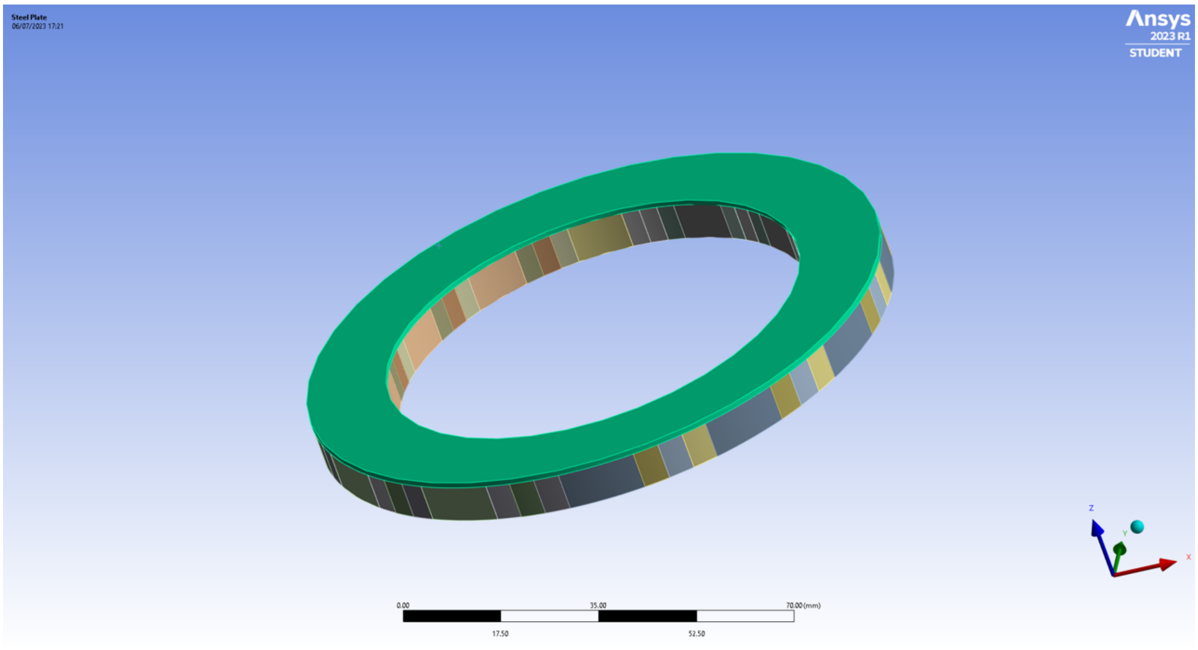

Figure 3.35: CAD model of the steel plate considered.

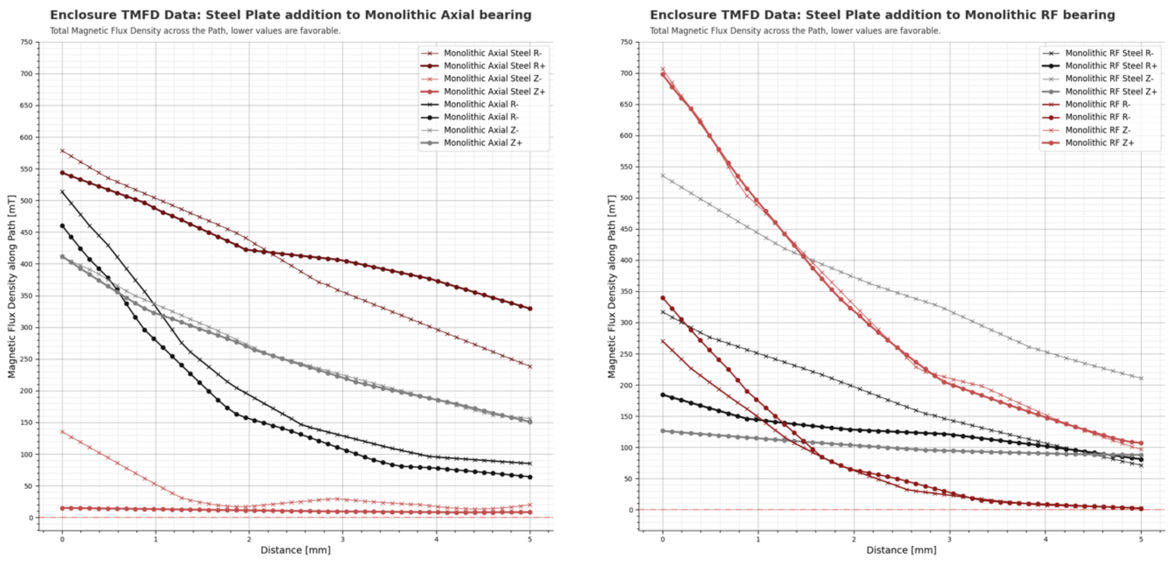

(a) R enclosure partition.

(b) Z enclosure partition.

Figure 3.36: TMDF data on a path along the width of the respective enclosure partitions when implementing a steel plate on the Z+ axis.

3.6. Configurations Overview

Throughout the numerical phase of the thesis, four different types of multipole bearing architectures were simulated and discussed. These are:

1. Segmented Bearings
2. Non-symmetrical Bearings
3. Monolithic-Multipole Bearings
4. Monolithic-Multipole Ratio Bearings

Each configuration built on the conclusions drawn from the previous design, trying to improve its performance in order for all imposed requirements to be satisfied. The initial configuration featured a simple, radially symmetrical, segmented design, which suffered from large variations in performance across bearing rotation, switching between attraction and repulsion modes at fixed intervals.

To counteract this, the non-symmetrical bearing configuration was introduced. The main idea behind this was to avoid the perfect overlapping of opposite magnetization magnets by changing the number of segments per array. In this manner, the effect of attraction inducing segments would be lowered. Bearing performance throughout rotation was successfully stabilized as a result, but introduced a new issue: non-zero Cartesian forces. As the two arrays were no longer symmetrical, destabilizing forces in the radial plane that were nullified in the initial segmented configuration could no longer be cancelled out. For this reason, the non-symmetrical configuration is not suitable for bearing implementations.

Based on the previous architecture and its shortcomings, it was concluded that a multipole magnetic bearing would have to be symmetrical in order for destabilizing forces to cancel out. As such, a new method of stabilizing performance across rotation needed to be found. The combination of a monolithic magnet and a multipole array was conceptualized, as the monolithic magnet would provide a constant magnetic field on which the multipole magnet would act, thus eliminating the problem of overlapping segments. This bearing architecture succeeded in its primary goal, with stiffness and force values flattening out. However, the performance compared to a conventional monolithic bearing was poor, only a small portion of the multipole array's volume contributing to performance. In order to increase array involvement, a new ratio was introduced between the ”working” segments (which were in repulsion with the monolithic one) and ”pattern completion” segments.

This lead to the Monolithic-Multipole 5-5-5-15 Ratio Bearing design being chosen as the final configuration, presenting constant stiffness and force throughout rotation as well as higher parameter values compared to the no-ratio design.

4

Experimental Setup and Measurements

4.1. Experimental Setup

This section of the thesis will focus on the adaptation of the chosen multipole configuration to the experimental setup. First, the change from arc-segments to rectangular ones is presented, together with updated simulation data. Following this, the design and manufacturing of the bearing structure is discussed. The section concludes with the comparison between experimental and simulation data, addressing error sources and interpreting their effects.

4.1.1. Bearing Design Simplification

In order for the 5-5-5-15 Radial Focus Monolithic-Multipole design to be translated to a prototype, certain simplifications to the bearing architecture had to be made. The reasoning behind this was the very complex magnetic orientation of the varying arc segments, which were very difficult to find as off-the-shelf components. Custom designed magnetic elements were considered for both the multipole array and the monolithic configurations, however the cost of such components would have far exceeded the project's budget and time frame. As a result, the arc segments have been simplified to cubic and rectangular magnets. This new simplified design can be observed in Figures 4.1 and 4.2. The two differ through the placement of the multipole array on the stator or the rotor of the bearing. In order to choose a final design, simulations were ran, focusing on the generated magnetic field and radial stiffness.

The resulting data showed that the simplification of the monolithic bearing would only be representative of the arc-segment design (considering the same scale for the bearing) if it would be placed on the stator (outer segment of the bearing), as the gaps between magnetic elements facing the air-gap would be too large, causing considerable performance losses.

Another simplification that was made was the change of the magnetic array cross section, from 7mm to 10mm, as to accommodate for commercially available magnets, which do not typically come in odd sizes. As a result of this design choice, the final bearing configuration was able to be sourced from off-the-shelf magnetic components. A total of 31 cubic 10x10x10mm magnetic elements would be featured on the monolithic array, while 12 cubic 10x10x10mm (15 degree radial segments), 24 rectangular 10x10x3mm (5 degree tangential segments) and 60 10x3x2mm rectangular magnetic elements would be employed in the assembly of the multipole array. The 60 10x3x2mm magnetic elements would be assembled into 10x3x10mm formations (5 degree radial segments). This has been done in order to allow for the axial magnetization to be formed.

The final design of the experimental bearing had a simulated result of the radial stiffness of 40.1 N/mm, which is above the generated stiffness of the original configuration (34.4 N/mm). Although the simplified design features gaps between magnetic elements, the increase in cross section side length from 7 to

10 mm also increased the total magnetic material volume, which resulted in an overall increase in performance.

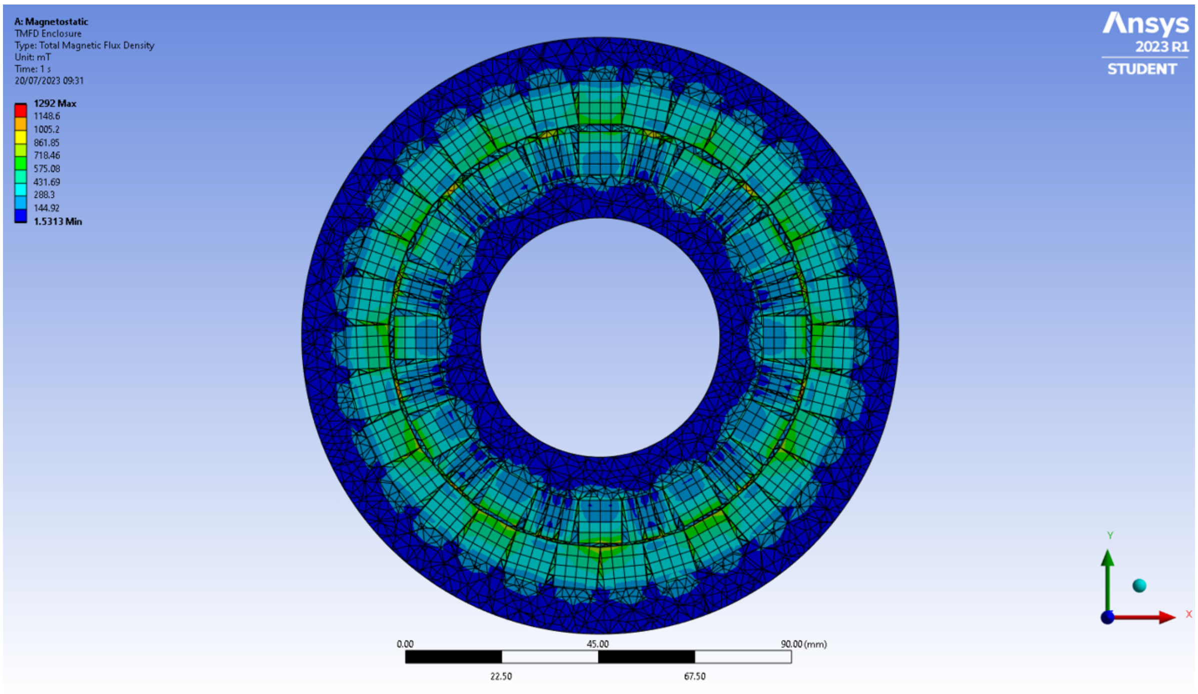

Figure 4.1: Simplification of the 5-5-5-15 Multipole Radial Focus Configuration.

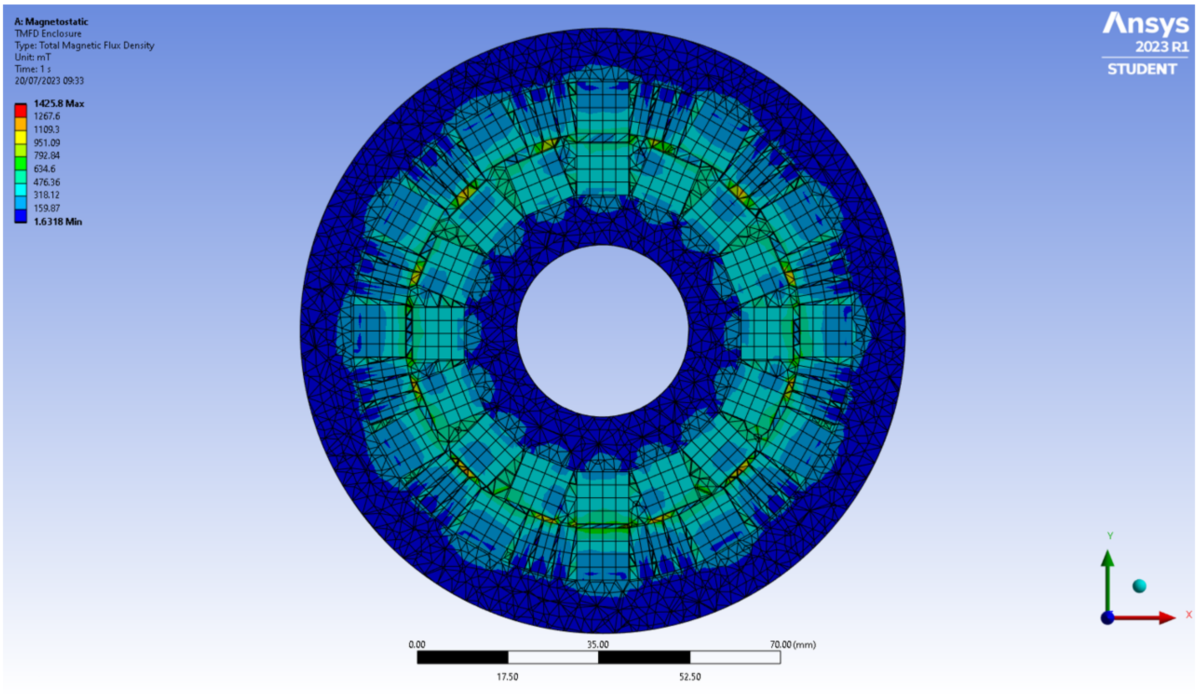

Figure 4.2: Simplification of the 5-5-5-15 Multipole Radial Focus Configuration, Reversed

As the designed bearing is radially stable, Earnshaw's Theorem states that the bearing will be axially unstable. As a result, an additional mechanism is required to stabilize the bearing in the axial direction. For this purpose a thrust bearing with a static load rating of 63 kN was chosen which it poses no risk of failure as the peak load generated by the bearing is around 110N.

4.1.2. Prototype Structure, Manufacturing and Assembly

The structure for the prototype was entirely 3D printed out of PLA. This manufacturing method has been chosen as a cost-friendly alternative to CNC Machining, while also avoiding the long lead times associated with metal manufacturing. Another benefit of 3D printing the structure was the possibility of rapid iterations in the design process, which is an important benefit to the prototyping process.

The main structure of the bearing was formed by the two supports of the magnetic arrays, onto which the magnetic elements would be assembled. The stator support was the highest volume component, which would be directly connected to the Aluminium base plate, which can be observed in Figure 4.4. The support would feature 31 slots for the 10x10x10mm cubic magnets, separated by guiding fins. The support also features four guiding slots for the aluminium rods used in the assembly of the stator and the rotor in the later stages of the experimental phase, as well as four M6 fastening holes, through which the structure would be secured to the Aluminium base plate. All these features can be seen in Figure 4.9a and 4.12. The magnetic array will also be secured with the help of a cap, fastened to the stator support through 10 M3 screws. All M3 screws were supported by metal inserts, which can be seen in 4.3. The rotor support structure followed a similar finned magnetic array assembly, with slots for all 48 magnetic elements and assembled elements, which can be seen in Figure 4.8. The structure also featured a center hole through which it could be secured during the assembly of the bearing to the thrust bearing support. The core of the rotor support featured an additional slot into which the radial stiffness measuring tool would be attached, which can be observed in Figure 4.8, and a radial displacement slit on the diametrically opposite side. Similarly to the stator support structure, the magnets are also secured with a cap, fastened to the rotor support through 6 M3 screws.

The secondary structure of the bearing's stator was formed by the thrust bearing mount, which housed the axially stabilizing thrust bearing. This structure can be seen in Figure 4.4 This is the structure onto which the bearing rotor would sit under operation and would be fastened to during bearing assembly. This structure featured four M6 mounting holes, through which it would be secured to the Aluminium base plate. It also featured two M6 mounting holes for the stator, as well as an M6 mounting hole on the bottom surface for the scale mount.

Four annex components were also employed in the testing and assembly of the bearing. The first such component is the being the radial stiffness tool, which interfaces the rotor of the bearing and the tension force gauge. On the rotor side, it would be fastened by an M3 screw, while the gauge attachment would be done through an M6 threaded hole. The second measurement component was the scale mount, which attaches to the bottom of the thrust bearing mount through a threaded rod which passes through the Aluminium base plate. The scale mount then features a 10cm base, which would rest on the scale under testing conditions. In this manner, both the rotor and thrust bearing mount would only be supported through the scale mount, thus allowing for the measurement of the axial force being generated by the bearing. This component can be seen in Figure 4.16. The third measurement component was a spoked wheel design, which connected to the cap fastening holes of the rotor support through 6 M3 screws. This wheel featured an additional M3 screw in the center of the component, through which a torque screwdriver could be used in the determination of cogging torque (all within the range of 0.25-0.33 Nm). This component can be observed in Figure 4.13. The final annex component was the stator puck which secured the stator to the thrust bearing mount through two M6 mounting holes.

The completed assembly can be observed in Figures 4.10, 4.9a and 4.9b. All main structural components mentioned above are presented in more detail in the technical drawings found in Annex A.

The assembly of the magnetic components started with their marking, sanding and cleaning. The marking of the magnets was conducted with the aid of a magnetic sensor, through which the north and south faces of the magnets could be identified. However, due to a malfunction of the sensor, these two faces have been inverted on all magnets, leading to a reversed configuration on a individual magnet level. This will be further detailed in the measurement section of this chapter. All magnetic elements were lightly sanded on the surfaces which would come into contact with the adhesive (cyanoacrylate/super glue) in order to guarantee good bonding between the two. The magnets would then be cleaned with a 50/50 mixture of water and IPA. This process is features in figures 4.6a, 4.6b and 4.6c. The magnets would then be inserted into their respective slots and held in place for a couple of seconds, until the adhesive hardened. This process can be observed in Figures 4.7a, and 4.7b.

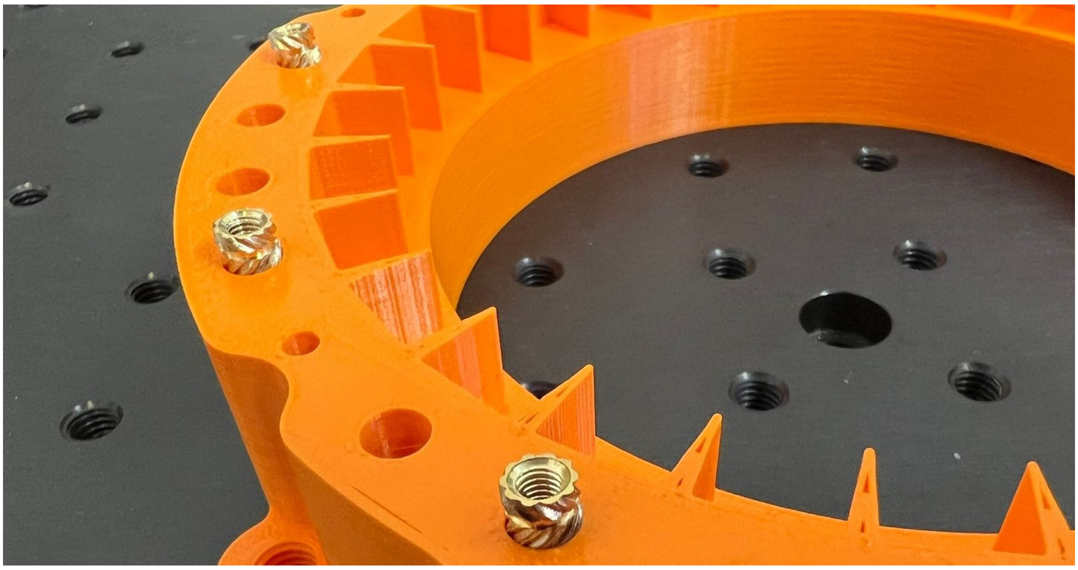

Figure 4.3: Stator Threaded Inserts - Prior to being inserted through the use of the soldering iron.

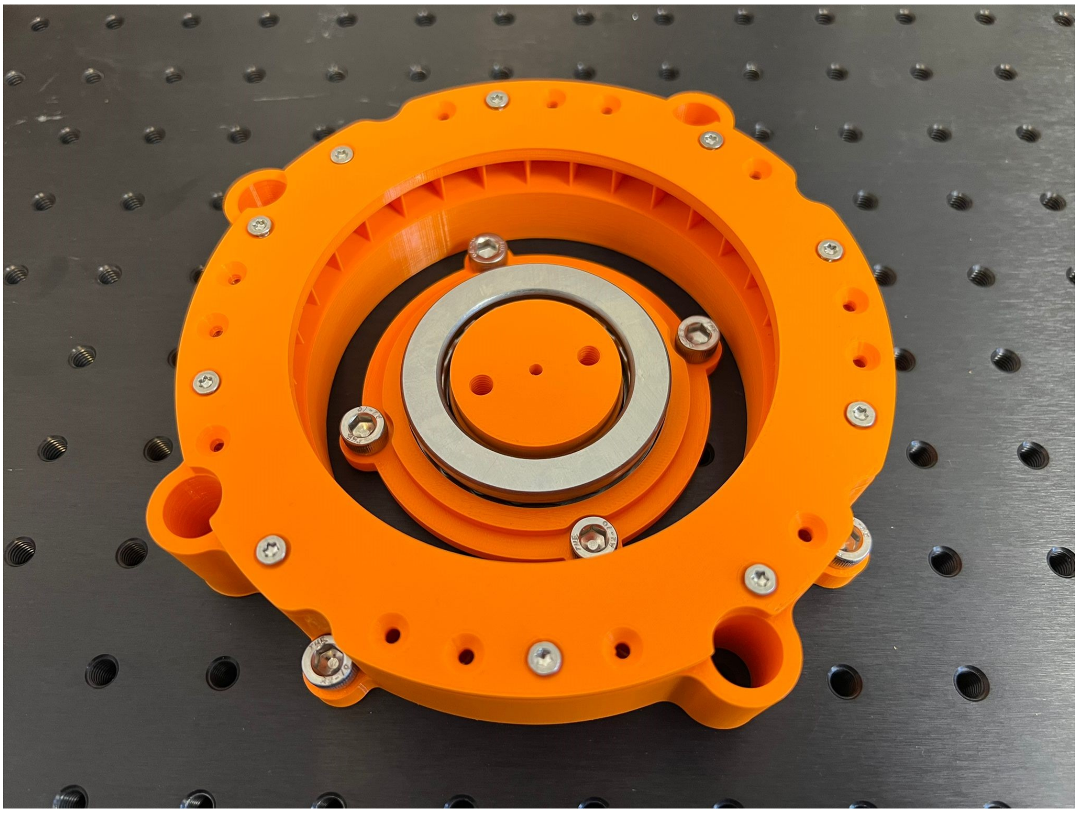

Figure 4.4: Assembled Bearing Stator: Stator structure with fastened cap on the outside, Thrust Bearing and its Mount in the center. Fastening points for the Rotor can also be seen on the upper surface of the Thrust Bearing Mount.

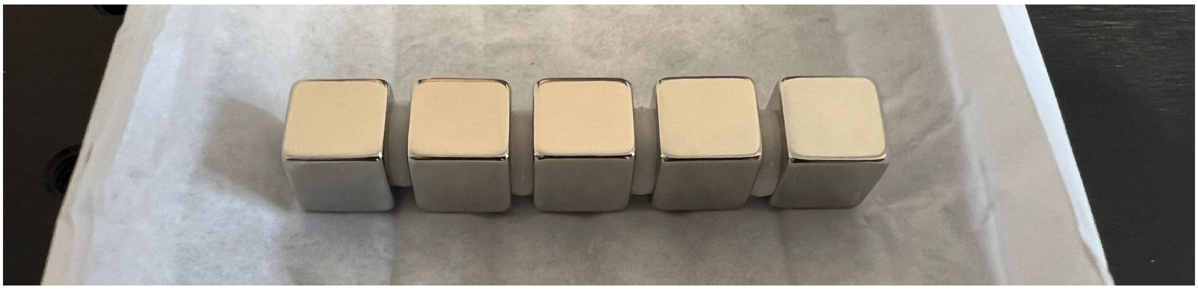

Figure 4.5: Magnet packaging.

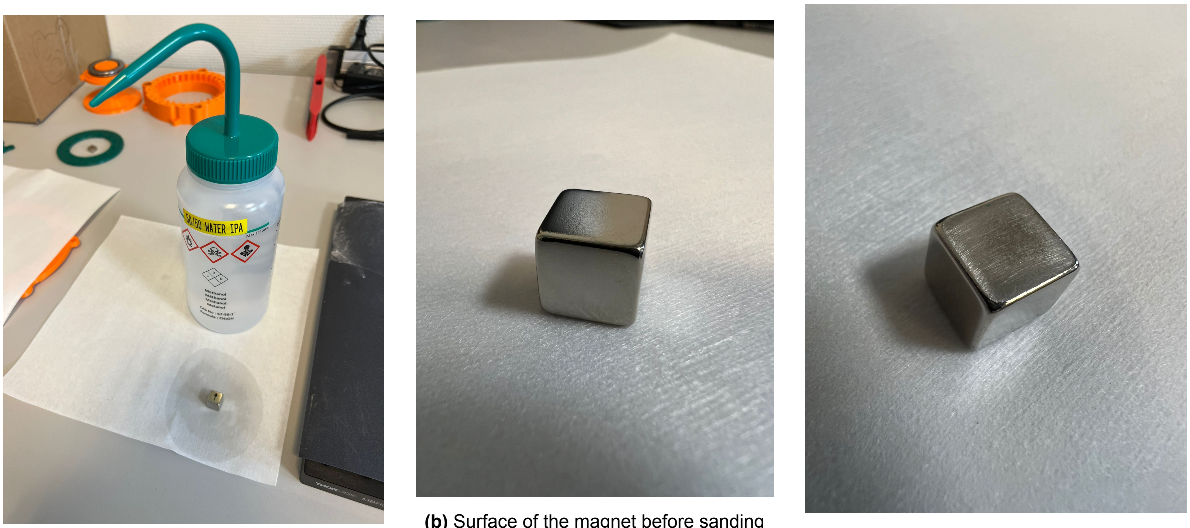

(a) Cleaning and sanding process.

(b) Surface of the magnet before sanding and cleaning.

(c) Surface of the magnet after sanding and cleaning.

Figure 4.6: Magnet pre-assembly processing

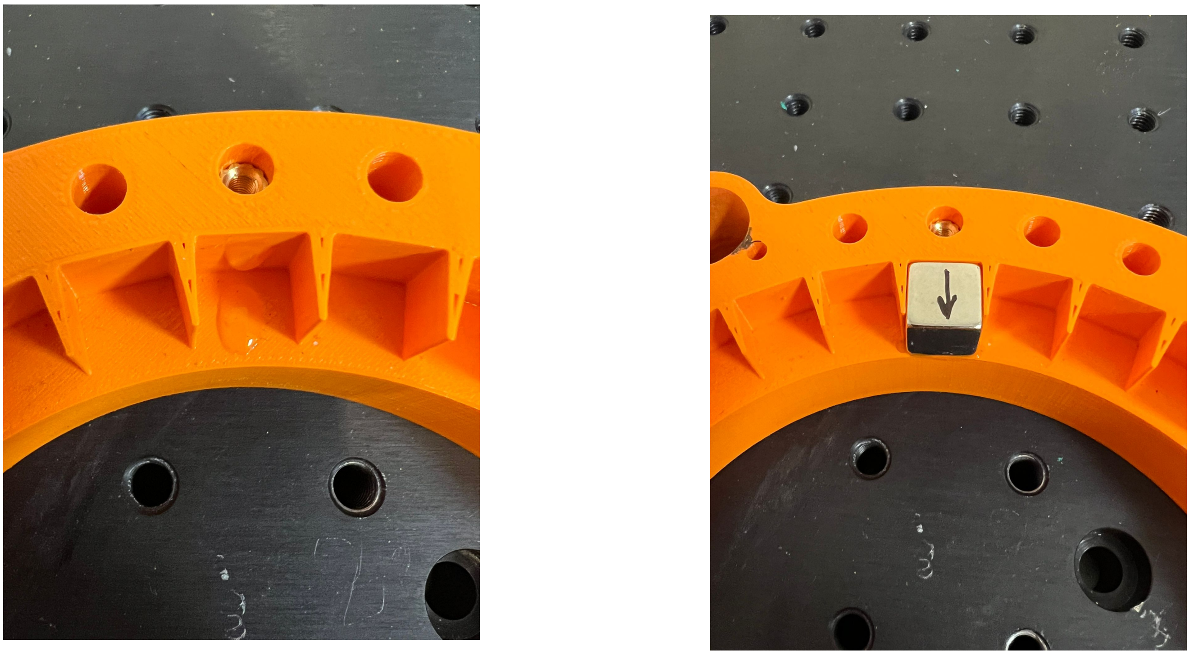

(a) Adhesive used in the assembly of individual magnets on the stator.

(b) Assembled magnet with reversed orientation marking.

Figure 4.7: Stator assembly process.

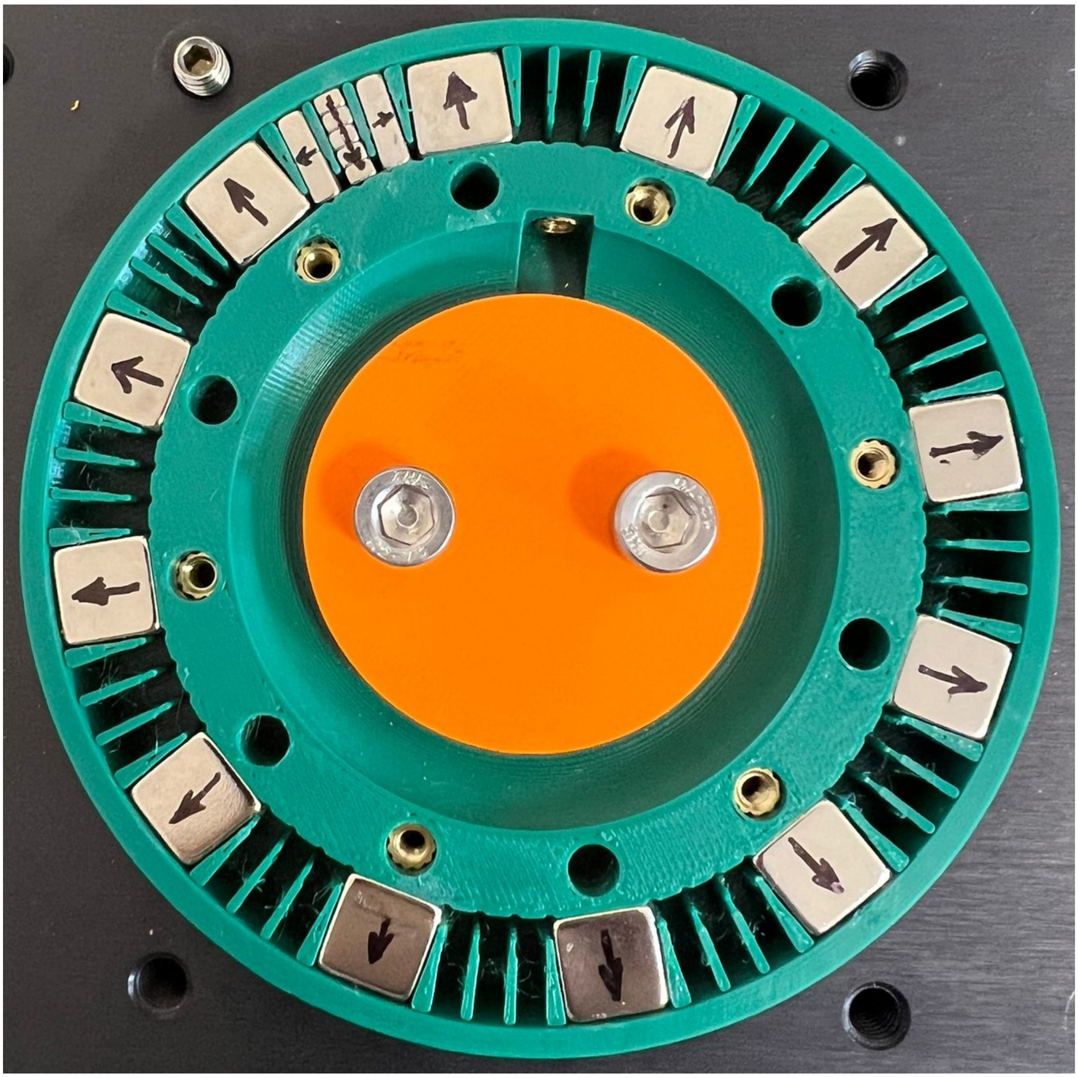

Figure 4.8: Rotor assembly process: Magnets are first marked with their orientation, then inserted into their respective slots. Figure orientation is reversed (arrow points at the south face).

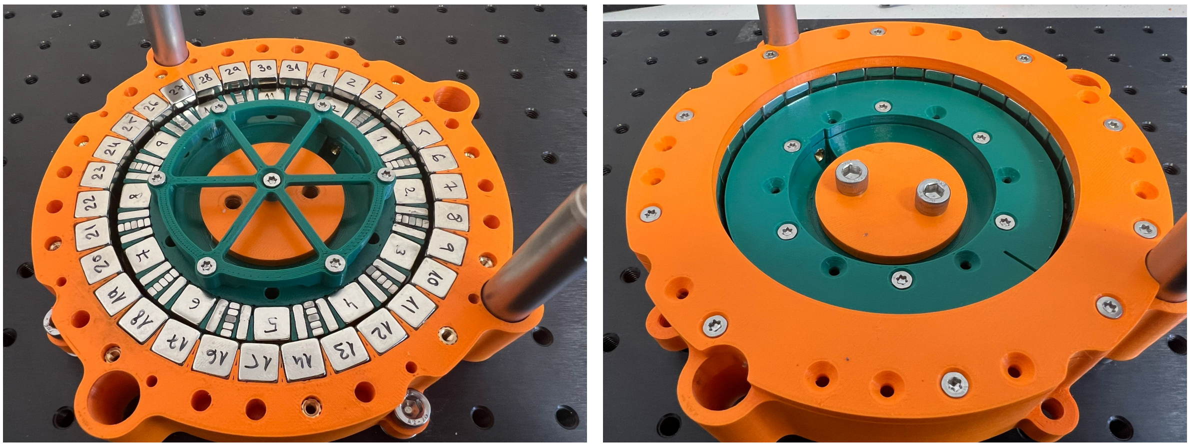

(a) Assembled bearing without caps - numbered magnets.

(b) Assembled bearing with caps, secured rotor.

Figure 4.9: Assembled Bearing

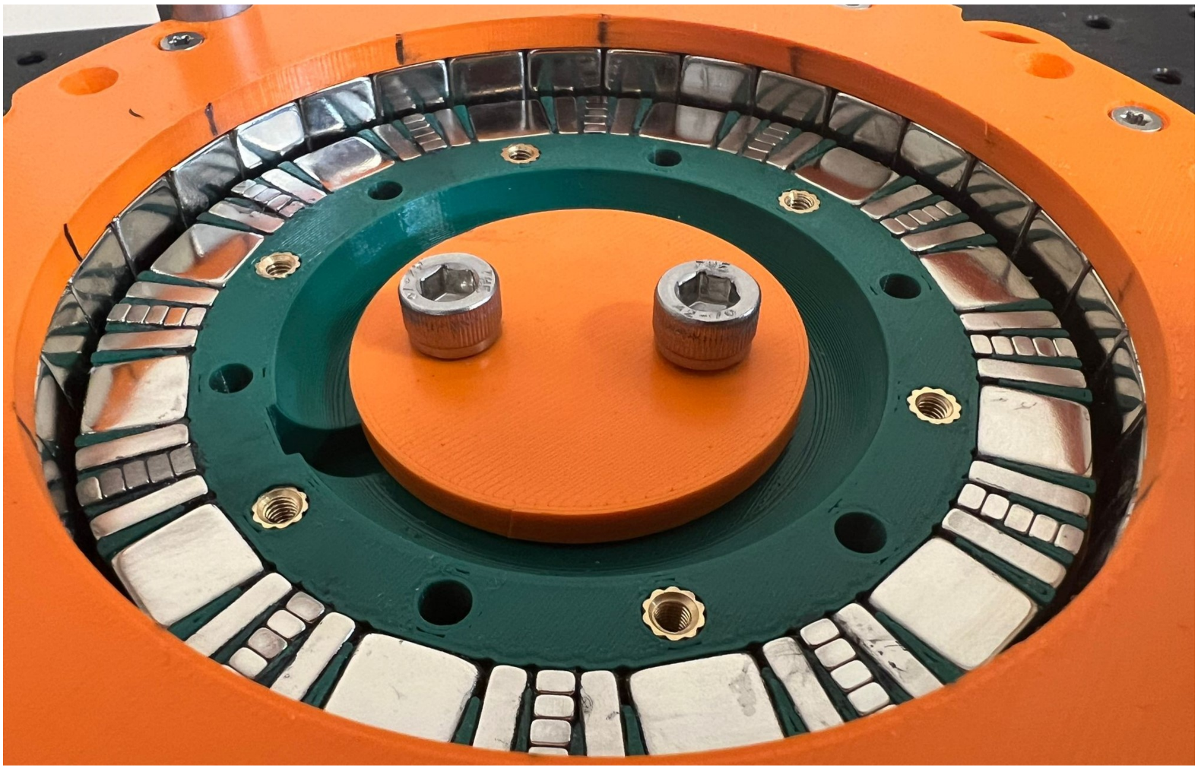

Figure 4.10: Assembled bearing - magnet close-up. The rotor is secured to the Thrust Bearing Mount through the Rotor Puck (central orange component), fastened with two M6 screws.

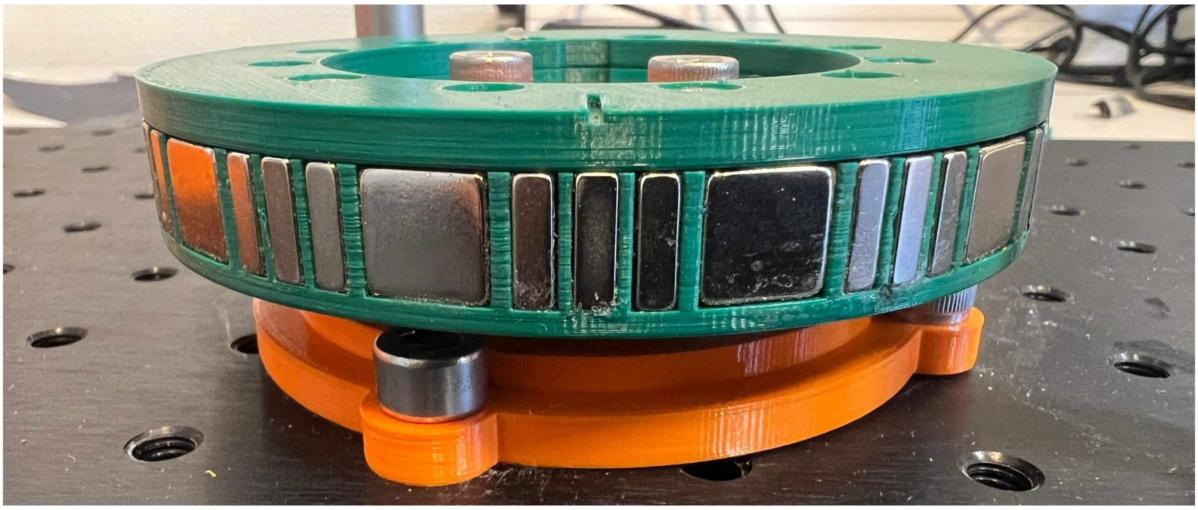

Figure 4.11: Assembled rotor side view, secured to the Thrust Bearing Mount. The Rotor Cap Slit can also be seen on the top surface. It would have been used in the measurement of the Radial Stiffness, for the radial displacement between rotor and stator, as an anchor point for the Caliper.

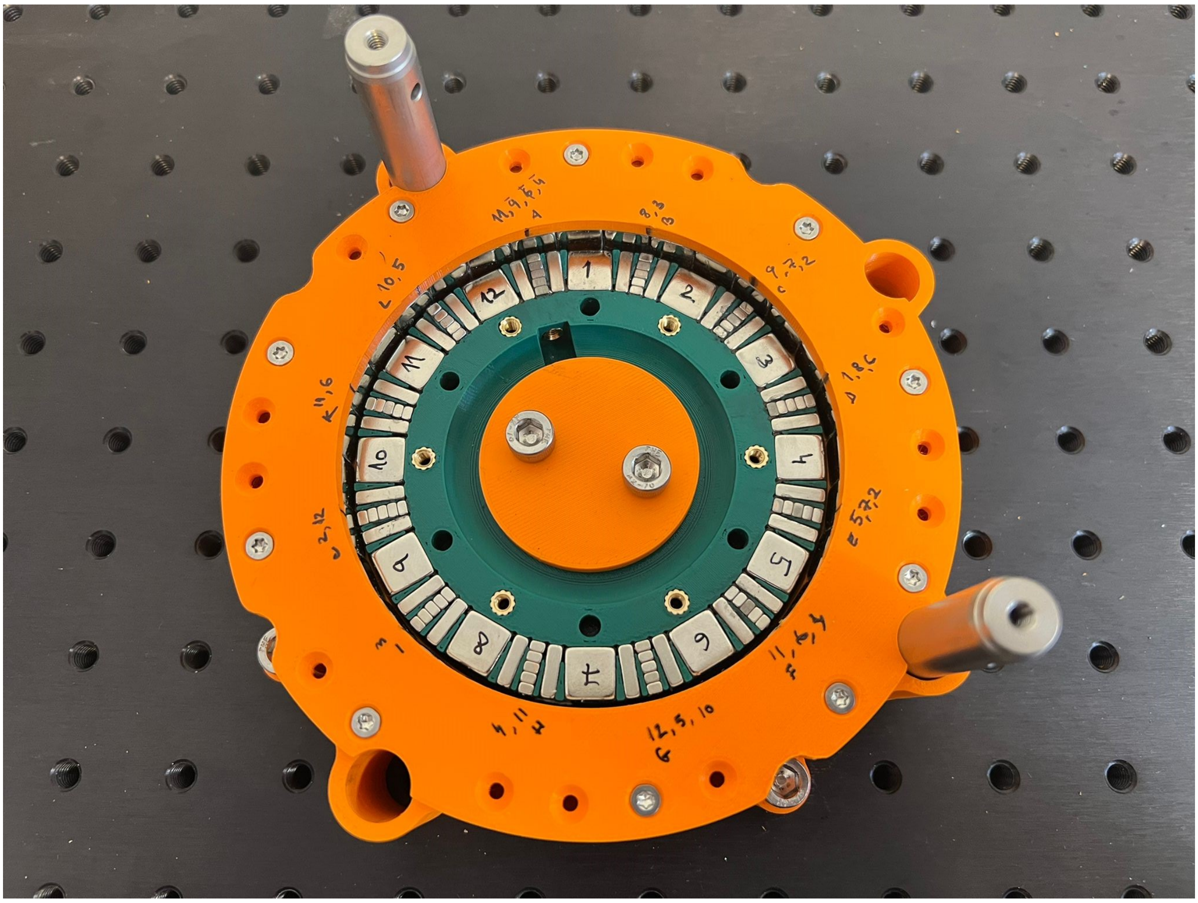

Figure 4.12: Bearing cogging - Stable positions of the rotor are marked on the stator cap (A-L), with the magnets that overlap being highlighted.

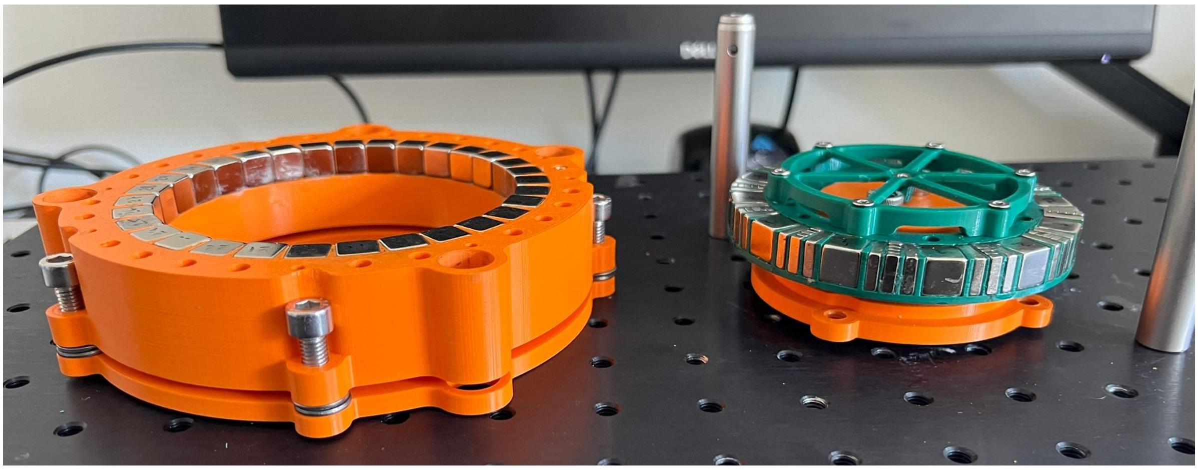

Figure 4.13: Stator and rotor of the bearing - The stator has been lifted from the base aluminium plate with the aid of an additional 3D printed component, with the same footprint as the stator structure. Additional axial displacement was imposed using two washers as spacers between the main stator structure and the additional base component, at each of the fastening points.

Manufacturing Failure of the Rotor Structure during Assembly.

In all figures shown so far, the bearing rotor is the second one to have been built. An initial attempt at assembling the rotor structure resulted in the failure of the guiding fins - failure mode which could not be repaired, thus requiring a new structure to be printed. The failure occured during the slotting process of the magnetic elements.

The initial assembly process included a PLA ring which fit tightly around the outer surface of the magnets, with the purpose of easing the assembly workflow and allow for strictly vertical insertion of the segments. However, this assembly method proved to be destructive. With the ring mounted, one could no longer inspect the slotted magnets from a side view, leaving the top down view of the structure as the only mid-assembly inspection point. This lead to the magnets appearing to be slotted correctly, even when that was not the case. Due to the vertical insertion of the magnets, all magnetic interaction forces which were not exerted in the axial direction were supported by the guiding fins and the rotor structure. These forces proved to be too strong for the guiding fins, resulting in their failure at the interfacing plane between the fin and the main rotor structure.

The magnetic interactions imposed a torque on the to-be-slotted elements, which then overloaded the low stiffness guiding fins. To overcome this issue, the additional ring was dropped to allow for full inspection of the magnetic elements, as well as changing the approach angle of the segments from a fully vertical one (90 degrees) to a 45 degree one. In this manner, the imposed torque could be better managed during the assembly process.

Experimental Bearing Diagram.

Figure 4.14 shows a diagram of the complete bearing assembly, in its axial force measurement configuration. It can be seen how the Scale Mount passes through the aluminium Base Plate and attaches to the Thrust Bearing mount. A gap of 5 mm is thus created between the thrust bearing mount and the base plate, which serves as a safety margin. To account for this on the stator side, the Stator Spacer lifts the Stator Support by 5 mm. In this manner, the rotor is supported only by the scale, and as such measurement can be taken. The figure also shows the Force Gauge Mount, which attaches to a slot within the rotor support and would have been used for the measurement of the radial stiffness.

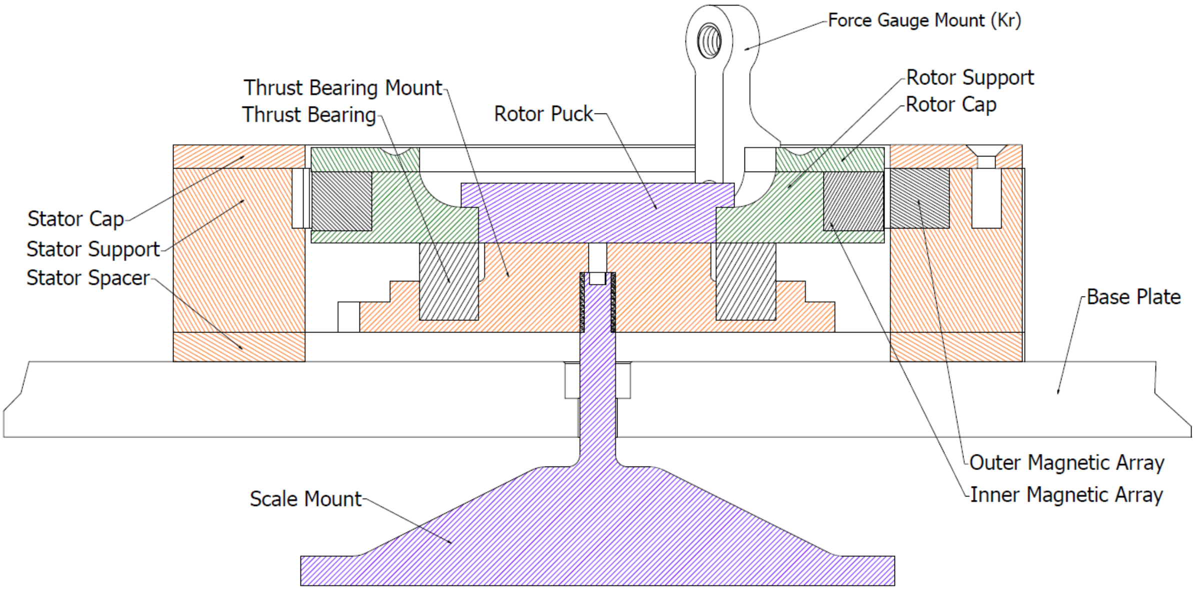

Figure 4.14: Bearing Cross-Section Diagram.

Manufacturing Tolerances and Errors

This section of the chapter focuses on the measurement of 3D printed components and extracting the resulting manufacturing errors. Components with come into contact with the stator or rotor components have been considered for these measurements. For each data point, eight to twelve measurements have been made, whose average was then considered final measured value and was taken into consideration for tolerance calculations. Table 4.1 features measurements of the inner magnet mount, which represents the rotor of the bearing, where the largest absolute error was 0.25mm (outer diameter), while the largest percentage error was 1.4% (core diameter). Table 4.2 features measurements of the outer magnet mount, or the stator of the bearing. In this case, the largest absolute error was 0.20mm (core diameter), while the largest percentage error was 0.27% (guide rod hole diameter). Table 4.3 presents measurements of the inner magnet puck, where the largest absolute error was 0.25mm (outer diameter), and the largest percentage error was 0.64% (core diameter). Table 4.4 features measurements of the thrust bearing mount, which had the largest absolute error of 0.192mm (outer diameter), and the largest percentage error of 0.70% (outer core height). The last component featured is presented in Table 4.5, which features the rotor cap. In this case the largest absolute error was 0.12mm (outer diameter), while the largest absolute error encountered of 1.2% (slit width).

Table 4.1: Measurements and error assessment of the 3D printed Inner Magnet Mount.

Parameter	Measurement [mm]	Theoretical [mm]	Absolute Error	% Error
Core Height	12.043	12.000	0.043	0.361%
Separator Height	12.110	12.000	0.110	0.917%
Magnet Slot 15	10.054	10.000	0.054	0.542%
Magnet Slot 5	2.994	3.000	-0.006	-0.194%
Inner Diameter	39.996	40.000	-0.004	-0.010%
Outer Diameter	96.227	96.477	-0.250	-0.259%
Core Diameter	75.820	75.950	-0.130	-0.171%
Slot Height	10.140	10.000	0.140	1.400%
Slot Width	6.998	7.000	-0.002	-0.029%
Hole Centering	1.382	1.357	0.025	1.818%

Table 4.2: Measurements and error assessment of the 3D printed Outer Magnet Mount.

Parameter	Measurement [mm]	Theoretical [mm]	Absolute Error	% Error
Core Height	27.512	27.500	0.012	0.042%
Magnet Slot	9.993	10.000	-0.008	-0.075%
Inner Diameter	98.398	98.477	-0.079	-0.080%
Outer Diameter	142.788	142.898	-0.110	-0.077%
Core Diameter	118.697	118.898	-0.201	-0.169%
Guide Diameter	12.665	12.700	-0.035	-0.276%
Hole Centering	3.770	3.771	-0.001	-0.027%

Table 4.3: Measurements and error assessment of the 3D printed Inner Magnet Puck.

Parameter	Measurement [mm]	Theoretical [mm]	Absolute Error	% Error
Core Height	9.985	10.000	-0.015	-0.150%
Outer Diameter	45.741	46.000	-0.259	-0.562%
Core Diameter	39.743	40.000	-0.258	-0.644%
Hole Spacing	20.004	20.000	0.004	0.020%
Hole Centering	7.995	8.010	-0.015	-0.187%

Table 4.4: Measurements and error assessment of the 3D printed Thrust Bearing Mount.

Parameter	Measurement [mm]	Theoretical [mm]	Absolute Error	% Error
I Core Height	15.044	15.000	0.044	0.293%
O Core Height	8.440	8.500	-0.060	-0.706%
Plate Height	5.004	5.000	0.004	0.075%
Floor Thickness	2.014	2.000	0.014	0.700%
Outer Diameter	79.808	80.000	-0.192	-0.240%
Core Diameter	37.810	38.000	-0.190	-0.500%
Slot ID	39.813	40.000	-0.187	-0.467%
Slot OD	59.900	60.000	-0.100	-0.167%
Hole Spacing	20.050	20.000	0.050	0.250%
Hole Centering	4.040	4.042	-0.002	-0.049%

Table 4.5: Measurements and error assessment of the 3D printed Inner Magnet Cap.

Parameter	Measurement [mm]	Theoretical [mm]	Absolute Error	% Error
Core Height	4.014	4.000	0.014	0.344%
Inner Diameter	60.008	60.000	0.008	0.013%
Outer Diameter	96.355	96.477	-0.122	-0.126%
Slot Width	6.962	7.000	-0.038	-0.548%
Slot Length	1.190	1.200	-0.010	-0.833%
Slit Width	1.012	1.000	0.012	1.200%
Slit Length	10.028	10.000	0.028	0.283%
Slit Depth	1.002	1.000	0.002	0.200%

As a result of this section of the chapter, it can be observed how the largest absolute error were typically encountered on either the outer or inner diameters of the components, with values around 0.2mm. Although not a negligible error for a magnetic bearing whose air-gap is only 1mm, this value is within expectations for a 3D printed structure.

4.2. Measurements and Simulation Data Comparison

4.2.1. Equipment and Measurement Methods

This section of the chapter focuses on the equipment employed in the manufacture, assembly and testing of the experimental bearing prototype. The section will list the equipment in the order in which it was utilized during the setup's development.

The 3D printer employed in the manufacture of all structural components was a PRUSA MK3S+, which was equipped with a 0.4mm nozzle. The layer height for all printed components was 0.15mm, with operated with an infill value of 50%, with the exception of the scale mount, which was printed with 100% infill as it would be a load-bearing structure.

The metallic threaded inserts used for the M3 threads securing both support caps and the radial stiffness tool were inserted using a soldering iron, which can be seen in Figure 4.15a. The temperature of the iron was set to that of the printing temperature of the PLA (215 ° C).

A gaussemeter was employed in the measurement of the magnetic field being enerated by elements within the two assembled arrays, together with a tangential probe. The gaussmeter can be seen in Figure 4.15b.

For the measurement of the generated axial force, a Kern CPB scale was employed. The scale had a range of 30Kg, with a resolution of 0.005 kg, and can be observed in Figure 4.16. The process of measuring the axial force can be seen in Figures 4.17a, 4.17b and 4.18. The first figure mentioned shows the rotor assembly, secured to the thrust bearing mount through the inner magnet puck, which are all fastened into the scale mount. The initial reading gives the weight of this assembly, at 465g. The next figure shows the stator assembly being lowered onto the guiding rods. At this initial point, an attractive force can already be seen, as the scale reading lowered to 0.385g. The stator assembly was then lowered in steps, taking readings of each step and marking its position on the guiding rods with the help of a marker. The reading were then translated to force values and will be features in the next section of this chapter.

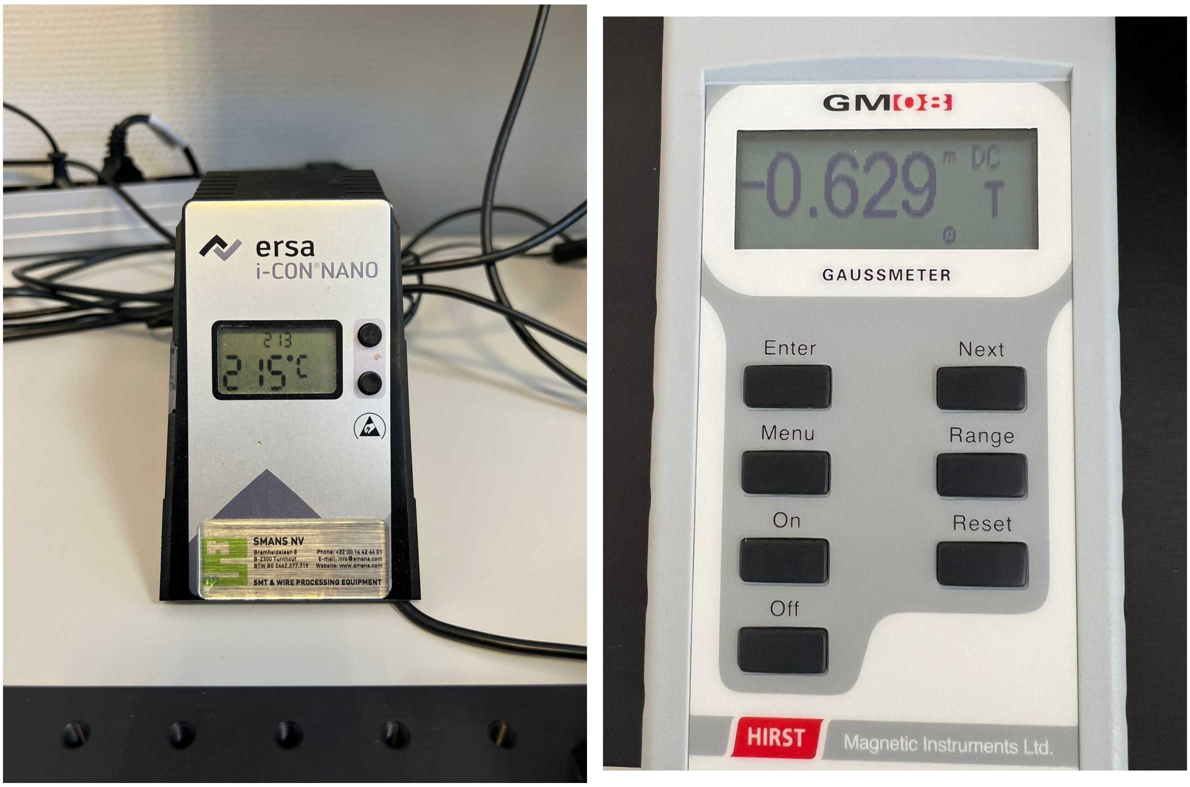

(a) Soldering iron temperature reading.

(b) Gaussmeter reading.

Figure 4.15: Equipment: Soldering iron and Gaussmeter.

Figure 4.16: Raised base plate and scale mount - The scale mount allows for the Thrust Bearing Mount to be assembled onto its thread, thus bypassing the base plate and being entirely supported by the scale.

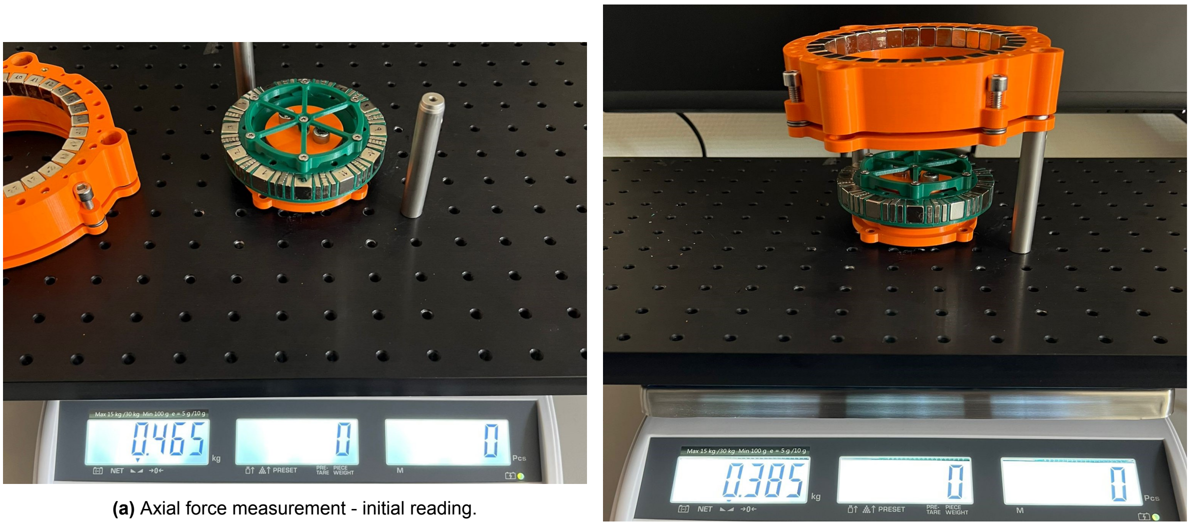

(a) Axial force measurement - initial reading.

(b) Axial force measurement - introduction of stator.

Figure 4.17: Axial force measurement

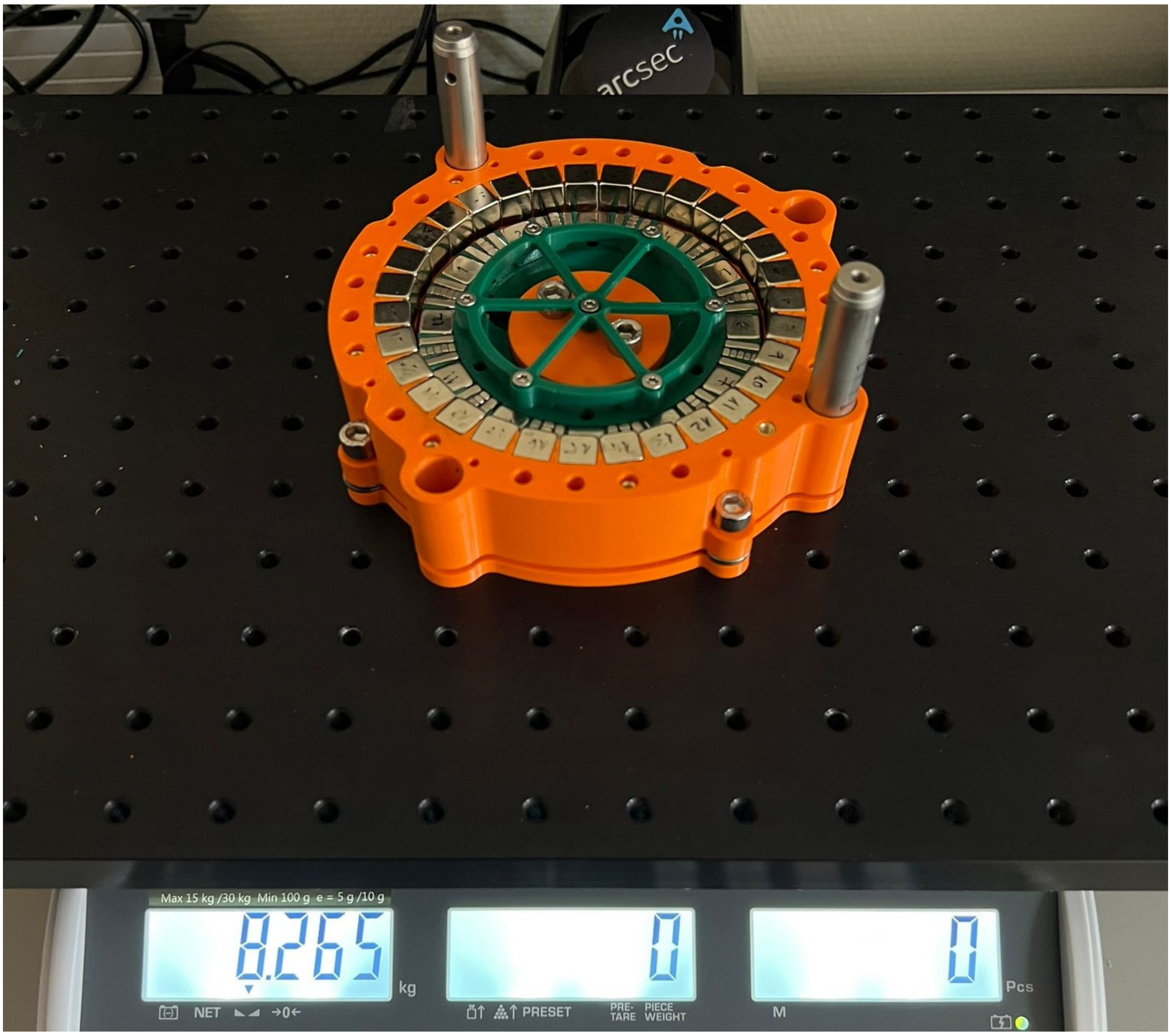

Figure 4.18: Final axial force measurement - the Stator is secured to the Base Plate.

4.2.2. Magnetic Orientation Measurement

The initial measurement of the magnetic elements was conducted with a magnetic sensor which, when placed in close proximity to the magnets, would give the orientation of the closest face of the magnet. Through this system, the correct north and south faces could be determined through rotating the magnet along the axis perpendicular to the magnetic sensor. If all four rotations resulted in a ”North” or ”South” reading, then the magnet was correctly orientated, and the face could be defined. If the magnet would be rotated as previously mentioned, but the sensor would give two ”North” and two ”South” readings, then the magnet was improperly placed, and the magnetic axis was parallel to the magnetic sensor. This process of determining / validating the orientation of the magnets was repeated three times before they would be assembled into the bearing structure. An initial measurement was taken before sanding, when an arrow pointing towards the North face was also marked onto the magnet. A second measurement would be taken after cleaning the magnet, and a third right before assembly (between the second and third measurement the adhesive would be applied to its respective slot). **However, the magnetic sensor which was used for these measurements did not work properly, resulting in a complete reversal of the magnetic arrays on a single element level. As such, the tangential elements were no longer pointing towards the 15 degree element, but towards the 5 degree radial element. This error during the manufacturing process was not spotted until after the complete bearing had been assembled and the first radial test attempt took place.**

Although the magnetization of all magnets was reversed, a model of this erroneous configuration was simulated, which resulted in a constant positive radial stiffness. Positive radial stiffness could be achieved in the simulation thanks to the 15 degree segments, which were still in repulsion with the monolithic array (as those magnets had also been reversed) and had much more of an impact on bearing performance than any other elements in the array.

As such, this error was not the sole culprit of the radial instability of the experimental bearing. Tolerances also had a role, as well as their cause: low stiffness guiding fins on the rotor and stator. These aspects will be discussed further in the Data Comparison section.

4.2.3. Data Comparison

This section of the experimental chapter presents and discusses the magnetic flux and axial force experimental data, and compares it to simulation data in order to calculate errors. The final subsection addresses the radial instability of the bearing, and its probable causes.

Table 4.6: Measurement Data of Total Magnetic Flux Density of individual magnetic elements within the bearing structure. T labels represent theoretical simulation values, while E labels represent experimental data.

15° Seg.		**5° Seg.**		**Tangential Seg.**		**Monolithic Seg.**	
T [mT]	E [mT]	T [mT]	E [mT]	T [mT]	E [mT]	T [mT]	E [mT]
765.75	646	1120.5	846	114.49	103	378.24	452
761.74	647	1145.5	780	125.52	95	388.64	461
786.98	658	1152.3	844	118.22	93	364.82	451
739.04	657	1127.1	841	109.34	83	385.66	464
785.31	631	1125.1	829	87.693	92	372.09	457
758.99	632	1120	817	99.152	102	387.38	448
772.14	641	1118	833	149.89	97	361.82	473
773.4	532	1131.8	831	151.93	87	369.91	472
764.45	562	1112.8	841	104.76	75	364.95	456
784.03	653	1124.1	817	109.65	87	360.4	467
766.1	640	1124.8	845	141.75	95	376.68	469
779.13	654	1109.6	812	113.07	107	368.01	453
769.755	**629.41**	**1125.96**	**828**	**118.78**	**93**	**373.21**	**460.25**

Table 4.7: Error of Total Magnetic Flux Density of individual magnetic elements within the bearing structure.

Magnetic element	Absolute Error [mT]	Percentage Error
15° Seg.	-140.33	-18.23%
5° Seg.	-297.96	-26.46%
Tangential Seg.	-25.780	-21.71%
Monolithic Seg.	87.033	23.32%

Tables 4.6 and 4.7 feature the gaussmeter readings of individual array elements. All segment types have been measured and compared to simulation data from the updated ”fully reversed” erroneous configuration of the bearing. Twelve measurements were taken of each element type, which were then averaged for the calculation of the absolute error and percentage error. All theoretical magnetic flux density results of the stator magnets were overestimated by an average percentage error of 22.13% (varying from 18.23% to 26.46%), while the stator magnets were underestimated with a percentage error of 23%. These relative error values are above the common margins for magnetic bearing experiments (which often fall around 10%). However, most papers deal with larger volume magnets, whose manufacturing tolerances are more easily enforceable. Small magnetic segments, such as the ones employed in this test, are not as accurately magnetized, and can lead to higher errors.

Table 4.8: Measurements and error assessment of the generated axial force experimental data.

Marking [mm]	**Disp. [mm]**	**Reading [Kg]**	**Reading Offset [Kg]**	**Force [N]**	**Theoretical Force [N]**	**Abs. Error [N]**	**% Error**
70.1	78.22	385	-80	-0.78	-	-	-
59.86	67.98	360	-105	-1.03	-	-	-
52.39	60.51	310	-155	-1.52	-	-	-
48.12	56.24	280	-185	-1.81	-	-	-
42.96	51.08	225	-240	-2.35	-	-	-
39.23	47.35	165	-300	-2.94	-	-	-
31.93	40.05	40	-425	-4.17	-	-	-
30.34	38.46	20	-445	-4.36	-	-	-
28.6	36.72	0	-465	-4.56	-	-	-
19.29	27.41	15	-450	-4.41	-	-	-
13.63	21.75	460	-5	-0.05	-34.061	34.01	-99.9%
10.24	18.36	1390	925	9.07	-37.186	28.11	-75.6%
2.09	10.21	4590	4125	40.45	34.703	-5.75	-16.6%
1.69	9.81	5990	5525	54.18	47.85	-6.33	-13.2%
0	8.12	7995	7530	73.84	72.859	-0.99	-1.4%

Table 4.8 features the results of the generated axial force measurement. The marking lengths represent the steps in which the stator was lowered onto the rotor in the experiment, and are measured from the bottom of the guiding aluminium rod. These values were then translated to the displacement between the two magnetic arrays through adding the marking length to the axial displacement measured between stator and rotor magnetic elements when the stator was fastened to the base plate (8.12 mm). Readings of the weight measured by the scale were taken for every marking. These readings then needed to account for the weight of the rotor, thrust bearing and scale mount assembly, as such they were offset by 0.465g. Obtained values were then converted to Force readings, and then compared with available simulation data. As the simulation had a limit on the number of nodes that could be used, the maximum theoretical axial displacement was 22mm. All force values measured below this axial displacement could be compared to theoretical results to obtain the absolute and relative errors.

The comparison between axial force theoretical and experimental data is also plotted in Figure 4.19. From this graph it can be observed that the simulation and experimental data fit quite well for the first three measurements where displacements are relatively small (8-10mm), leading to 1.4%, 13.2% and

16.6% relative errors. However, past this point the simulation data was no longer accurate, considerably overestimating the repulsive force between the magnetic arrays.

The cause for this discrepancy in the case of axial displacements larger than 10mm could be caused by poor manufacturing tolerances of the assembled magnets, some of which featured 4-5 degree deviations from their designed orientation due to magnetic interactions between adjacent elements, which resulted in bending of the guiding fins. Other error sources could be the measurements of the markings and final air-gap of the configuration, or the variance of the real axial displacement due to the scale weigh pan, which also compressed with increasing force. If accounting for the scale compression, the real axial displacements would be slightly smaller than the ones calculated in Table 4.8, as the calculations are based on the final ”compressed” rotor, and would have the most effect on the values of larger displacements. A smaller axial displacement would then lead to a reduction in error between simulated and experimental results, however it would not account for the entire overestimation of the repulsive force.

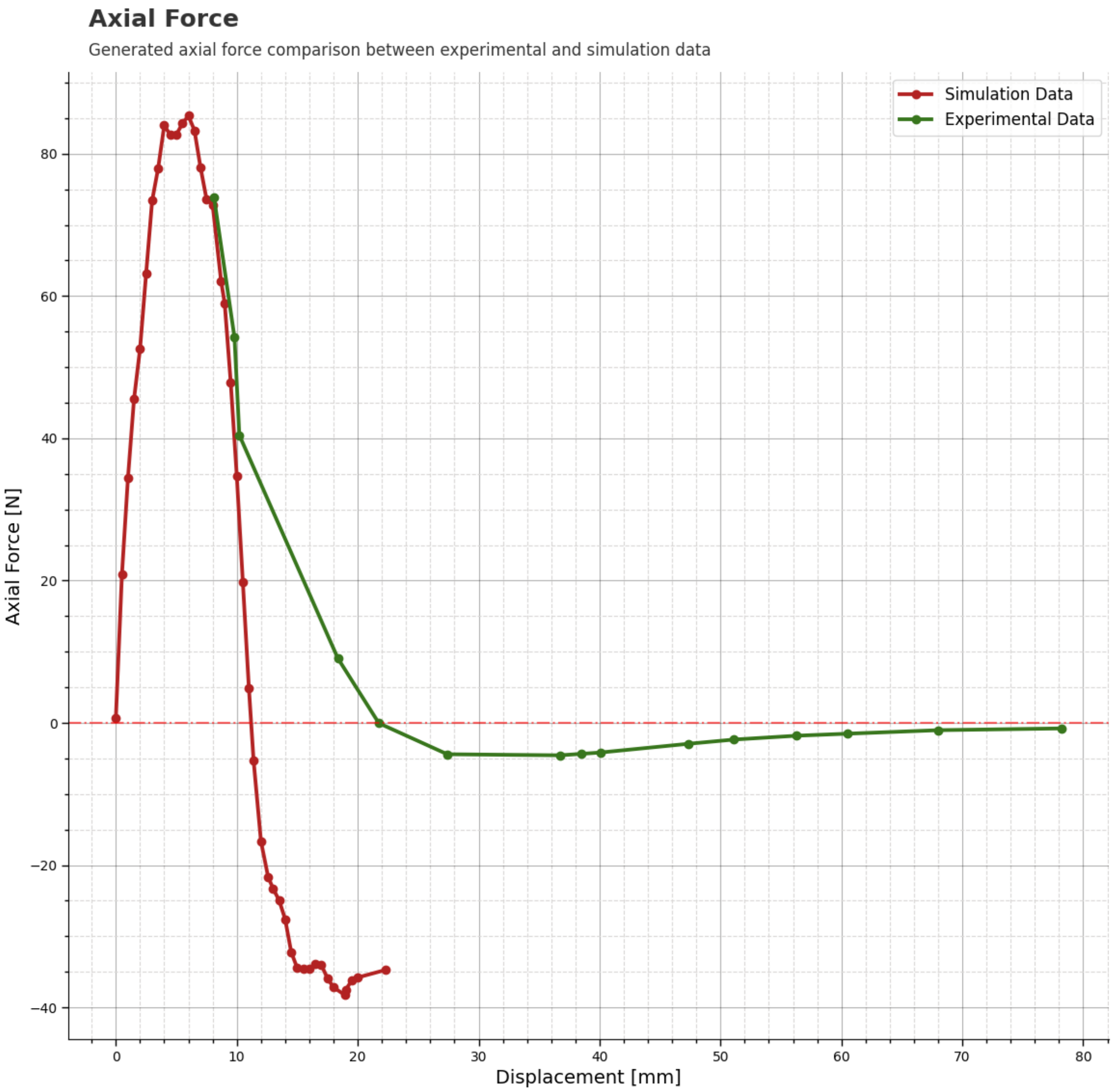

Figure 4.19: Axial Force - Experimental data vs Simulation Data

5

Conclusions and Recommendations

5.1. Research Question Overview

Throughout the thesis report, all research and experimental testing has been conducted with the scope of providing a qualitative answer to the Research Questions presented and discussed in Chapter 2.

1. **RQ-1:** How does the number of segments in a Halbach multipole magnet affect bearing performance in terms of generated magnetic field and bearing stiffness?
2. **RQ-2:** How does the ratio between the number of segments within a multipole magnet affect bearing performance in terms of generated magnetic field and bearing stiffness?
3. **RQ-3:** In comparison to a conventional monolithic magnetic bearing, how does a Halbach multipole magnet affect performance in terms of bearing stiffness?
4. **RQ-4:** To what extent do manufacturing and assembly tolerances affect the operation and radial stability of a multipole magnetic bearing?

RQ-1

This research question was addressed in Chapter 3, where radially segmented configurations with 12 to 40 segments per magnetic array were simulated and compared. The variable characterizing the magnetic field is the magnetic flux density, which, under the form of Total Magnetic Flux Density averaged over air-gap volume, increases with higher segment numbers in the case of the Radial and Radial Focus configurations, while peaking at 16 elements for the Axial Configuration, then decreasing steadily. These relationships can be observed in Figure **??**. In terms of radial stiffness, three segment number samples (32, 36 and 40 segments) were chosen for the four considered configurations: Radial Focus, Radial, Axial Halbach and Axial non-Halbach. The configurations then had their inner magnetic array displaced in the Y direction by 0.25, 0.5 and 0.75mm and the resulting force was measured. This force then was divided by the respective displacement to obtain radial stiffness values. Stiffness values only increased in the case of the Radial Focus configuration, while remaining relatively constant for the rest. This evolution can be observed in Figure 3.11, as well as Table 3.8. Both the generated magnetic field and radial stiffness have been studied in the case of varying numbers of segments per magnetic array.

RQ-2

This research question was also addressed in Chapter 3, where ratios of the number of segments between magnets and within a single magnetic array were studied. The first ratio was addressed in the Non-Symmetrical bearing configurations chapter, where magnetic arrays with varying number of segments (12/16 - 12/24 - 12/32) were simulated. These configurations were introduced in an attempt to counteract the oscillating behavior of the absolute radial force and average air-gap total magnetic flux density present in the segmented designs. As the cause of these oscillations in performance were the overlapping of same orientation magnetic segments, the thought of offsetting the elements relative to each other raised intrigue and as such non-symmetrical bearing designs were introduced to the study. Although the oscillations in performance stopped almost entirely for the absolute radial force (for all considered ratios), and for TMFD data in the case of Radial and Axial configurations, while the phenomenon persisted for TMFD data of the Radial Focus configuration. These effects can be observed in Figures 3.18a to 3.18f. However, non-symmetric configurations introduced new issues into the system, in the form of non-zero Cartesian forces. Both X and Y forces acting on the rotor magnetic array were no longer zero in a centered position, as was the case in the simple segmented configurations. This behavior can be seen in Figure 3.17. This would lead to bearing instability and negative radial stiffness in certain rotational positions, violating REQ-1 and REQ-2. This is due to the bearing no longer being ”balanced”. In the case of the segmented designs, for each stator magnet exerting a force onto the rotor, the sum of all forces generated by other magnetic elements with the same orientation within the array would counteract its effect. This would translate to null Cartesian forces. However, by changing the number of magnets in each magnetic array, this counteracting effect is disturbed, leading to an unstable bearing.

The second type of ratio was studied with the Monolithic-Multipole configuration design, were ”working” magnets were three times the arc length of the ”pattern completion” magnets, leading to a 1:3 ratio. This configuration proved to fully stabilize the bearing, through diminishing the destabilizing effects of overlapping same orientation magnets and providing a uniform magnetic field through the monolithic bearing. The radial stiffness also showed a considerable improvement over the 1:1 ratio of the segmented design when the monolithic bearing was also considered (from 7 N/mm to 31.7 N/mm in the case of the Radial Focus configuration). In conclusion, non-symmetric configurations level out most of the TMFD data, but introduce instability to the system in the form of negative stiffnesses across its rotational range.

RQ-3

Similarly to the first two research questions, RQ-3 was addressed in Chapter 3 throughout all the considered configurations. In the first section of the chapter, segmented magnetic designs proved that they could achieve peak stiffness values 40% higher (Radial Focus 40 Seg.) than their monolithic counterparts. However, peak stiffness does not translate into a functional bearing. As a result of the high variations in the total magnetic flux density across the air-gap, which were caused by overlapping same orientation magnets, their magnetic field oscillated between sections of repulsion and attraction between stator and rotor magnetic arrays. In the the last section of the chapter, monolithic-multipole magnetic designs were the first bearings which satisfied all imposed requirements. However, in the pursuit of a constant performance across bearing rotation, the generated stiffness proved to fall below the one offered by conventional monolithic bearings, which can be observed in Figures 3.28 and 3.27. This loss of radial stiffness performance is correlated to the reduction in the generated external magnetic field, which is considered to be an advantage of the monolithic-multipole bearing. This behavior can be observed by comparing Figure 3.4a to Figures 3.24c and 3.25c.

RQ-4

This research question was addressed in Chapter 4, where the monolithic-multipole simplified design was prototyped and analyzed. Manufacturing tolerances were studied through the measurement of both structural components and assembled magnetic elements in order for them to be compared to simulation data. While the structural side of the prototype had very small errors in geometry (typically < 0.1%), the magnetic flux density reading varied from an 18.2% deviation for the ”working” magnetic segments, to 26.4% and 21.7% for the ”pattern completion” magnets. These percentage errors, while high by comparison to the ones defining the prototype structure, are only slightly above expectations (20% errors being common magnetic simulations). Axial force measurements also presented acceptable errors within the near field (from 1.4% to 13.2% within the first 10mm of displacement), while the far field presented more erroneous results, which can be accounted for by the limitations of the simulation environment. However, radial stability was not achieved through the testing of the prototype. This is most likely caused by deviations within the air-gap of the assembly. As the considered air-gap was only 1 mm, deviations which would be considered acceptable (0.1-0.2 mm) in other situations, have an amplified effect on system performance in this application. One of the main issues which caused this deviation is the low stiffness of the bearing structure, more exactly the fins separating the multipole array magnetic elements. In theory, these fins should have guided the magnets and enforce their proper orientations. However, this was not the case in reality, as the strength of the magnetic interactions when placed in such close proximity overloaded the fins, resulting in 4-5 degree deviations. These deviations mostly affected the radially magnetized ”pattern completion” elements which were, independently from adjacent magnets, in constant attraction with the rotor monolithic design. This lead to displaced elements asserting more impact on the bearing operation than simulations planned for, resulting in a radially unstable bearing through overly strong attraction forces between the stator and rotor magnetic arrays. In conclusion, tolerances have a considerable impact on bearing performance and stability. A low stiffness structure which allowed for 4-5 degree orientation deviations has been proved to be unfit for qualitative testing of a multipole magnetic bearing’s operation. As such, **research question RQ-4 requires further study, as no qualitative tolerance analysis was conducted, but only tolerance assessment.**

5.2. Recommendations for future work

Based on the concepts developed and studied in this thesis, several recommendations for future project which would be beneficial to the study of multipole magnetic bearings have been identified and briefly presented in this section.

An aspect of segmented multipole magnetic bearings which was not explored in this work is the stacking of multiple magnetic arrays. This concept could be beneficial to configurations with non-zero axial forces in centered positions, as stacking two such arrays on opposing faces could counteract the destabilizing force. In this manner, new configurations are ”unlocked” for implementations into multipole bearing.

Another aspect which was not comprehensively studied is the replacement of array magnetic elements with steel or iron laminated inserts. This concept can be further expanded to entire structures that guide the magnetic field around the bearing back into the air-gap, thus reducing the external polluting magnetic field all while increasing air-gap magnetic flux density and thus bearing performance.

A last concept which was not explored in this work is the radial ratio between ”working” magnetic elements and ”pattern completion” magnetic elements. As a method of further increasing bearing performance, the pattern completion magnets could be further reduced in volume through altering the width of the magnets. In this manner they could also be distanced from the opposing field, thus further reducing their negative impact on bearing performance.

Recommendations regarding the experimental setup and the assembly process have also been considered and will be discussed in this paragraph. The primary takeaway is to not underestimate the strength of the magnets, and their generated forces. Although the magnets employed in the experiment were relatively small in volume, their assembly process was rather difficult, especially in the case of the monolithic array. During assembly, the magnetic elements would exert great repulsive forces when being slotted into the array, leading to deviations in orientation and even failure of the guiding fins (and thus the entire supporting structure). In order to mitigate this, high stiffness supports should be used (3D printed PLA structures were not enough), together with robust assembly procedures, which are not impacted by segment-array interactions.

References

[1] C. J. Dennehy, “A survey of reaction wheel disturbance modeling approaches for spacecraft line-of-sight jitter performance analysis,” in *Proc. European Space Mechanisms and Tribology Symp. Munich, Germany*, 2019.

[2] F. Ishola, A. Carrasco-Casado, R. Cordova, *et al.*, “Characterization and comparison of cubesat and drone platform jitter effects on laser beam pointing stability,” 2022.

[3] W. Bialke and E. Hansell, “A newly discovered branch of the fault tree explaining systemic reaction wheel failures and anomalies,” in *Proceedings of the European Space Mechanisms and Tribology Symposium*, 2017, pp. 20–22.

[4] W. Bialke, “A discussion of friction anomaly signatures in response to electrical discharge in ball bearings,” in *Aerosp. Mech. Symp*, vol. 44, 2018, pp. 55–68.

[5] “Nasa.gov.” (2023), [Online]. Available: `https://nssdc.gsfc.nasa.gov/nmc/spacecraft/display.action?id=1999-035A#:~:text=FUSE%20Science%20Operations%20were%20on,the%20reaction%20wheels%20were%20unsuccessful..`

[6] “Nasa.gov.” (2023), [Online]. Available: `https://www.nasa.gov/feature/ames/kepler/nasa-ends-attempts-to-fully-recover-kepler-spacecraft-potential-new-missions-considered.`

[7] G. Schweitzer, E. H. Maslen, *et al.*, *Magnetic bearings*. Springer, 2009.

[8] W. Jones, “Earnshaw’s theorem and the stability of matter,” *European Journal of Physics*, vol. 1, no. 2, p. 85, 1980.

[9] K. P. Lijesh and H. Hirani, “Design and development of halbach electromagnet for active magnetic bearing,” *Progress In Electromagnetics Research C*, vol. 56, pp. 173–181, 2015.

[10] Y.-M. Choi, M. G. Lee, D.-G. Gweon, and J. Jeong, “A new magnetic bearing using halbach magnet arrays for a magnetic levitation stage,” *Review of scientific instruments*, vol. 80, no. 4, p. 045 106, 2009.

[11] Y.-M. Choi and D.-G. Gweon, “A high-precision dual-servo stage using halbach linear active magnetic bearings,” *IEEE/ASME Transactions on Mechatronics*, vol. 16, no. 5, pp. 925–931, 2010.

[12] D. Supreeth, S. I. Bekinal, and R. Shivamurthy, “An overview on electrodynamic bearings,” *IEEE Access*, 2022.

[13] J.-P. Yonnet, G. Lemarquand, S. Hemmerlin, and E. Olivier-Rulliere, “Stacked structures of passive magnetic bearings,” *Journal of Applied Physics*, vol. 70, no. 10, pp. 6633–6635, 1991.

[14] K. Halbach, “Design of focussing and guide structures for charged particle beams using rare earth cobalt permanent magnets,” California Univ., Berkeley (USA). Lawrence Berkeley Lab., Tech. Rep., 1981.

[15] W. Robertson, B. Cazzolato, and A. Zander, “A multipole array magnetic spring,” *IEEE Transactions on Magnetics*, vol. 41, no. 10, pp. 3826–3828, 2005.

[16] J.-P. Yonnet, “Analytical calculation of magnetic bearings,” in *Proc. 5th Intern. Workshop Rare Earth-Cobalt Perm. Mag. and Their Appl., 1981*, 1981.

[17] X. Feipeng, L. Tiecai, and L. Yajing, “A study on passive magnetic bearing with halbach magnetized array,” in *2008 International Conference on Electrical Machines and Systems*, IEEE, 2008, pp. 417–420.

[18] R. Moser, J. Sandtner, and H. Bleuler, “Optimization of repulsive passive magnetic bearings,” *IEEE transactions on magnetics*, vol. 42, no. 8, pp. 2038–2042, 2006.

[19] S. Jinji, R. Yuan, and F. Jiancheng, “Passive axial magnetic bearing with halbach magnetized array in magnetically suspended control moment gyro application,” *Journal of Magnetism and Magnetic Materials*, vol. 323, no. 15, pp. 2103–2107, 2011.

[20] A. Mystkowski and L. Ambroziak, “Frequency and non-linear aninvestigation of passive magnetic bearing with halbach-array,” *acta mechanica et automatica*, vol. 4, no. 4, pp. 78–82, 2010.

[21] K. K. Nielsen, C. Bahl, N. A. Dagnaes, I. F. Santos, and R. Bjørk, “A passive permanent magnetic bearing with increased axial lift relative to radial stiffness,” *IEEE Transactions on Magnetics*, vol. 57, no. 3, pp. 1–8, 2020.

[22] W. Wu, S. Li, X. Yang, C. Shuai, Z. Li, and X. Wang, “Improvement of the static and dynamic characteristics of water-lubricated bearing with integrated halbach magnet arrays,” *Tribology Transactions*, no. just-accepted, pp. 1–18, 2023.

[23] J.-f. LIU, H. Choi, and M. Walmer, “Design of permanent magnet systems using finite element analysis,” *Journal of Iron and Steel Research, International*, vol. 13, pp. 383–387, 2006.

[24] D. J. Eichenberg, C. A. Gallo, and W. K. Thompson, “Development and testing of a radial halbach magnetic bearing,” Tech. Rep., 2006.

[25] E. Marth, G. Jungmayr, M. Panholzer, and W. Amrhein, “Optimization and realization of a multipole permanent magnetic bearing with rotating magnetization,” *Proceedings of the Institution of Mechanical Engineers, Part I: Journal of Systems and Control Engineering*, vol. 230, no. 4, pp. 320–329, 2016.

[26] R. Bjørk and C. Bahl, “A conical passive magnetic bearing with constant stiffness,” *Scientific Reports*, vol. 12, no. 1, pp. 1–9, 2022.

[27] F. Bancel, “Magnetic nodes,” *Journal of Physics D: Applied Physics*, vol. 32, no. 17, p. 2155, 1999.

[28] E. P. Furlani, *Permanent magnet and electromechanical devices: materials, analysis, and applications*. Academic press, 2001.

[29] R. Ravaud and G. Lemarquand, “Discussion about the magnetic field produced by cylindrical halbach structures,” *Progress In Electromagnetics Research B*, vol. 13, pp. 275–308, 2009.

[30] R. Ravaud and G. Lemarquand, “Analytical expressions of the magnetic field created by tile permanent magnets of various magnetization directions,” in *Progress In Electromagnetics Research Symposium 2009 Moscow*, 2009, p. 511.

[31] J. P. Selvaggi, S. J. Salon, and M. V. Chari, “Employing toroidal harmonics for computing the magnetic field from axially magnetized multipole cylinders,” *IEEE transactions on magnetics*, vol. 46, no. 10, pp. 3715–3723, 2010.

[32] J. Selvaggi, S. Salon, and M. Chari, “Computing the magnetic induction field due to a radially-magnetized finite cylindrical permanent magnet by employing toroidal harmonics,” *Progress in electromagnetics research*, vol. 245, 2010.

[33] L. Hu, M. Liu, D. Yang, *et al.*, “Calculation of field and force of halbach arrays: Improved magnetic charge method for irregular magnetized magnets,” *Proceedings of the Institution of Mechanical Engineers, Part C: Journal of Mechanical Engineering Science*, vol. 236, no. 23, pp. 11 136–11 149, 2022.

[34] E. Marth, G. Jungmayr, and W. Amrhein, “A 2-d-based analytical method for calculating permanent magnetic ring bearings with arbitrary magnetization and its application to optimal bearing design,” *IEEE transactions on magnetics*, vol. 50, no. 5, pp. 1–8, 2013.

[35] M. Fitouri, Y. Bensalem, and M. N. Abdelkrim, “Comparison between 2d and 3d modeling of permanent magnet synchronous motor using fem simulations,” in *2020 17th International Multi-Conference on Systems, Signals & Devices (SSD)*, IEEE, 2020, pp. 681–685.

[36] S. Naik, B. Bag, and K. Chandrasekaran, “A 2d and 3d analysis on electromagnetic parameters of spoke-shape interior permanent magnet synchronous motor using fem,” *Periodica Polytechnica Electrical Engineering and Computer Science*, 2023.

[37] S. Kulkarni, F. Zhao, I. C. Nlebedim, R. Fredette, and M. P. Paranthaman, “Comparative life cycle assessment of injection molded and big area additive manufactured ndfeb bonded permanent magnets,” *Journal of Manufacturing Science and Engineering*, vol. 145, no. 5, p. 051 001, 2023.

[38] J. Cui, J. Ormerod, D. Parker, *et al.*, “Manufacturing processes for permanent magnets: Part i—sintering and casting,” *JOM*, vol. 74, no. 4, pp. 1279–1295, 2022.

[39] J. Cui, J. Ormerod, D. S. Parker, *et al.*, “Manufacturing processes for permanent magnets: Part ii—bonding and emerging methods,” *JOM*, vol. 74, no. 6, pp. 2492–2506, 2022.

[40] L. Li, A. Tirado, I. Nlebedim, *et al.*, “Big area additive manufacturing of high performance bonded ndfeb magnets,” *Scientific reports*, vol. 6, no. 1, pp. 1–7, 2016.

[41] S. Jafarzadeh, A. C. Wulff, K. Engelbrecht, and C. Bahl, “Additive manufacturing of hard magnetic passive shims to increase field homogeneity of a halbach magnet,” *Advanced Engineering Materials*, 2023.

[42] “Sonnecy.com.” (2023), [Online]. Available: `https://www.sonnecy-shop.com/media/pdf/67/d2/e7/CY-Mag-NdFeB.pdf`.

[43] “Supermagnete.be.” (2023), [Online]. Available: `https://www.supermagnete.be/eng/physical-magnet-data`.

A

Appendix: Prototype Component Drawings

D (2 : 1)

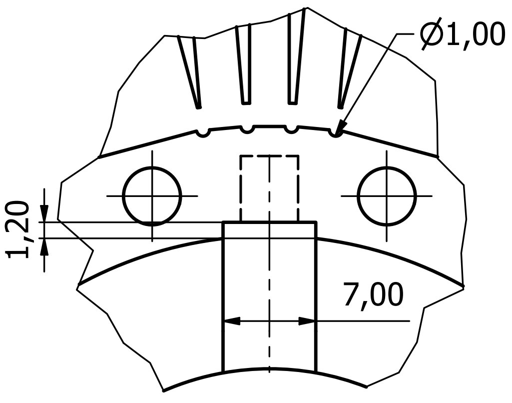

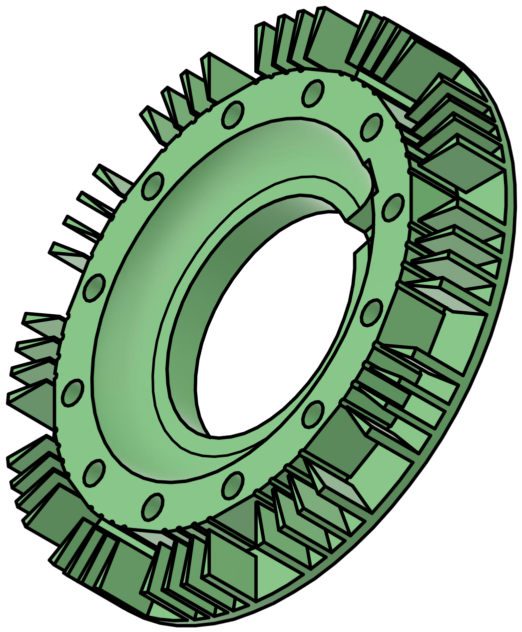

A-A (1 : 1)

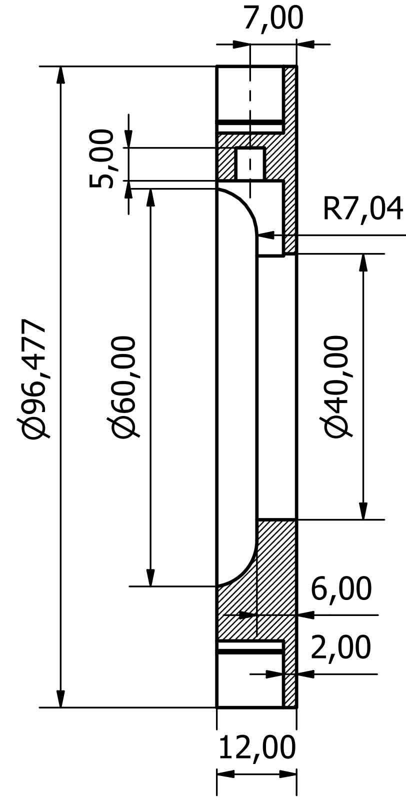

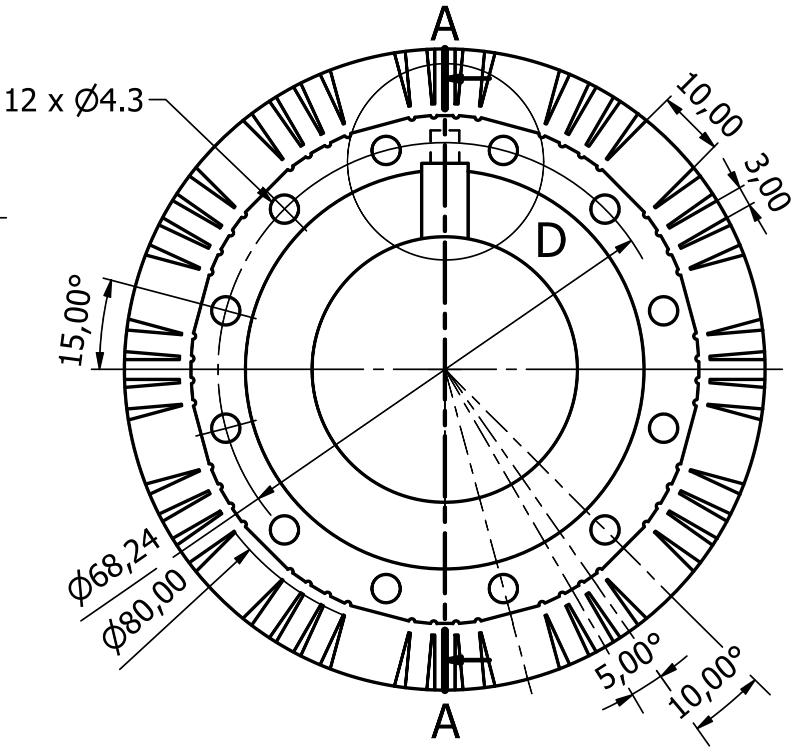

Designed by Vlad Buta	Checked by	Approved by	Date		Date 09/08/2023
		Inner Magnet Mount			
		Inner_Magnet_Mount		Edition	Sheet 1 / 1

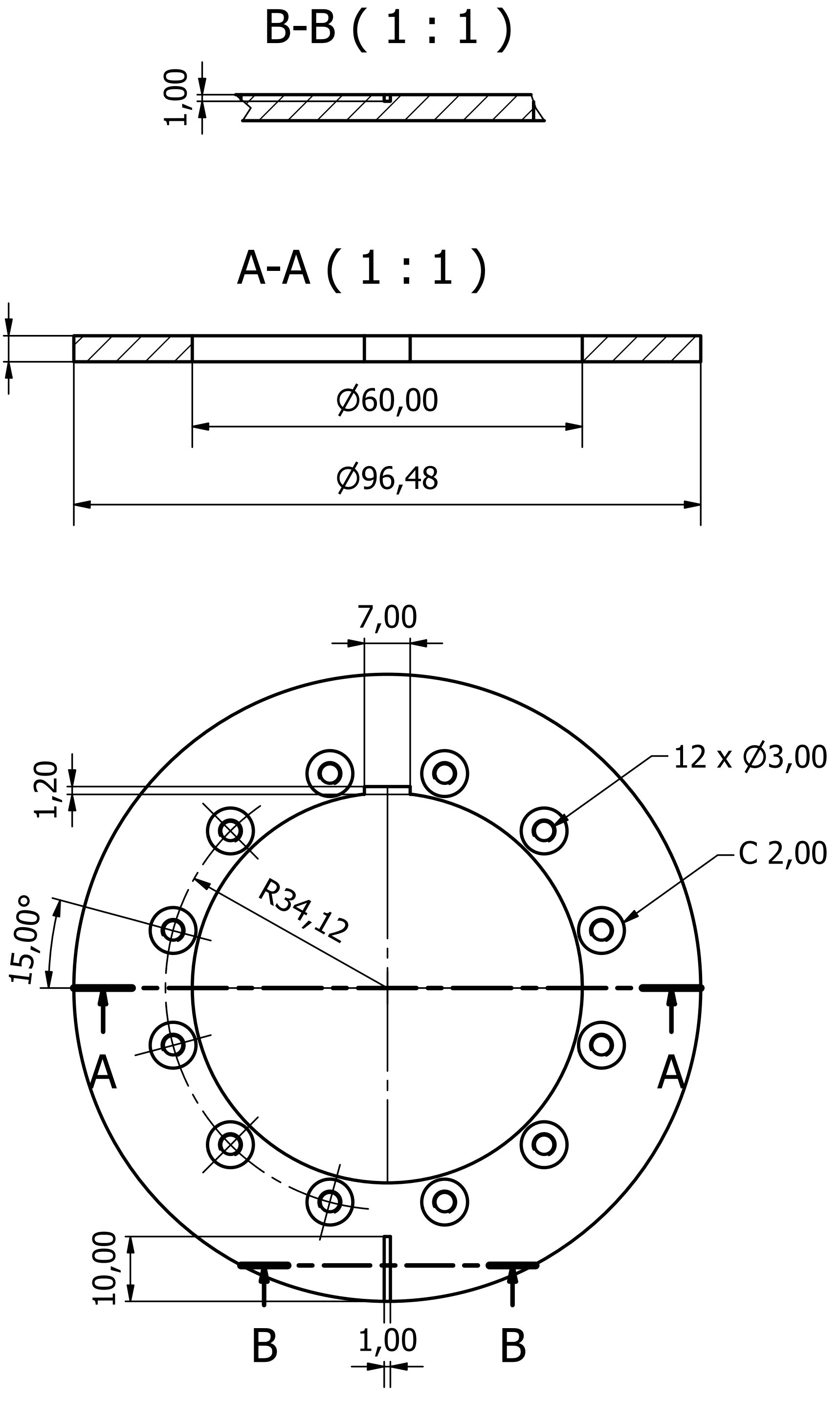

Designed by vladb	Checked by	Approved by	Date		Date 10/08/2023

Inner_Magnet_Mount_Cap

Edition

Sheet
1 / 1

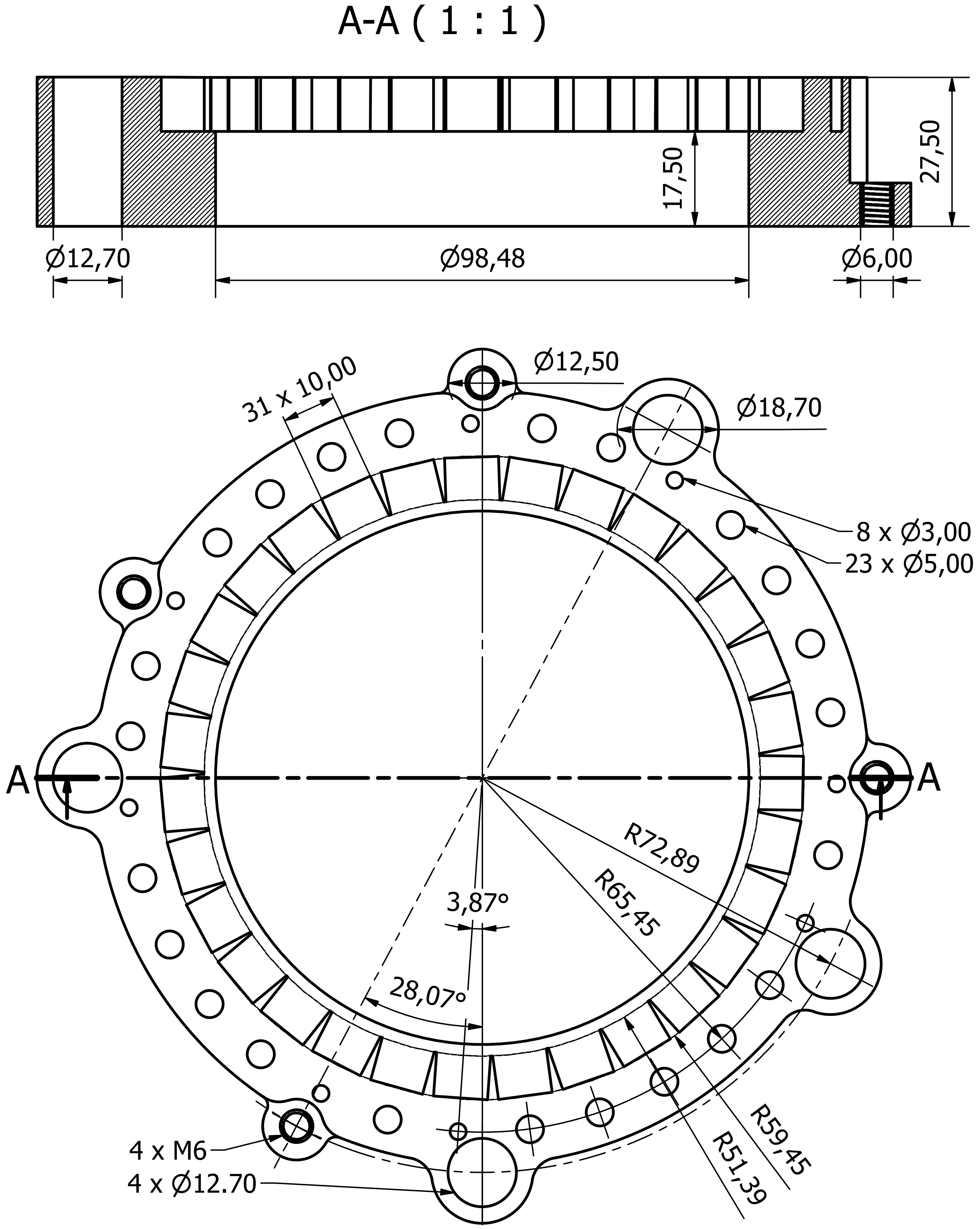

Designed by vladb	Checked by	Approved by	Date		Date 10/08/2023	
	Outer_Magnet_Mount			Edition	Sheet 1 / 1	

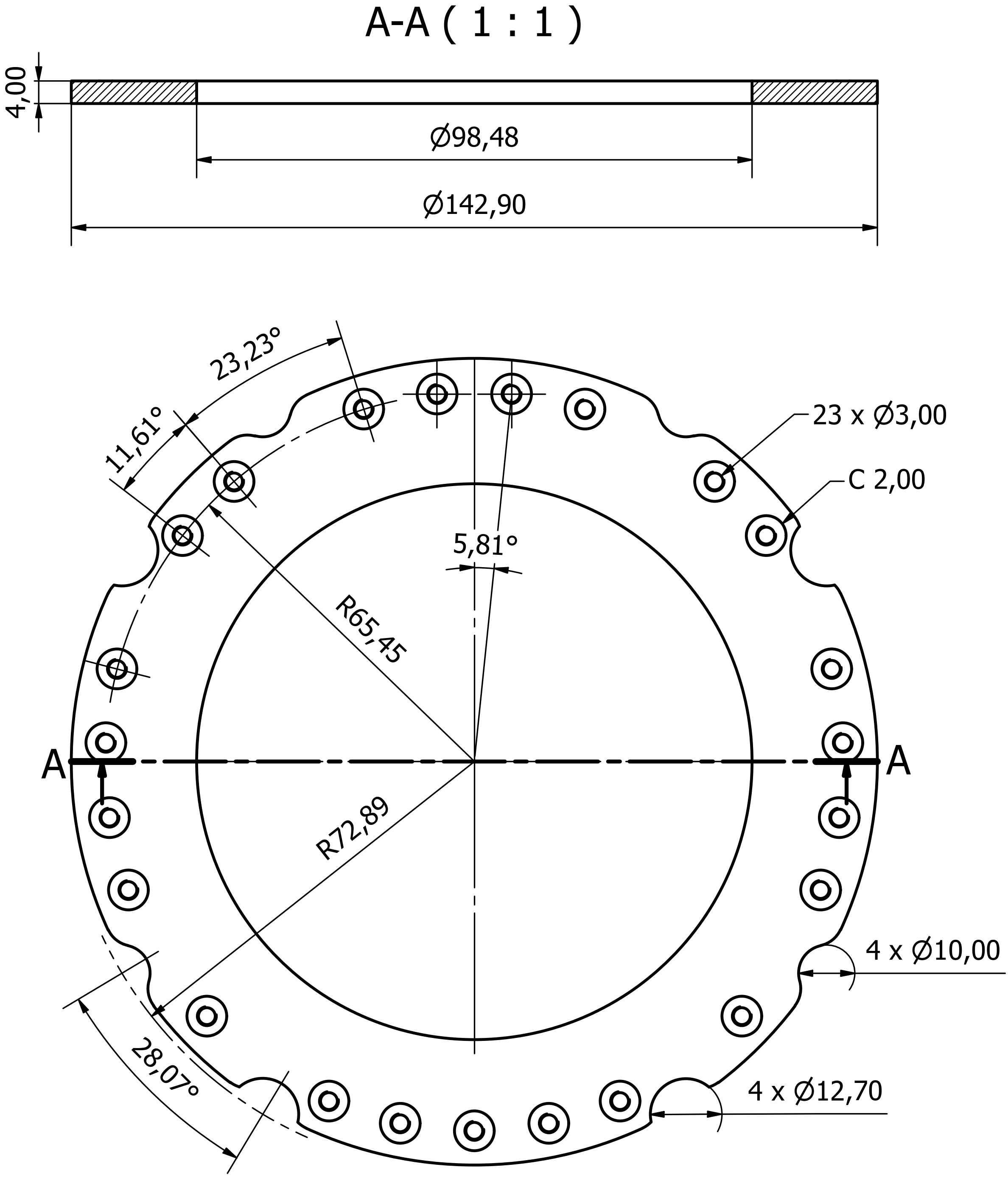

Designed by vladb	Checked by	Approved by	Date	Date 10/08/2023	
		Outer_Magnet_Mount_Cap		Edition	Sheet 1 / 1

A-A (1 : 1)

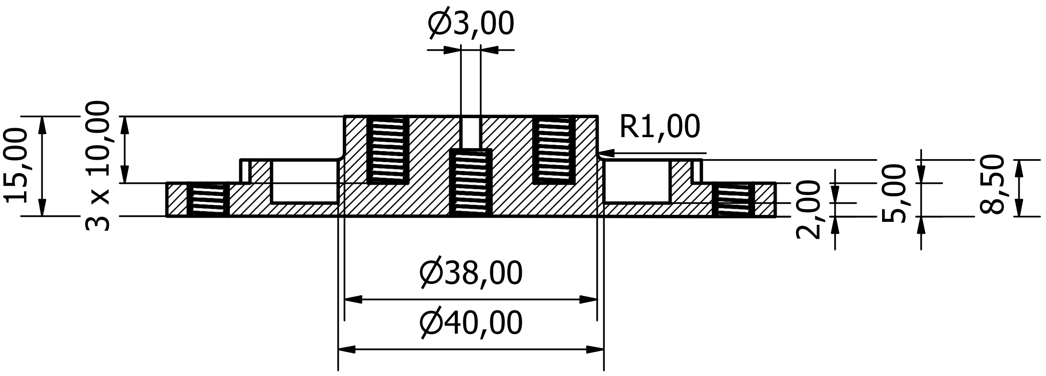

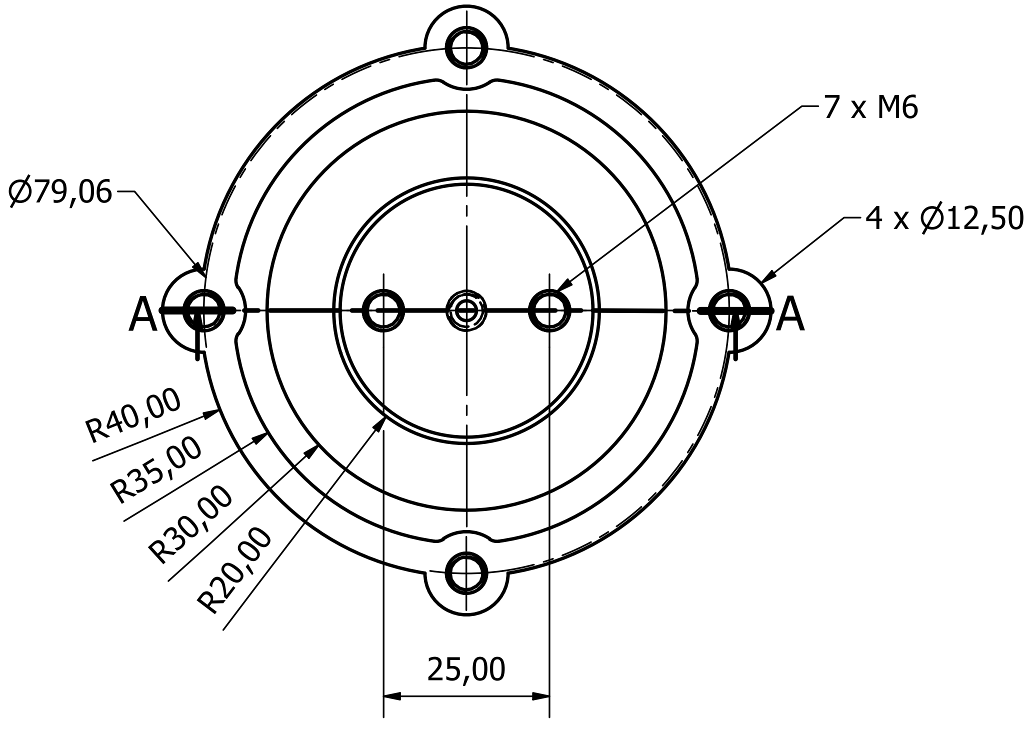

Designed by vladb	Checked by	Approved by	Date	Date 10/08/2023	
	Thrust Bearing Mount			Edition	Sheet 1 / 1

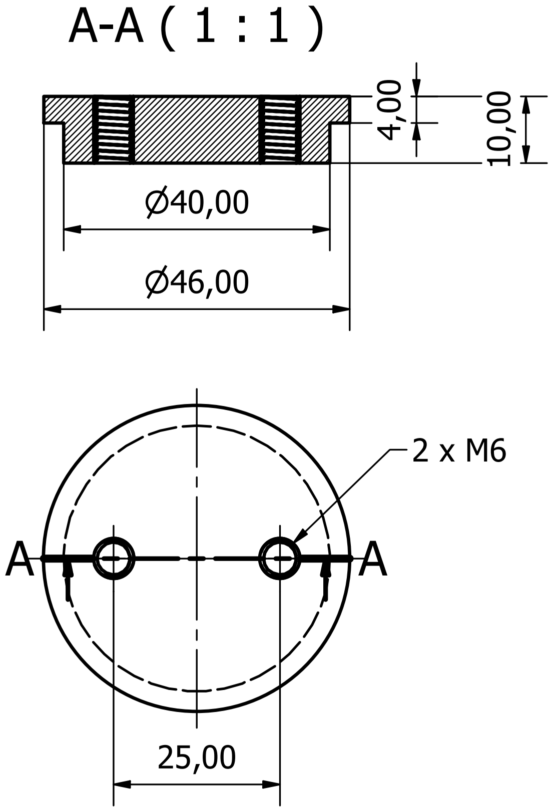

Designed by vladb	Checked by	Approved by	Date		Date 10/08/2023
		Inner_Magnet_Puck		Edition	Sheet 1 / 1

A-A (1 : 1)

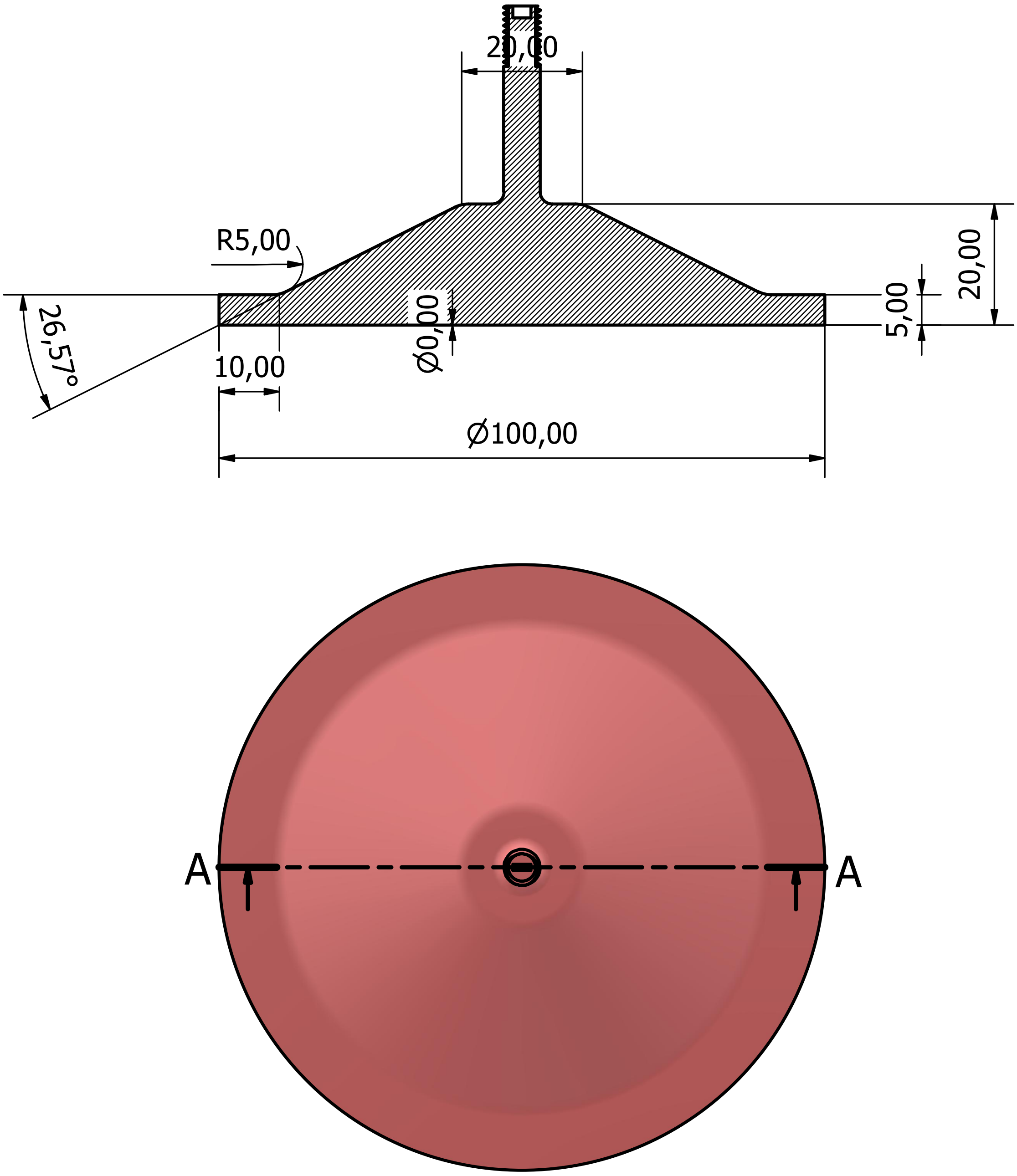

Designed by vladb	Checked by	Approved by	Date	Date 10/08/2023	
	Inner_Magnet_Scale_Mount_V2			Edition	Sheet 1 / 1